Additive Manufacturing of Porous Titanium Structures for Use in Orthopaedic Implants

by

Ahmad Basalah

A thesis
presented to the University of Waterloo
in fulfilment of the
thesis requirement for the degree of
Doctor of Philosophy
in
Mechanical Engineering

Waterloo, Ontario, Canada, 2015

Author Declaration

This thesis consists of material all of which I authored or co-authored: see Statement of Contributions included in the thesis. This is a true copy of the thesis, including any required final revisions, as accepted by my examiners.

Statement of Contributions

This thesis includes seven chapters. Each chapter starting from chapter 2 up to 6 represents a publication I authored or co-authored as follow:

- The first chapter is the introduction including the motivation and objectives of the thesis.

-The second chapter is the first one-third of a book chapter:

Vlasea M., Basalah A., Azhari A., Kandel R. Toyserkani E. Additive manufacturing for bone load bearing applications. Edited by: Lijie Grace Zhang, John Fisher KL, 3D Bioprinting and Nanotechnology in Tissue Engineering and Regenerative Medicine. 1st Edition, Elsevier Inc.; 2015.

-The third chapter consists of a journal article published in the Journal of Biomedical Materials Research Part B Applied Biomaterials:

Basalah A, Shanjani Y, Esmaeili S, Toyserkani E. Characterizations of additive manufactured porous titanium implants. J Biomed Mater Res B Appl Biomater 2012;100:1970–9.

-The fourth chapter includes a manuscript will be submitted soon:

Basalah A, Esmaeili S, Toyserkani E. On the influence of sintering protocols and layer thickness on the physical and mechanical properties of additive manufactured titanium porous structures.

-The fifth chapter consists of a manuscript submitted to "International Journal of Advanced Manufacturing Technology" without the biological study section in June 7, 2015:

Basalah A, Esmaeili S, Toyserkani E. Mechanical Properties of Additive Manufactured Porous Titanium Bio-Structures with Oriented Macro-Scale Channels.

- The sixth chapter consists of a manuscript submitted to the Journal of Biomedical Physics & Engineering Express in June 18, 2015:

Basalah A, Esmaeili S, Toyserkani E. A Novel Additive Manufacturing-based Technique for Developing Bio-structures with Conformal and Encapsulated Channels.

-Finally, chapter seven includes the conclusions and future work.

Abstract

This dissertation explores additive manufacturing of porous titanium structures for possible use as scaffolds in orthopaedics. Such scaffolds should be tailored in terms of mechanical properties and porosity to satisfy specific physical and biological needs. In this thesis, powder metallurgy was combined with additive manufacturing to successfully fabricate porous Ti structures.

This study describes physical, chemical, and mechanical characterizations of porous titanium implants made by the proposed powder bed inkjet-based additive manufacturing process to gain insight into the correlation of process parameters and final physical and mechanical properties of the porous structure. A number of processing parameters were investigated to control the mechanical properties and porosity of the structure. In addition, a model was developed based on the microstructural powder compaction to predict the porosity as a function of the developed sinter neck among the particles during the sintering process. The produced samples were characterized through several methods including porosity measurement, compression test, Scanning Electron Microscopy (SEM), Energy-dispersive X-ray spectroscopy (EDX), and shrinkage measurements.

Additionally, a new method for manufacturing Ti implants includes encapsulated networks of macro-sized channels was introduced. Also, the influence of different orientations and numbers of channels within the additive-manufactured structures were investigated.

The characterization test results showed a level of porosity in the samples in the range of 12-43%, which is within the range of cancellous and cortical bone porosity. The compression test results showed that the porous structure's compressive strength is in the range of 56-1000 MPa, yield strength is in the range of 27-383 MPa, and Young's modulus is in the range of 0.77-11.46 GPa. This technique of

manufacturing porous Ti structures demonstrated a low level of shrinkage with the shrinkage percentage ranging from 1.5-12%. Also, the experimental results demonstrated excellent agreement with the developed model. Moreover, the novel method of fabricating the encapsulated channel show a reduction in the shear strength to 24-30% that is advantageous for bone implants. The results demonstrate that the channel orientation in the structure affect the shrinkage rate in the parts with vertically orientated channels, in which a relatively isotropic shrinkage in vertical and horizontal directions is achieved after sintering.

Acknowledgments

At the beginning, I would like to say thanks be to Allah, who has guided and assisted me to accomplish this thesis.

I would like to express my sincere gratitude to my Supervisors; Prof.Ehsan Toyserkani and Prof. Shahrzad Esmaeili for the great support, encouragement, trust, patience, assistance and guidance they have provided me over the past few years. The knowledge and support that I've given from my supervisors were really invaluable and made my life in Canada enjoyable.

I hereby acknowledge my thesis examining committee members, Prof. Hani Naguib from University of Toronto, Prof. Fathy Ismail, Prof. Mohammad Kohandel, and Prof. Hamid Jahed from the University of Waterloo, for their time of reviewing my thesis.

My sincere thanks also goes to the technical team in the Department of Mechanical and Mechatronics Engineering at University of Waterloo, electronic technologists James Merli who's helped us from the beginning in modifying the tube furnace to meet the CSA requirements, Andy Barber for helping us in diagnosing the trouble shooting in the 3D Printer, Robert Wagner for helping us in the manufacturing some parts, Mark Griffett for his help and support in conducting the compression test, Yuquan Ding for the microstructural observation of the samples using the (SEM), Martha Morales for her IT support.

Thanks from the heart to the late King Abdullah for allowing me the opportunity to pursue the doctoral degree through the King Abdullah scholarship program. I would also like to extend my thanks to the Saudi Arabian Cultural Bureau in Ottawa, the University of Umm Al-Qura for the financial support I've received from them. Also, I would like to acknowledge the funding support received from the Natural Sciences and Engineering Research Council of Canada (NSERC), grant # RGPIN312074 37063 and NSERC Discovery grant # 283181-09 37188.

I really appreciate the support and the coordination provided by my colleagues at the Multi-scale Additive Manufacturing Laboratory and would like to thank, Dr. Yaser

Shanjani, Dr. Hamidreza Alemohammad, Dr. Mihaela Vlasea, Elahe Jabari, Amir Azhari, Esmat Sheydaeian, Richard Liang, Farid Behzadian, and Farzad Liravi.

Thanks are also extended to Prof. Julie Gough and Louise Carney from the Manchester University for conducting the biological study in their site.

I also want to extend my deep and sincere gratitude to my beloved parents, Ali and Wafa who dedicated to rise me up loving the science and learning me the doctrine of "nothing is impossible" from which I'm inspiring the self-esteem and patience in overcoming the obstacles. Thanks to my brothers, Saeed and Basim for taking care of my parents and own interests up there. An extended thanks to my beloved sisters for their support to me. I would also like to thank my family in law for their understanding our circumstances to be away from them the past few years. My sincere thanks go to my lovely wife Maram, who inspired me and provided constant encouragement during the entire degree program, deep thanks for her understanding and patience. I would like to thank my little boy, Ali, who missed out a lot of times due to my research and hopefully I compensate him for this time in the future.

Last but not the least, I would like to thank all my friends who supported me here in Canada and anyone prayed for me to be successful in my career.

Dedication

“To my beloved people; mom, dad, wife, brothers, sisters, son, nephews, and nieces
I am very proud to dedicate this work to all of you,,,”

Contents

List of Figures

List of Tables

Chapter 1 Introduction

1.1 Motivation

Life is all about change; lifestyle changes can significantly impact our habits, which, in turn, can negatively or positively affect our health. Obesity can be the result of a lifestyle change. In addition, the improvement in the quality of life that resulted from the development in the health care system led to aging of the entire population. This aging of population and an increase in the rate of obesity are the main causes of the increase in degenerative arthritis (osteoarthritis)[1,2].

Over 10% of Canadians over 15 years of age suffer from osteoarthritis [3]. The severity of this joint disease varies between mild, moderate and severe, where severe osteoarthritis requires total joint replacement surgery [1].

According to the Annual Report of the Canadian Joint Replacement Registry of 2014, osteoarthritis accounted for 76.5% of hip replacement surgeries and 97.1% of knee replacement surgeries[4]. In 2012-2013, hip replacements increased by 16.5% and knee replacements increased by 21.5% as compared to the previous five years[4].

The success of joint replacement surgery relies on an implant lasting longer than when the patient returns for revision surgery. The revision surgery is more sophisticated than the first implantation surgery[5].

According to 2012-2013 data, the rate of Canadian citizens who required a revision after conducting joint replacement surgery were 26.3% for hip and 22.5% for knee surgeries.

The most common reason for the revision surgery is an aseptic loosening or a failure in the bonding between the host bone and the implant[4]. Joint replacement surgery costs the Canadian healthcare system $963 million annually [4].

Osteoarthritis is one of the most common joint diseases. It can lead to a total joint replacement with a proper bone implant. However, the needs for bone implants are not limited to joint disease. There are many other reasons require bone implant to restore the functionality of a lost or defected part of bone such as trauma, accidents and war causalities. Consequently, the demand for bone implants is increasing. As such, designing and manufacturing proper bone implants is important. This bone implant should satisfy the needs of the users in terms of physical and mechanical properties that mimic real bone properties in order to avoid a loosening of the implant.

In order to alleviate the stress shielding effects which typically lead to loosening of the implant, the implant should be comparable to bone in terms of its mechanical and physical properties. Thus, two main crucial factors that ensure successful bone implant are porosity and stiffness. Proper amount of porosity ensures effective bone integration, and comparable stiffness to bone avoids the surrounding bone resorption. Also, the porous structure should include/mimic conformal channels which deliver the blood and minerals to the cells in the real bone structure.

Several conventional techniques have been used to produce porous Ti structures. Unfortunately, no single technique satisfies the objective of creating a porous structure with controllable porosity and mechanical properties. The best solution to overcome the above-mentioned issue and fabricate a customized implant is to use the additive manufacturing (AM) technique. AM technique is considered a promising alternative for precise fabrication of internal and external features of scaffold architecture.

Costly AM techniques, particularly laser or electron beam-based techniques, have been used in the fabrication of bone scaffold on a small scale. In addition to the high cost of these techniques, the difficulty in removing residual material is considered the primary

limitation which prevents these techniques from being applied on a large scale. However, the powder bed inkjet-based technique is an economical choice to 3D print a Ti porous structure. In comparison to its counterparts (>US $600,000), the powder bed inkjet-based technique costs (US $40,000)[6]. Also, there is almost 50% savings in the operating cost as represented in the consumable material or Ti powder, because the inkjet-based printing technique does not require a specific powder and the commercially pure Ti works very well. Thus, this economical factor makes this technique superior for the fabrication of a highly complex Ti structure. This manufacturing technique is an appropriate option to be used throughout the world, such as in developing countries where the costly additive manufacturing technique is not available. Also, this technique is a green technology which does not require any intrusion of laser during processing. At present there is a shortage of information in the literature about using the powder bed inkjet-based technique in the fabrication of titanium bone implants. To address this gap in the literature, the following objectives will be achieved.

1.2 Objective

The aim of this thesis is to utilize the powder based ink-jet printer in fabricating a Ti porous bone implant for load bearing purpose. The feasibility of using this approach to fabricate bone implant is assessed by conducting the following characterization techniques on the produced samples:

-Mechanical properties of the fabricated scaffold are characterized by using various methodologies such as compression test and shear test.

-Physical properties such as the porosity of the structure are characterized by using Archimedes principle. In addition, the dimensional variation of the structure is assessed.

-For microstructural examination, the Scanning Electron Microscope (SEM) is used to visually assess the microstructure. The Energy Dispersive X-ray spectroscopy (EDX) is used to characterize the chemical composition of the structure.

Based on the result of the characterization, a development on the produced structure is implemented by considering the following aspects.

Material Processing: The influence of several parameters are investigated including sintering temperature, sintering duration, binder content, powder shape, powder distribution, and powder size.

Structure: The architecture is assessed and the influence of the macro channels in the structure with different orientations on the physical and mechanical properties is investigated.

Manufacturing: Manufacturing parameters such as the layer thickness of printing and the optimum layer thickness for a certain powder size are investigated and a new approach of additive manufacturing is introduced.

1.3 Outline of thesis

This thesis consists of seven chapters. The first chapter presents the introduction and describes the motivation for and objective of the thesis. Chapters two through six illustrate the studies that have been conducted. The connections between these studies are shown in Figure 1-1. The second chapter provides an overview of the literature and background in which bone implant materials, manufacturing techniques, and bone and implant characteristics are reviewed. In the third and fourth chapters, different material and manufacturing processing parameters are investigated in an attempt to meet the physical and mechanical properties of bone. The fifth chapter focuses on the creation of macro channels in order to enhance the osseointegration process and address the influence of these channels on the physical and mechanical properties of bone implant. The sixth chapter introduces a novel technique of manufacturing macro channels. Finally, chapter seven offers the conclusions of this thesis and suggests opportunities for future work.

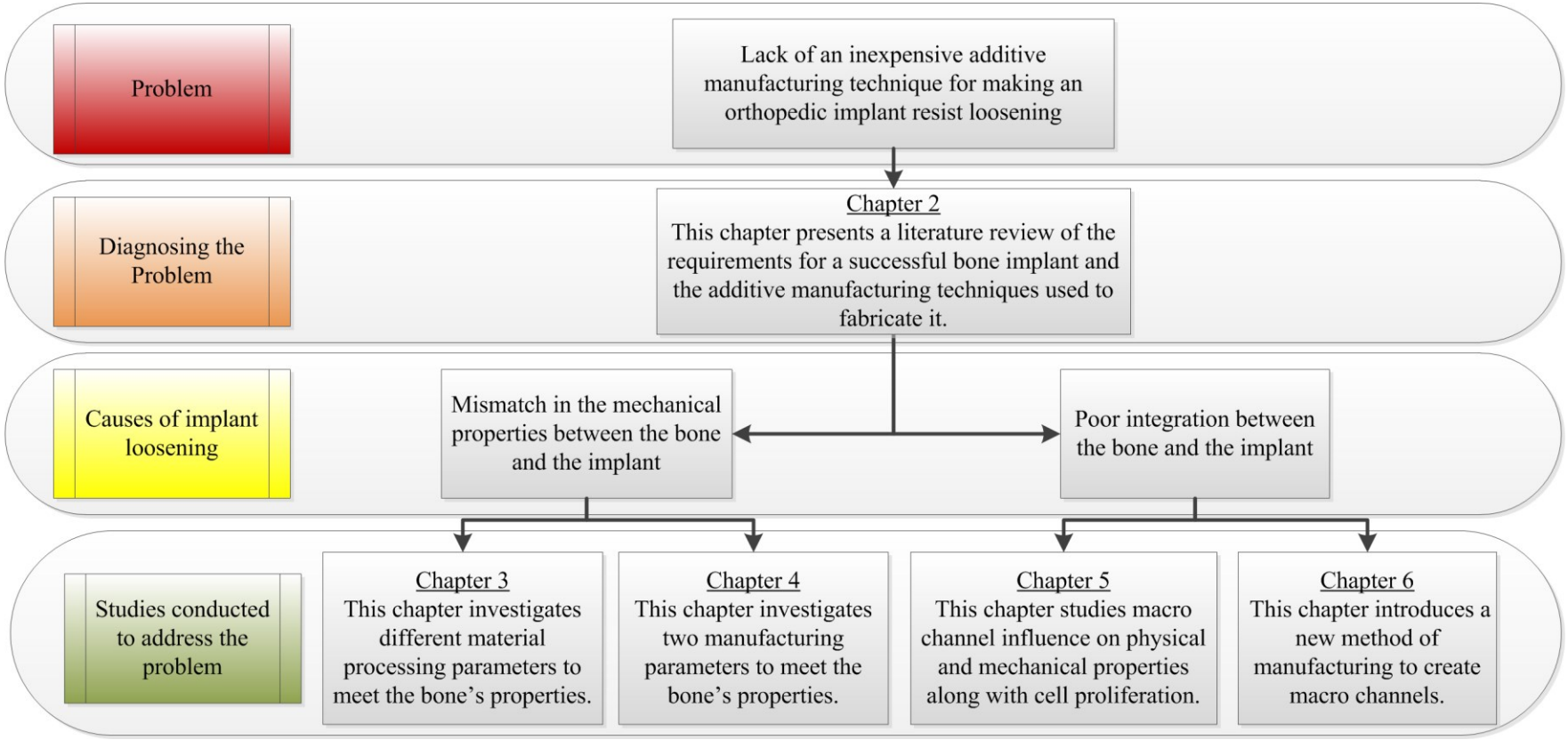

Figure 1-1 This flow chart defines the problem, identifies the causes of the problem, and lists the studies that have been conducted in this thesis to alleviate this problem.

Chapter 2 Additive Manufacturing for Bone Load Bearing Applications

2.1 Need for bone substitutes

The incentive behind fabricating constructs with a direct application in bone and joint reconstruction surgeries lies in understanding the demand for such devices. Bone and cartilage conditions, such as arthritis, osteoporosis, traumatic musculoskeletal injuries, spinal injuries, and spinal deformities [7], although mostly nonlife-threatening, can become very incapacitating, diminishing the quality of life of the affected individuals by causing ongoing pain, discomfort, inflammation, and restrictions in range of motion [7]. Furthermore, these conditions represent a major financial burden on the healthcare sector[7,8]. The current conventional treatment for advanced joint and bone trauma is to fully or partially replace the affected area with tissue grafts[9] or with artificial prosthetics[10] to restore near-normal functions. Current state-of-the-art prosthetic implants fail to meet structural and functional requirements that would render them as permanent remediation solutions[10]. As a result, thousands of patients undergo painful and costly subsequent surgeries for implant replacements or readjustments. Cell-based or tissue graft solutions have been proven to ameliorate the quality of life of patients, but are limited in terms of size and anatomical shape of defect that can be addressed, as well as the availability of healthy donor tissue and morbidity of the donor site[9,11,12]. There is a pressing need for more successful bone and osteochondral reconstruction approaches that take into account biochemical, morphological, and anatomical factors. One such approach focuses on manufacturing biocompatible and/or bioresorbable bone substitutes with complex internal and external architecture and appropriate biochemical cues that can enhance or replace

the defect area, gradually mature, and seamlessly integrate with the native tissue [13]. The bone substitute would serve as a biocompatible template that would encourage cell migration, proliferation, and differentiation, ideally acting as a temporary bioresorbable porous support until the bone matrix is regenerated [14]. A vast amount of work has been done in materials research and manufacturing methodologies in this field, specifically in constructing bone substitutes for load bearing applications; however, there is still a gap in understanding the ideal relationship between the scaffold morphology (pore size, shape, and interconnectivity), transient biochemical interactions, and mechanical properties [14,15].

2.2 Compositional, Structural and mechanical properties of bone

2.2.1 Compositional Properties of Bone and Requirements for Bone Substitutes

Bone is a dynamic and complex organ, encompassing a variety of tissues such as mineralized osseous tissue, cartilage, endosteum, periosteum, marrow, nerves, and blood vessels[16]. The main role of the bone network is in providing the necessary mechanical support, movement, and protection, with other roles ranging from blood production, to storage of mineral materials, pH regulation, and housing multi progenitor cells[16,17]. Due to the complex nature of the bone as biological system, in the context of fabricating bone substitute implants, the focus is generally on understanding the biochemical and structural makeup of the bone extracellular matrix (ECM), as well as the interaction of the ECM with cells and the environment in which they reside[17]. The bone ECM is in essence a composite material comprised of carbonated apatite (~69% of the ECM), mainly hydroxyapatite (Ca10(PO4)6(OH)2) crystals, entrapped in an organic matrix (~22% of the ECM) of mostly type I collagen, and water (~9 % of the ECM)[17,18]. Lipids, proteins, and osteogenic factors also reside in the ECM organic matrix[18]. From a compositional point of view, the bone substitute matrix should be at least biocompatible with the ECM, cellular, and chemical environment, osteoconductive to encourage fast bone ingrowth from surrounding healthy tissue[19], as well as nontoxic, nonmutagenic, noncarcinogenic, and nonteratogenic [20]. Ideally, the material should be osteoinductive to promote formation of new bone at the site [16,21].

2.2.2 Structural Properties of Bone and Requirements for Bone Substitutes

Structurally, the bone ECM is comprised of two main zones with very different morphological properties. Trabecular bone, also known as cancellous bone, is a highly porous bone matrix, with interconnected porosities between 50–90% and visible macropores in the range of 500–1000 mm [22]. Trabecular bone has a complex and organized porous architecture, with trabeculae following the direction of mechanical stress[16] as a direct result of adaptations to mechanical loading, as postulated by Wolff's law [10] and the mechanostat theory [23]. Trabecular bone encloses bone marrow and is enclosed by cortical bone. Cortical bone ECM has a compact solid-like structure, with enclosed vascular Haversian canals, having a low porosity between 3–12%, and pores <500 mm[22]. Cortical bone has a solid structure with a series of voids, for example Haversian canals, with a 3–12% porosity (typical apparent density values for proximal tibial trabecular bone 0.30 ± 0.10 g/cm^3). The bone ECM is constantly remodeled by the cells that reside in it, where osteoblasts are responsible for producing and mineralizing new bone matrix, osteocytes work on maintaining the matrix, and osteoclasts are responsible for resorbing the matrix [22]. From a structural standpoint, in designing a bone substitute, it is necessary to consider a gradient in porosity and mechanical properties, from a dense external configuration matching the characteristics of cortical bone to the highly porous region with interconnected porosity matching the characteristics of cancellous bone [24]. This means that an ideal bone substitute must have a heterogeneous porous structure, with varying physical and mechanical characteristics. In addition, the implant must also be designed to have an anatomically accurate three-dimensional shape in order to maintain a natural contact load distribution post implantation [11].

Table 2-1 Range of Mechanical Properties for Human Cancellous and Cortical Bone [16,21].

Bone Type	**Tensile Strength (MPa)**	**Compressive Strength (MPa)**	**Young's Modulus (GPa)**
Cancellous bone	N/A	4–12	0.01–0.5
Cortical bone	60–160	130–225	3–30

2.2.3 Mechanical Properties of Bone and Requirements for Bone Substitutes

The high level of porosity and pore interconnectivity that is ideal for a bone substitute may be limited by the mechanical strength requirements for that specific implant, especially in the case of load bearing applications. The bone substitute should provide physical support, starting from the seeding process in vitro until the tissue is remodeled in vivo. Furthermore, the implant must provide sufficient mechanical support to endure in vivo stresses and load bearing cycles[13]. Table 2-1 summarizes the range in mechanical properties of human cancellous and cortical bone.

2.3 Difficulties in Achieving an Ideal Bone Substitute

Manufacturing of optimal porous bone substitutes from a biochemical, structural, and mechanical properties point of view is highly complex due to a collection of factors. From an architectural standpoint, the bone substitute supports biological and mechanical functions [14], which may be in conflict. For example, for increasing the load-bearing property of the material, a denser material is needed, which conflicts with the requirement of having a highly porous matrix to encourage bone ingrowth and fluid permeability[22]. What is generally defined as an optimization of scaffold properties is likely a tuning of a single parameter with little regard to how other scaffold properties are modified. Furthermore, characterizing, digitizing, and manufacturing the scaffold architecture are difficult tasks. Using characterization methods to reveal pore surface, pore volume, pore shape, interconnectivity, and volume porosity in bone tissues[14], and furthermore translating such data into a digital format that can be interpreted into fabrication methodologies in a continuous or discrete fashion can be a challenge. Typically, the interconnected macroporosity should be >50 μm[14,18,21,22,25,26], with a specific orientation to match the stress loading conditions and fluid and nutrient transport mechanics[14]. Also, what is defined as microporosity, with a diameter ranging between 0.1–10 μm [14,18,22] has shown an effect on the biological response of scaffolds, thus the pores at this scale should be characterized and integrated in the final design. From a structural standpoint, it is also necessary to implement a gradient in porosity and mechanical properties, from a dense external configuration matching the characteristics

of cortical bone to the highly porous region with interconnected porosity matching the characteristics of cancellous bone [15,16,24]. Manufacturing methodologies that can incorporate the interpretation and implementation of digital data at a macro and micropore scale are of concern.

Another issue related to manufacturing the appropriate bone substitute architecture lies in the development of appropriate software interpreter design strategies[27–29] that can convert the desired structural porous morphology and mechanical properties of the bone to be replaced, into appropriate voxel units that can be fabricated using various manufacturing platforms. Such voxels may be computed mathematically using topology optimization algorithms [27,30] or numerical simulation [29].

From a material standpoint, difficulties arise in designing structures that can bioresorb in vivo at an appropriate rate matching bone remodeling. In the context of regenerative medicine, the terminology of materials with biodegradable, bioresorbable, bioerodible, and bioabsorbable [13] properties are often used. The biodegradation pathway will have an effect on the mechanical, structural, and biochemical properties of the scaffold, and needs to be fully understood [14]. Some of the parameters that affect the degradation rate are pore size, pore interconnectivity, permeability, scaffold shape, and volume, as well as implantation location within the musculoskeletal system. Furthermore, the long-term native tissue response to the degradation products should also be considered [14]. To add to the difficulty of producing an ideal implant, the overall biochemical, structural, and mechanical properties of the bone substitute should match patient-specific needs such as age, gender, health, metabolism, implant location, and loading conditions [14].

2.4 Metallic Bone Substitutes

2.4.1 Metallic Materials, Limitations and Opportunities

For a long time, metals were the main material utilized for orthopedic implants. This interest in metals resulted from the excellent physical and mechanical properties that are intrinsic to metals. At present, the interest in nonmetallic materials has prompted the fabrication of tissue scaffolds. These materials are mostly polymer or ceramic, and are

used to produce biodegradable scaffolds. Biodegradable scaffolds can be useful for young patients, because they have high growth rates of tissue to restore the functionality of the damaged area. However, the case is completely different for senior citizens, who have very low tissue growth rates. When faced with a certain degradation rate of the materials, this may cause a mismatch in terms of the mechanical properties[31]. Therefore, permanent metallic bone substitutes are more appropriate in the case of older patients. Several metals have been used for implants, such as stainless steels (316L), Co-Cr-Mo, pure titanium, titanium alloys, and tantalum. Each metal has advantages and disadvantages that can either expand or limit its usage.

Stainless steel is considered one of the first metals used in the orthopedic field as plates and screws for bone fixation in the early twentieth century[32]. The most popular stainless steel alloy used in prosthesis fixation is (316L), with moderate strength and toughness in comparison to other metals as shown in Table 2-2. This alloy is distinguished by good corrosion resistance in comparison to other steel alloys, since the 12% Cr in its content forms a corrosion protective layer Cr2O3 on the surface [33]. This metal is both widely available and economically effective in terms of processing and manufacturing [34,35]. However, as the wear resistance of stainless steel is very low, its usage in hip replacement was stopped [36]. Nowadays, stainless steel is rarely used for orthopedic implants. Instead, stainless steel is used for temporary fixation devices such as nails, screws, and plates due to the superiority of other metals such as Ti, Ti alloys, and Co–Cr alloy in terms of mechanical properties and corrosion resistance [36].

Table 2-2 Comparison of the Mechanical Properties of Different Metals [37].

Material	Bone	Magnesium	Co–Cr–Mo and Alloys	Ti and Alloys	Stainless Steels
Density (g cc−1)	1.8–2.1	3.1	8.3–9.2	4.4–4.5	7.9–81
Compressive strength (MPa)	130–180	65–100	450–1896	590–1117	170–310
Elastic modulus (GPa)	3–20	41–45	200–253	55–117	189–205
Toughness (MPam1/2)	3–6	15–40	100	55–115	50–200

Another widely used metal in the orthopedic industry is Co-Cr-Mo alloy that is characterized by a high level of mechanical strength, fatigue strength, wear resistance, and low cost of production[35,36,38]. While these advantages are considered beneficial for some applications, this is not generally true for orthopedic implants, since this metal's high strength and elastic modulus has caused a stress shielding between the implant and the bone due to the mismatch of mechanical properties. Moreover, the high level of metal ions that are released and the nanoparticle debris which is caused by the wear, negatively affect the biocompatibility of this metal [35,39]. Despite these drawbacks, this metal is the most preferable in hip replacement due to its high level of wear resistance compared to the other metals. In particular, this material is used to fabricate the femoral head and acetabular cup which is an area of high friction[36]. In addition, dentists have some interest in this metal as a coating for some dental devices [34].

NiTi (nitinol) is a shape memory alloy, which means it can restore its original shape after a plastic deformation by using a heat treatment. This alloy was introduced in 1960 and is characterized by high strength, superelasticity, and good corrosion resistance [36,40,41]. However, the release of the Ni ions limits its usage as an orthopedic prosthesis due to the possibility of toxicity and the inflammation effect of the surrounding tissue. This has led researchers to treat the surface through exposure to the oxidization process in an attempt to create a protective layer free of Ni [36,41,42].

Alternatively, degradable metals have captured the interest of some researchers. One of these metals is magnesium (Mg), which is characterized by having low elastic modulus. In addition, Mg is an osteoconductive material and it does not show any inflammatory effect following fixation [43]. However, as Mg is a degradable material, the dissolved particles may cause toxicity, which could limit its usage in orthopedic applications [44] .

Titanium (Ti) was introduced in the orthopedic field in 1965 in the form of screws and plates. This long period of usage illustrates the preference of using Ti, as supported by long-term clinical data, which indicates this material's good biocompatibility. Moreover, Ti is characterized by a nano-oxide layer covering its surface that increases in vivo osteointegration [45]. Indeed, from a biological aspect, Ti has proved its compatibility more so than stainless steel or CoCr, as proven by the cell culturing of these metals [45].

Overall, Ti is considered one of the strongest and highest corrosion-resistant metals. Moreover, Ti is characterized by an excellent strength to weight ratio and good toughness [36,46].

Recently, it has been noted that the science community is concentrating on Ti alloys, in particular, Ti-6Al-4V, to fabricate bone substitute scaffolds. This interest originates from the good mechanical properties and biocompatibility of this alloy. The presence of aluminum (Al) and vanadium (V) in this alloy improves the mechanical properties compared to commercially pure Ti (CP Ti)[36]. One of the most important benefits of Ti and its alloy (Ti-6Al-4V) is its relatively low elastic modulus which is the half of the Co–Cr modulus, which could assist in reducing the effect of the stress shielding [46]. Despite the fact that Ti has a low elastic modulus in comparison to other metals, the mismatch between bone and implant still exists [46]. Arguably, the presence of V in this alloys is a source of concern, since V is toxic [44,47]. Further drawbacks of Ti and its alloys include the expensive machining cost and the sophisticated heat treatment process [36]. Nowadays, most dental implants are fabricated from CP Ti, and Ti-6Al-4V are used in orthopedic applications[36].

In order to eliminate the effect of V in Ti6Al4V alloy, new Ti alloys have been developed to overcome the toxicity issue, such as Ti-6Al-7Nb, Ti-5Al-2.5Fe, Ti-35Nb-5Ta-7Zr, Ti-35Nb-5Ta-7Zr-0.4O, and Ti-15Zr-4Nb-4Ta. For instance, Ti-15Zr-4Nb-4Ta has shown excellent mechanical properties, biocompatibility, and good corrosion resistance. In addition, it is likely that more bone was formed than that which formed around the Ti 6Al 4V when implanted on the bone marrow of the rat tibia [47]. Most of these alloys are still in the development stage in order to characterize the mechanical properties and biocompatibility for application in bone regenerative medicine [36].

Another material, tantalum (Ta) is considered one of the best metals in the orthopedic field due to its fairly low Young's modulus, high corrosion resistance, and excellent biocompatibility [48]. A recent study comparing Ta and Ti showed that Ta is superior compared to Ti in regards to cell integration with a controllable Young's modulus in the range of 1.5–20 GPa by changing the porosity of the structure [49]. However, the high cost of production and fabrication of this metal is the main obstacle limiting its usage in the orthopedic industry along with short-term clinical data[35,48].

Generally, the major constraints which can govern the success of a load bearing implant are biocompatibility, porosity, and proper mechanical properties. The highly important mechanical properties in the designing of a load bearing implant are Young's modulus and compressive strength. Other mechanical properties such as bending strength are less relevant in load bearing implant. However, certain properties such as fatigue strength are necessary for a long lasting implant, but are not as crucial as Young's modulus and compressive strength, since these properties may cause short-term failure of Implant [50].

2.4.2 AM of Metals for Bone Substitutes

Historically, conventional techniques were used to fabricate porous metals for several industrial applications. Once porous metal was introduced in early 1972 in the orthopedic field [51], scientists looked for ways to control and improve the properties of this metal foam. Consequently, several conventional techniques emerged. However, these techniques are not capable of precisely controlling the porosity and producing a scaffold with a predefined microstructure. Also, these techniques cannot produce a scaffold with a contoured external shape. In order to overcome these obstacles, additive manufacturing (AM) techniques are considered the most promising alternative for precise fabrication of internal and external features of scaffold architecture.

There are many AM techniques that have been used in the fabrication of metal scaffolds, such as three-dimensional printing (3DP), electron beam melting (EBM), selective laser melting (SLM), direct metal deposition (DMD), and selective laser sintering (SLS) [40,52–55]. Each technique has different opportunities and limitations. Some of these techniques rely on laser technology, and others rely on the injection of the slurry. The costs of production through these techniques are varied according to complexity. For example, the laser sintering methods are highly expensive due to their use of laser technology and the capability of producing a precise microstructure. Other techniques appropriate for fabricating a scaffold have acceptable microstructure details, such as fiber deposition and 3DP.

SLS is an AM technique (Figure 2-1) that works by sintering very fine layers of metal powders layer over layer using a CO2 laser beam, either directly or indirectly. In direct

SLS, the powder mixture is a compound of two metals: a low sintering temperature metal and the main metal [56]. In this technique, the laser beam melts the low sintering temperature metal and uses it to bind the main metal particles to each other. For instance, in a study where NiTi dental implant was fabricated using DMLS, the base metal was Ti and the binding agent was Ni [40]. The second technique is called indirect SLS, where a preprocessing of the powder is required to coat the metal powder particles with some polymer to work as a binding agent of the green sample. This technique requires a postprocessing of the green sample by debinding the polymer from the green sample followed by the sintering of the metal particles in a shielded environment at a very high temperature. The diversity of materials produced by this manufacturing method is one of the most important advantages of this technique [57]. The final product resolution is moderate since heat transfers to the adjacent area and fuses extra particles to the targeted area, which might lead to a limitation in the accuracy according to the size of particles [57,58]. Economically speaking, fabrication using SLS is costly [35]. Technically, SLS is considered a lengthy manufacturing method, since it requires preprocessing of the powder and the laser sintering process is time-consuming. In addition, the resulting product may require a postprocessing heat treatment that usually takes hours to complete [56,58].

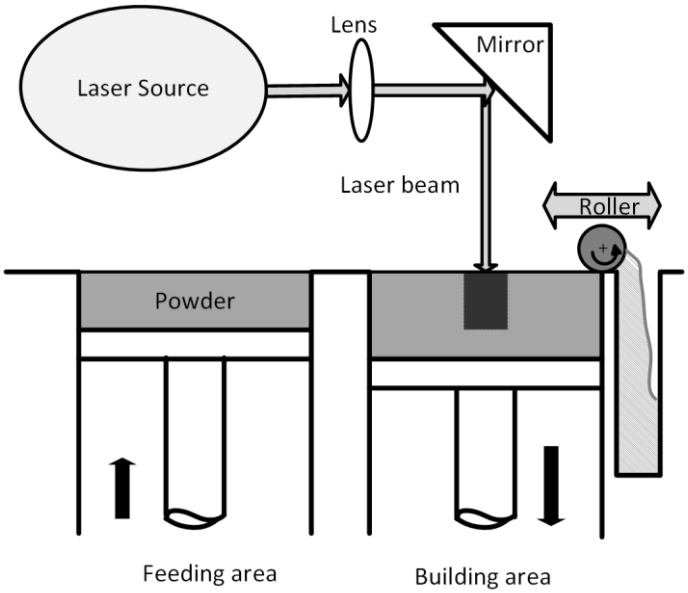

Figure 2-1 Schematic presentation of working principle of SLS technique.

Another complex technique, EBM, works based on the layering process similar to SLS. EBM differs from SLS in its use of an electron beam rather than a laser to sinter the powders, which is generated in a tungsten filament and is accelerated and controlled with a magnetic field [59]. This manufacturing technique is relatively fast and the building of samples takes place under vacuum [44]. It offers an attractive opportunity in the fabrication of fully dense or porous parts due to several controllable parameters such as beam current, scan rate, and sequence variations [53]. In this technique, an additive or fluxing agent is not required to fulfill the melting process because the electron beam is powerful enough to raise the temperature of the particles to the melting point [59]. However, there are still some limitations in this method such as the low dimensional accuracy and surface quality due to shrinkage. Additionally, this technique is costly, and removing the excess material inside the structure can prove difficult [60]. Different metals have been fabricated using EBM, such as Cp-Ti, Ti-6Al-4V, and Co/Cr for orthopedic implant and maxillofacial surgery [44,59].

Similarly, SLM utilizes the same mechanism of the EBM, and a wide range of materials in powder form can be used [44]. Moreover, SLM is able to produce solid and porous parts based on the laser energy density [54]. Also, this technique is free of binders and fluxing agents, so there is no need for a postprocessing step [44,56,61]. Unlike EBM, SLM uses an ytterbium fiber laser 200 W power and uses Ar or N in the building chamber, which may increase the thermal conductivity and maintain a consistent rapid cooling of the printed zone more than EBM [54,62]. However, high production cost, lengthy fabrication time, and difficulty in removing the trapped powder are the major limitations of this technique [35,44,56]. Furthermore, the vaporization phenomenon is one of the drawbacks of this technique. This phenomenon is generated due to the high temperature of the molten pool caused by the laser beam evaporating the particles. This leads to an overpressure in the molten pool, which results in spewing of some molten metals out of the pool [56]. Today, this technique is utilized in the aerospace industry, orthopedics prostheses, and dental implants [61].

In the same context, laser engineering net shaping (LENS) and direct metal deposition (DMD) are both AM techniques used in manufacturing bone substitutes. These techniques mainly depend on laser technology to fuse the metal powder. LENS systems

use a neodymium–yttrium–aluminum–garnet (Nd:YAG) laser, while DMD uses the CO2 laser beam. The powder feeding systems are completely different, since the powder feeding in the DMD comes through a concentric ring at the tip of the laser nozzle, while in the LENS the powder comes through different powder feeders to the melting zone. Both techniques use an inert gas during the manufacturing process to avoid oxidation [55]. With these techniques, it is possible to use a wide range of metal powders such as stainless steel, nickel-based alloys, Ti and its alloys, tooling steel, copper alloys, alumina, or a combination of these [57,58,63]. Thus, LENS can be useful for the repairing or re-manufacturing process that cannot be implemented by other AM techniques [57]. LENS and DMD work through the process of depositing the metal layer-over-layer. Both are similar in terms of processing; however, the high cost of DMD has boosted LENS's popularity. The need for support structures for overhanging features is one of the limitations of the use of these techniques in the fabrication of orthopedic prostheses[58]. Another drawback is the residual stress caused by the rapid heating and solidifying process[57].

Many studies have been conducted using two techniques: fiber deposition (FD) and 3DP. The two have been chosen mainly due to their manufacturing simplicity compared with SLS or EBM and cost efficiency. The base material of FD is metal powder. In the FD method, the powders are mixed with a solution to form the slurry which can be deposited from the machine onto a substrate. The scaffold is built by the process of layering from bottom to top. The FD technique requires postprocessing of the product by the sintering of the produced scaffold in a very high temperature furnace. When using FD in the fabrication of a scaffold, several parameters can influence the strength and the porosity of the structure, such as the gap between fibers, the fiber's lay down angle, and the nozzle's diameter [64,65]. The dimensional accuracy of the final product is poor compared to other techniques such as 3DP due to the wet nature of the fiber slurry, which leaves a high level of shrinkage after drying and sintering [66]. In fact, this technique is still in the experimental stage. One of the simplest rapid prototyping techniques is the ink-jet-based 3DP, as shown in Figure 2-2.

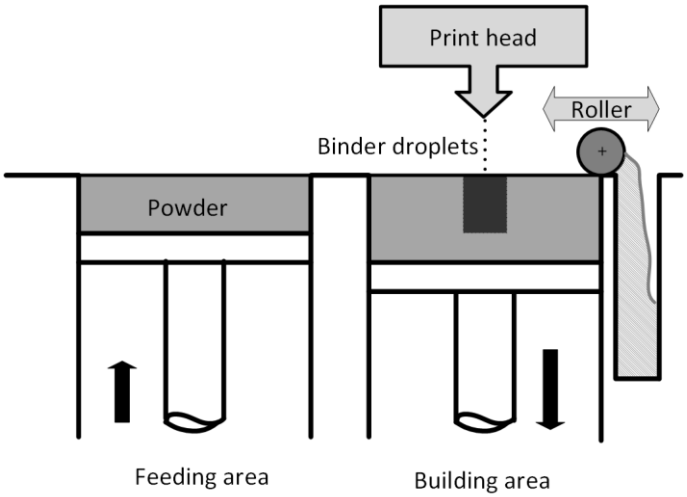

Figure 2-2 Simple sketch showing the working principle of the 3DP machine.

In this technique, the printer functionality is similar to an ink-jet printer, where instead of ink, a binder is dispersed through a print head on each layer of powder. Similar to previous methods, this printer works on a layer-by-layer basis, starting from the bottom and going up. The printer has two different powder zones: one for building the structure and the other for feeding the powder, so that when the feeding area goes up, the building area lowers down, moving a distance equivalent to the required layer thickness. A counter-rotating roller spreads the powder from the feeding bed over to the building bed, followed by the injection of the binder based on an image corresponding with the slice layer data of the 3D structure. This technique is very fast in the building process and is significantly cheaper than other techniques [58]. This machine was used indirectly to produce a porous metal scaffold by printing a sacrificial mold from alumina powder to cast the Co-Cr alloy which is then removed through several thermal and chemical steps[67]. Similarly, the same principle has been used to create a Ti scaffold and wax template as an alternative sacrificial mold [52]. This method of manufacturing provides a precise surface texture. However, the time- consuming process through the multiple stages of manufacturing is considered to be the main disadvantage of the indirect 3DP technique. This attempt has fascinated and motivated many researchers to replicate this success through direct printing of the desired metal scaffold, followed by sintering of the green part under a high temperature vacuum furnace [66,68]. This technique has fewer stages than indirect printing. With 3DP, several parameters are able to form the microstructure of the

desired part such as powder size, sintering temperature, and duration [66]. The layer thickness is primarily chosen based on the particle size and cannot be thinner than the largest particle in the powder [68]. However, the resolution is lower than the laser-based techniques because the binder penetrates the powders adjacent to the targeted area[58]. Difficulties in removing the trapped powder from the green part are the main disadvantage of this technique [58,66,68].

Using the 3DP method and CP Ti as a building material, the authors' group has been able to develop a set of optimized processing conditions to assure control over a microstructure and the associated mechanical and physical properties of the structure[66]. Material powder size is one of the most influential parameters on changing the strength and density of the structure, as shown in Figure 2-3. Also, the physical appearance of the final product is crucial in the fabrication of the orthopedic implant, since a high level of shrinkage in the implant is undesirable, and the particle size influences the shrinkage, as shown in Figure 2-4.

As a whole, AM techniques offer a good control over the manufacturing of the external and internal details of metallic bone substitute scaffolds, with limitations in the creation of complex internal interconnected macro pores [31].

2.5 Conclusions

Metals still form the bulk of primary bone substitute materials in the orthopedic industry. Interest in metal implants will remain strong in the future, especially for senior patients. The fabrication of metal implants is costly, but with new developments in the AM field, manufacturability may become easier.

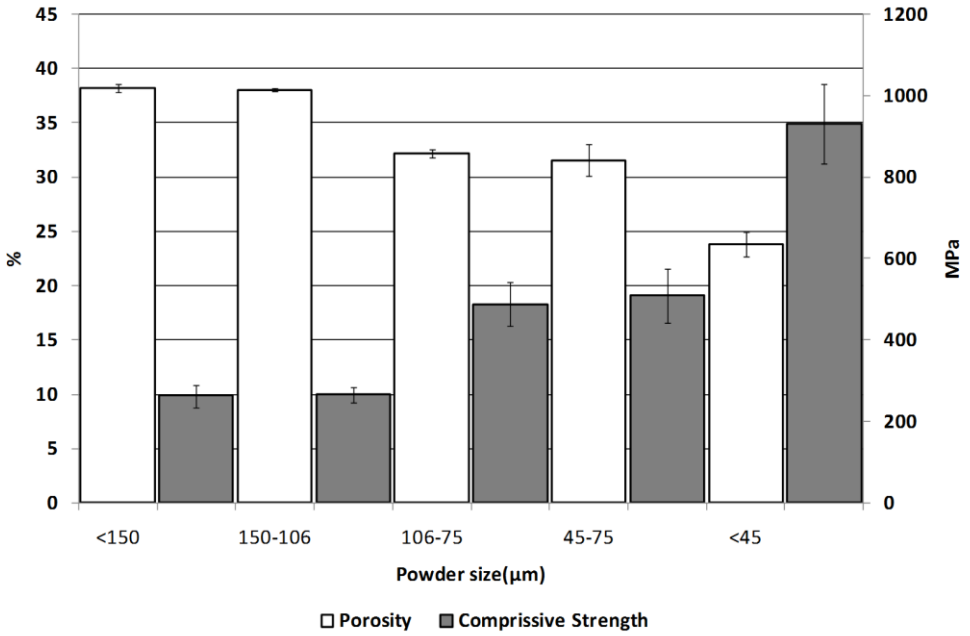

Figure 2-3 Compressive strength and porosity of the porous structures fabricated by varied sizes of Ti powder.

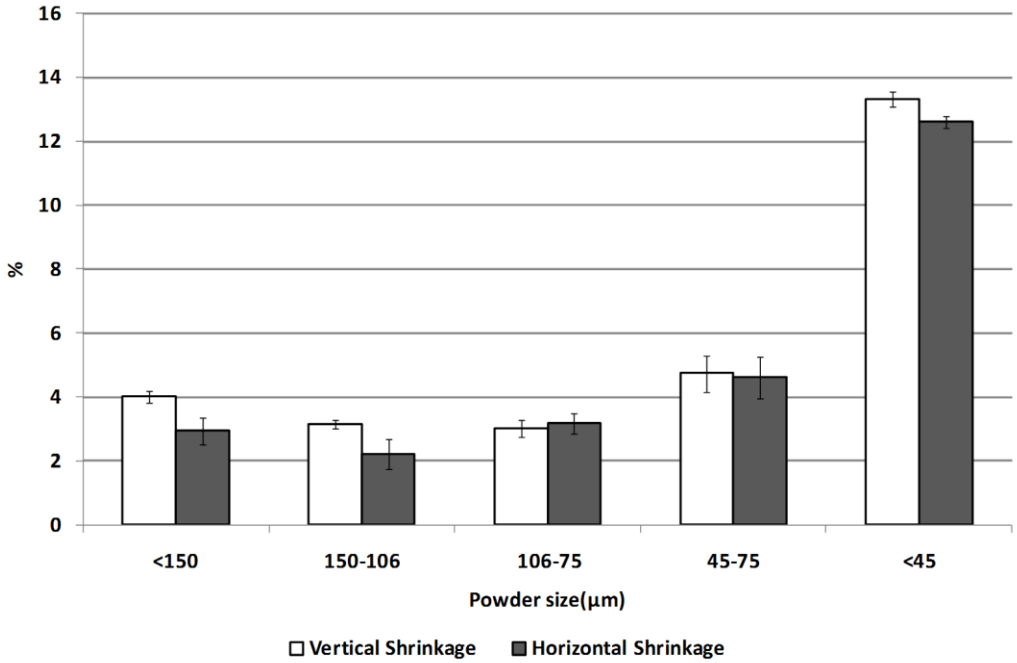

Figure 2-4 Vertical and horizontal shrinkage of Ti samples fabricated by varied sizes of Ti powder.

Chapter 3 Characterizations of additive manufactured porous titanium implant

3.1 Introduction

Aging of the world population is exponentially increasing, partly due to significant increase in life expectancy. Half of chronic diseases for elders over 65 years are represented by joint diseases and osteoporotic fractures[69]. The most common sites of osteoporotic fractures include the spine, hip and forearm [69].

Bone implants composed of bulk metals are commercially available and are used for the repair of large bone fractures/defects. Several metals have been used for this purpose such as stainless steels (316L), Co-Cr-Mo alloy, titanium (Ti) alloys, pure titanium and tantalum[44]. Each metal has advantages and disadvantages which can expand or limit the usage. However, the major drawback of the bulk metals is the stress shielding which is generated on the host bone due to a mismatch in the stiffness of bone and the implant [70]. In spite of the fact that the creation of implants from a material with low elastic modulus (such as Ti) reduces the stress shielding, the mismatch between bone and implant still exists[46]. An effective approach to eliminate this problem may be the use of porous metal structures. The amount of porosity in the implant is considered as the crucial factor promoting successful bone integration with porous structure.

Several techniques have been used to produce porous metal structures. Some of these techniques are conventional such as gas injection into the metal melt, plasma spraying, space-holder method, conventional sinter of metal powders, spark plasma sintering and replication of polymeric foams [44,46,50,71–73]. Other techniques which are more advanced and have the capability of controlling the external and internal structure. These

techniques are called additive manufacturing (AM) techniques such as three-dimensional printing (3DP) [52], electron beam melting (EBM)[53], selective laser melting (SLM)[54], direct metal deposition (DMD)[55] and selective laser sintering (SLS)[40].

Recently, AM of Ti structures via adhesive bonding 3D printing has been investigated [74]. In this method, a Ti green part is formed through 3D printing of irregular Ti particles followed by heat treatment and sintering to obtain high mechanical properties. Although this primary study showed the feasibility of the fabrication process and suitability of produced structures in terms of *in vitro* biological responses, no investigation has been reported related to the effect of process parameters on the porosity and physical quality of final porous implants.

In this work, a comprehensive study on the effect of material condition (such as Ti powder size and amount of the PVA) and manufacturing parameters (such the sintering temperature and time) on the physical, chemical and mechanical properties of porous Ti structures is presented.

3.2 Methodology

3.2.1Materials

The material used in the study to fabricate porous Ti structures was commercially pure Ti powder (CP Ti, Phelly Materials Inc., Bergenfield, NJ, USA). This powder meets the ASTM (F67-06 Grade 2) standards and was received in spherical shaped particle form with diameter in the range of 45-150 μm. Ti powder was sieved with mesh sizes of 200 and 140 (U.S. standard sieve series, Cole-Parmer, USA). The outcome of sieving process were four different categories of Ti powder: (A) As received powder, 45-150 μm, (C) Course powder, 106-150 μm, (M) Medium powder, 75-106 μm and (F) Fine powder, 45-75 μm.

In this study, polyvinyl alcohol (PVA) powder 86-89% hydrolyzed with low molecular weight (Alfa Aesar, Ward Hill, MA, USA) was used as a binder to bind spherical Ti particles together to fabricate rigid green parts before the sintering. PVA was received as a course powder and needed to be ground to < 63 μm to be similar or close to

Ti powder size. The grinding process was followed by sieving (U.S. standard sieve series, Sieve No. 230, Cole-Parmer, USA). The resulting powder was in the range of 63 μm.

The blending process of Ti and PVA was carried out using a jar-mill (LABMILL 8000 JAR MILL MACHINE, Paul N Gardner Company, USA) for 4 hours using two levels of PVA additions, that is, 3 and 5 wt %. During the screening phase, 10 wt % PVA was initially used that resulted in a very high porosity (~50% which was not desired as the goal of this study was to arrive at ~30% porous structures similar to cortical bone). Therefore, lower PVA percentage was selected for this study. To assure a homogeneous distribution of PVA within Ti powder, the blending process should be implemented according to a certain criterion. The method of blending must be chosen while considering the relation between the gravitational force and the centrifugal force to get a homogenous mixture [75]. It was found that the optimum mixing rate would be satisfied at 76% of critical rotation rate. The critical rotation rate occurs when the centrifugal force equals the gravitational force according to the following equation:

$$\frac{md\omega^2}{2} = mg \qquad (1)$$

$$\omega = 2\pi n \qquad (2)$$

where g is the gravitational acceleration (9.81 m s^{-2}), d refer to bottle outer diameter, ω is the angular velocity, m is the mass of bottle and n is the number of the cycle per minute. Transforming the linear velocity to a rotational speed and solving the above equation results in[75] ;

$$n = \frac{32}{\sqrt{d}} \qquad (3)$$

Thus, for a bottle with a diameter of 63 mm (which was used in this study), the optimum rotation speed of the jar mill (n) was adjusted to 128 rpm.

3.2.2 Manufacturing of green parts

The 3D model of a rounded bar with dimensions of Ø10.3×15.45 mm^2 was generated with the assistance of SolidWorks® Ver. 2006 (SolidWorks Corp., Concord, MA, USA). The model was exported in stereolithography (STL) format to 3D Printing machine.

The fabrication of the porous structures was conducted by a retrofitted powder-based 3D printing machine (ZPrinter310-Plus, Z Corporation, Burlington, USA). In the printer, the designed model was sliced by Zprint software into 2D layers. Three varied levels of layer thickness were chosen by considering the particles sizes in each category as listed in Table 3-1. To spread a layer of powder smoothly, the stacked-layer thickness should be larger than the largest particle in each category as shown in Figure 3-1(b).

At the beginning, the feed piston rose up in conjunction with the build piston which descended by the stacked-layer thickness. Then, a counter-rotating roller spread a layer of blended powder in the same thickness of the slice that had already been specified before the printing. Next, a print-head injected an aqueous solvent (Zb^{TM}58, Z Corporation, Burlington, USA) on the powder, causing the Ti particles to bind to one another and to the previous printed cross section. The feed and build pistons moved with the same sequence while the above process repeated until the entire sample was printed as shown in Figure 3-1(a). After the printing process, samples were left to dry for 1.5 h at 38ºC.

Table 3-1 Layer Thickness Which Used for Different Categories of Powder.

Powder Category	**Stacked-Layer Thickness(μm)**
(A) 45-150 μm	175
(C)106-150 μm	175
(M) 75-106 μm	125
(F) <75μm and >45 μm	100

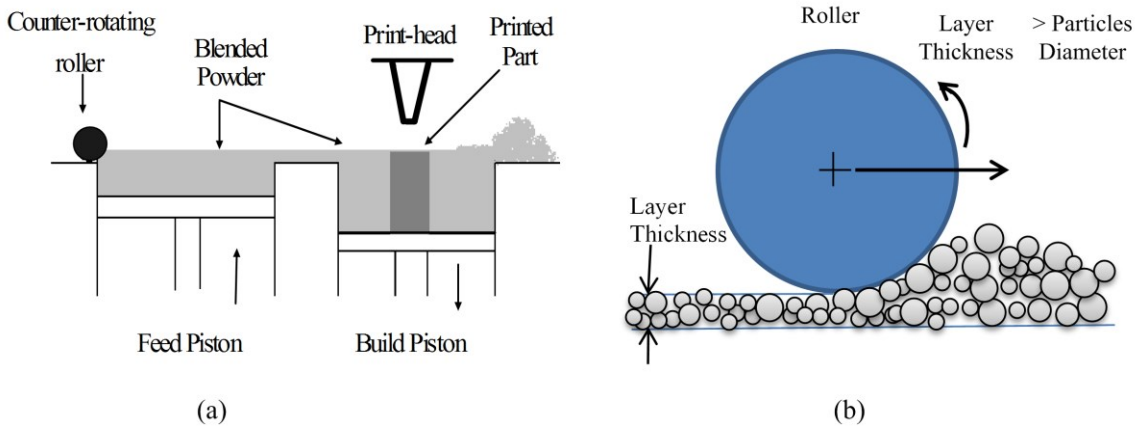

Figure 3-1 Schematic of (a) 3D printing process and (b) powder spreading and compaction by a counter-rotating roller. Layer thickness (i.e., the gap between roller and underlying powder layer) is chosen larger than powder particle size.

Using a brush, the samples were cleaned after drying. The cleaning was followed by blowing compressed air to the samples to ensure that all non-adherent particles were removed from the external surface.

3.2.3 Sintering

The sintering process was carried out in a MTI® High Temperature Tube Furnace (GSL—1500X-50, Richmond, CA, USA). The process started with burning the PVA at 295 ºC for 3 h with a heating rate of 10ºC min^{-1} as seen in Figure 3-2. Then, the tube was purged with high purity Ar gas (Grade 5) to avoid the oxidation of titanium under high temperatures. The furnace was adjusted to hold at 500 ºC for 1 h to ensure that the residual PVA in the samples were removed. Then, the furnace temperature was programmed to rise up to a targeted temperature of either 1100 or 1400ºC and was held for either 1 or 3 h. The surfaces of the sintered samples were slightly cleaned by a sand paper. Then, samples were immersed for 5 min in the ultrasonic cleaner bath filled with distilled water. After that, the samples were placed in an alumina crucible to dry in a regular oven at 130ºC for 2 h.

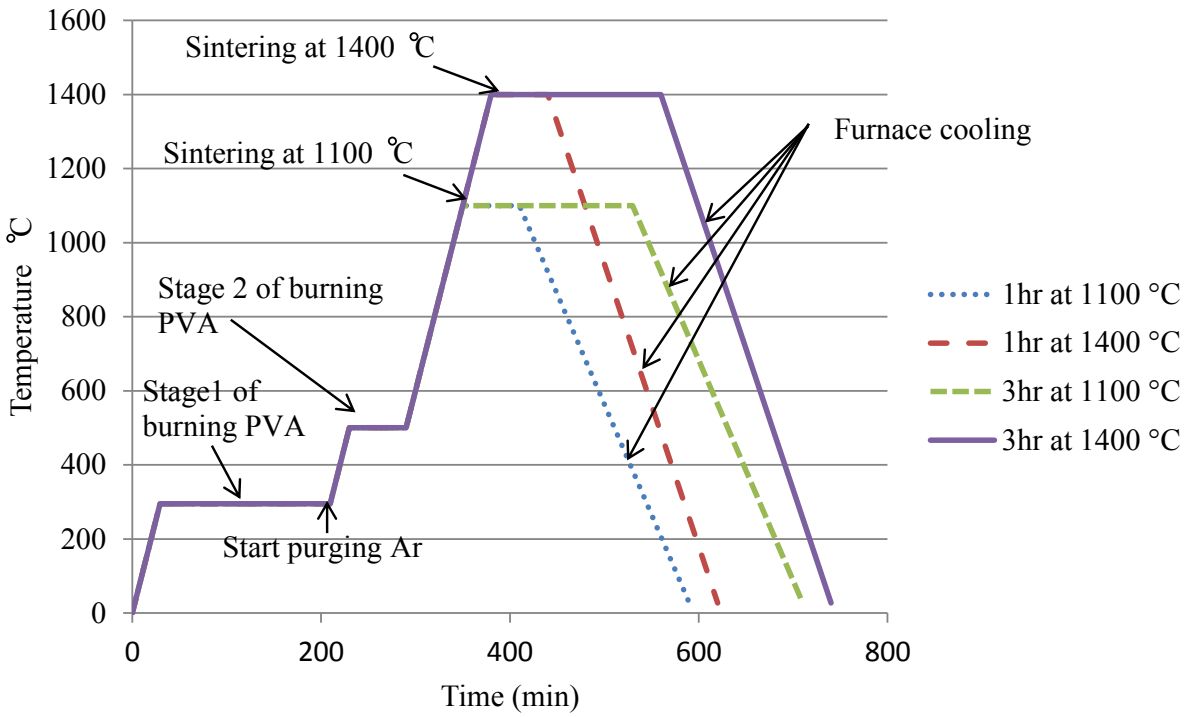

Figure 3-2 Sintering protocols which are followed in the sintering process.

3.3 Shrinkage Measurement

The geometrical features measurement was conducted to identify the shrinkage percentage on the material during the sintering process. This measurement was carried out using electronic Vernier caliper. The height and diameter of the samples were measured before and after the sintering process three times for each. The feature sizes were recorded and averaged from three readings. The percentage of horizontal (H%) and vertical (V%) shrinkage (shown in Figure 3-3) was calculated according to the following formula:

$$H\% = \frac{\text{Diameter}_{\text{After sintering}} - \text{Diameter}_{\text{Before sintering}}}{\text{Diameter}_{\text{Before sintering}}} \times 100 \qquad (4)$$

$$V\% = \frac{\text{Height}_{\text{After sintering}} - \text{Height}_{\text{Before sintering}}}{\text{Height}_{\text{Before sintering}}} \times 100 \qquad (5)$$

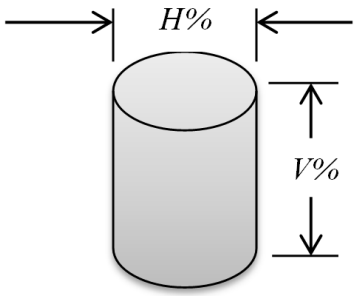

Figure 3-3 Schematic of horizontal and vertical shrinkage directions on the sample caused by sintering. Ti rounded bars were positioned in the sintering furnace as their main axis was along with the gravity direction.

3.4 Porosity Measurements

The porosity measurement was carried out according to ASTM B 311& C373 using Archimedes principle of buoyancy. The test was done by first measuring the dry weight , W_{dry} , using an electronic balance (APX-203, Denver Instrument, USA) with a precision of 0.001g. Then, sample was immersed in the distilled water and boiled for 3 h to extract the bubbles of air from the porous structure. Afterwards, the sample was kept in water for 12 h to ensure the removal of air from the entire structure. The sample was subsequently placed on the net of the Universal Specific Gravity Kit (Sartorius®, Bradford, MA, USA) which was submerged in water and weighted the sample's submerged weight W_{sub}. The sample then removed from the kit and weighted to obtain the wet weight W_{wet}. Finally, the porosity of the sample was calculated from the following formula:

$$\text{Porosity } \% = \frac{W_{wet} - W_{dry}}{W_{wet} - W_{Sub}} \qquad (6)$$

3.5 Mechanical Properties Measurements

Compression test was used to characterize the mechanical properties of the fabricated samples. This test was implemented by the uniaxial test machine (Instron-4206, USA) at room temperature. The machine was equipped with a 150 kN load-cell and the cross head speed was 1mm min^{-1}, corresponding to a strain rate of $1.0\times10^{-3}s^{-1}$. In this study, 4 rounded bars with diameters of ~ 10 mm and a length-to-diameter ratio of 1.5 (according to ASTM E9 – 09) were used to perform the tests.

3.6 Micro-structure Characterization

The microstructure characterization of the porous titanium structure was conducted using the scanning electron microscope (SEM) (JEOL JSM-6460) equipped with energy-dispersive X-ray spectroscopy (EDX) analysis (INCA 350 Microanalysis System).

The sinter necks among the particles in the SEM images were measured using ruler in the image processing tool box of MATLAB® to compare the neck ratio (neck size /particle size).

The characterization of the chemical composition of the produced samples was carried out by the EDX. This method of analysis discovers any contamination that the material may have been exposed to through the sintering process.

3.7 Results:

3.7.1 Structural Observation

A typical rounded bar sample with a diameter of 10 mm and height of 15 mm which was fabricated using the 3D printing machine is depicted in Figure 3-4.

Figure 3-4 Fabricated Ti sample with a dimension of Ø10mm×15mm.

The SEM images of the porous structure in Figure 3-5 shows Ti particles are bound together forming clusters of Ti when the additive PVA powder is used in the fabrication process.

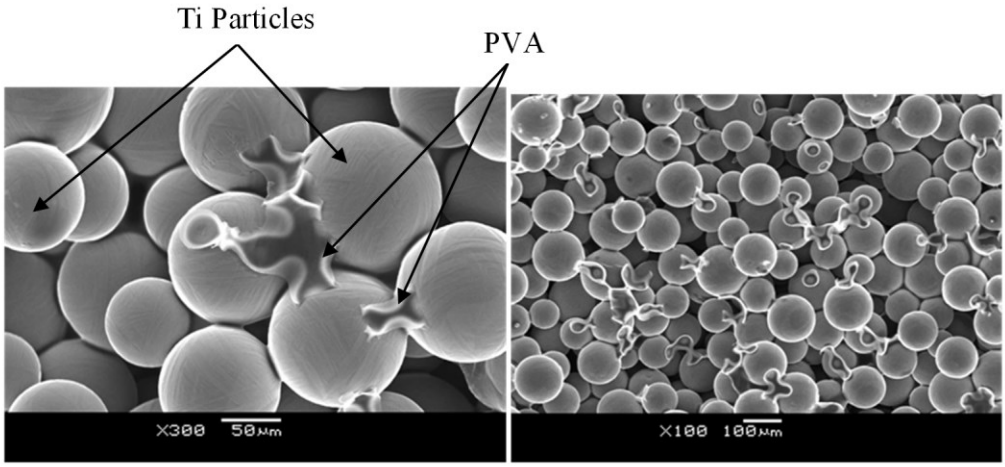

Figure 3-5 Micrograph of the green sample printed from category A of powder demonstrates the PVA binding Ti particles together before the burning process of PVA.

Figure 3-6 shows the microstructure of Ti samples after sintering. In Figure 3-6a, the neck among the particles had just started at 1100 ºC; however, Figure 6b shows that large necks have formed among the particles at higher sintering temperature (1400 ºC). This evidence proves the influence of increasing the sintering temperature on improving the sintering process.

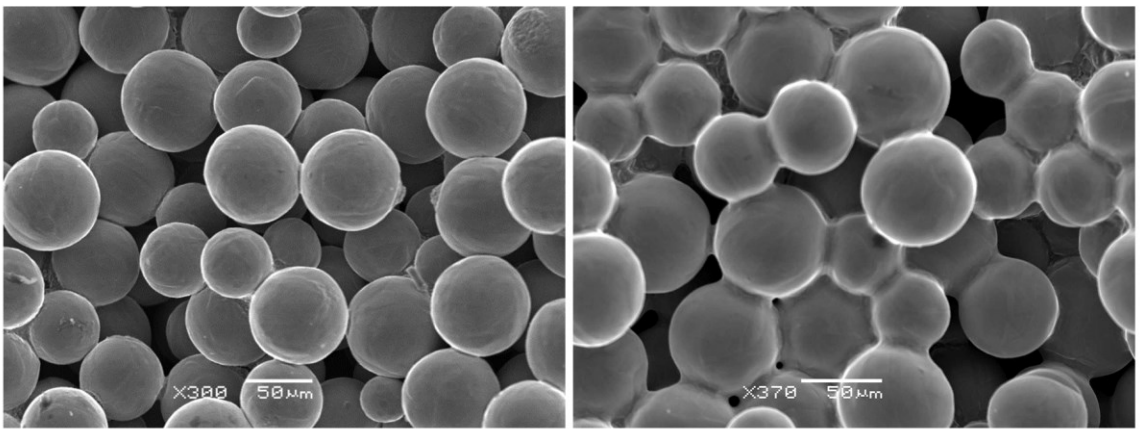

Figure 3-6 SEM of Ti samples fabricated from category F with fine particles bounded with 3% PVA and sintered for 1hr at (a) 1,100 ºC, (b) 1,400 ºC.

The chemical composition of Ti samples was evaluated by the EDX. The histogram of the EDX reveals that the structure was not contaminated by any material

during the sintering process and there was no residual of PVA or its by-products after sintering. The reading of the EDX was taken from the sinter neck as shown in Figure 3-7. The main material in the histogram is Ti.

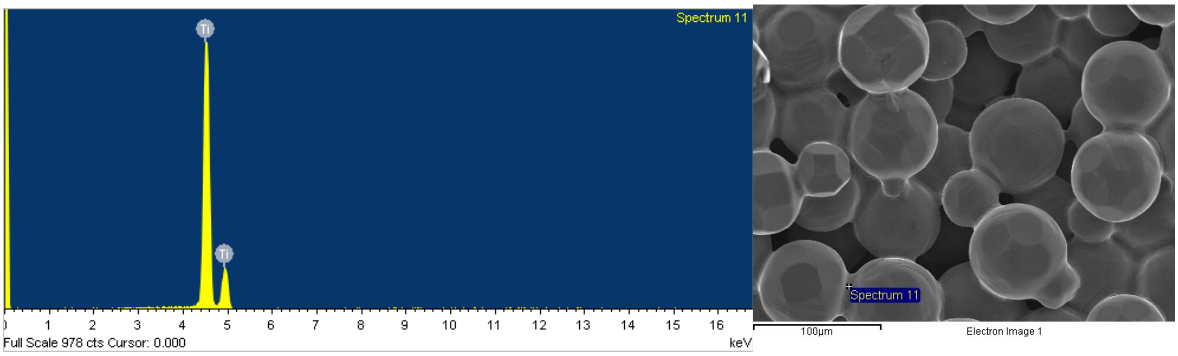

Figure 3-7 The EDX spectrum of Ti sample fabricated from category F, 3% PVA used as a binder and sintered for 1 h at 1400 ºC; the image at right presents the location on a sinter neck selected for EDX-characterization.

3.7.2 Shrinkage

The sintering shrinkages associated with the produced samples in horizontal and vertical directions are presented in Figure 3-8 and Figure 3-9, respectively. The results are presented separately for 3 and 5% of PVA. In general, the vertical shrinkage was higher than the horizontal shrinkage (2-5% in vertical vs. 1-4% in horizontal direction) and the parts shrank more in 5 % PVA compared to 3% PVA .

3.7.3 Porosity

Porosities of samples made with different powder sizes and PVA compositions at varying sintering protocols were measured as shown in Figure 3-10. For each point on this graph, four samples were made in which their corresponding standard deviations on porosity are also presented in the figures. These samples demonstrated varying porosity in the range of 31 to 43%.

3.7.4 Compressive Strength

The results of the compression test are depicted in Figure 3-11. In general, increase the sintering temperature and time cause an increase in the strength of the structure. Also,

decrease the size of Ti particles causes an increase in the compressive strength. In this study, compressive strength in the range of 56-509 MPa resulted from the four categories of powder which were sintered under different sintering conditions.

3.8 Discussion

Porous Ti structures were produced using a powder-based adhesive bonding AM process and the physical, chemical and mechanical properties of them were characterized. In addition, the effective process parameters were assessed. For design and manufacturing of orthopedic implants, the dimensional precision is a key factor. The implants should fit in the spaces which are precisely targeted for. This precision is highly affected by dimensional deviations occur during the manufacturing process. Structural shrinkage is a critical cause of dimensional deviation which happens during sintering process. A low percentage of shrinkage in the structure is preferred in order to obtain an effective control over the geometrical accuracy. Using the measured dimensional deviations from original CAD model to the final sintered part, an anisotropic compensation factor can be determined. The compensation factor is applied on the CAD model to obtain the final part with desired dimensions. However, anisotropic shrinkages cause nonuniform dimensional deviations. Anisotropic shrinkages are incredibly difficult to accurately compensate in the parts with complex surface due to the interactions between dimensional deviations in x, y, and z directions. Thus, process parameters which results in more uniform shrinkage are desired for AM of complex-shaped orthopedic devices.

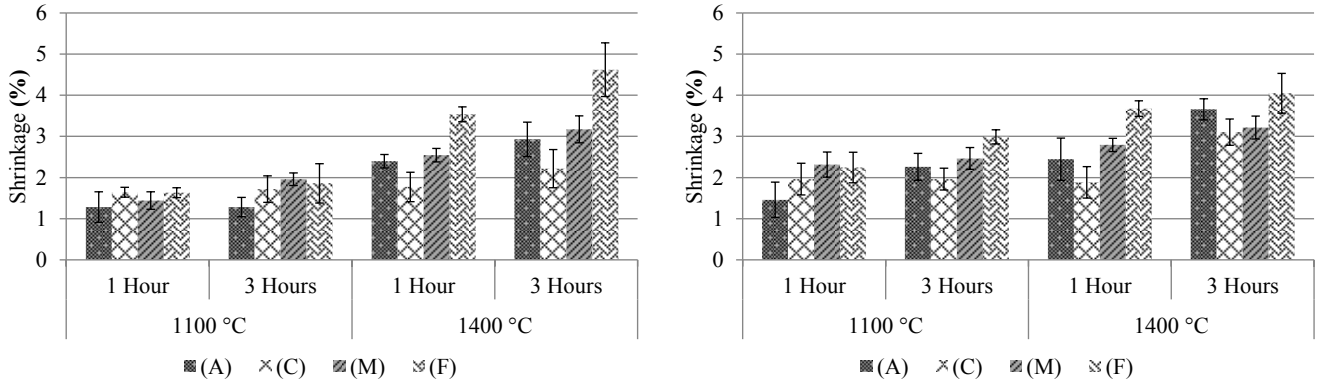

Figure 3-8 Horizontal shrinkage of Ti samples composed of (a) 3% PVA and (b) 5% PVA.

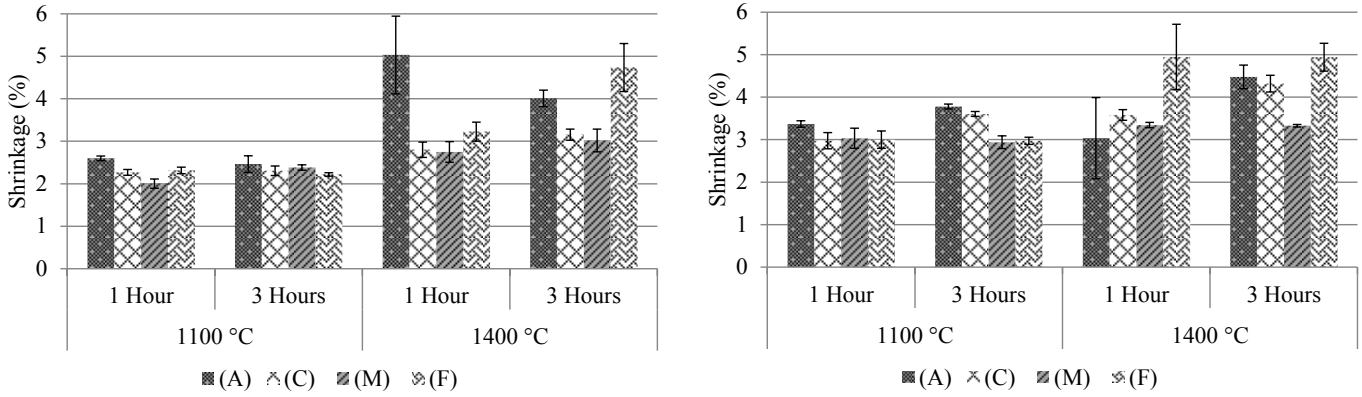

Figure 3-9 Vertical shrinkage of Ti samples composed of (a) 3% PVA and (b) 5% PVA.

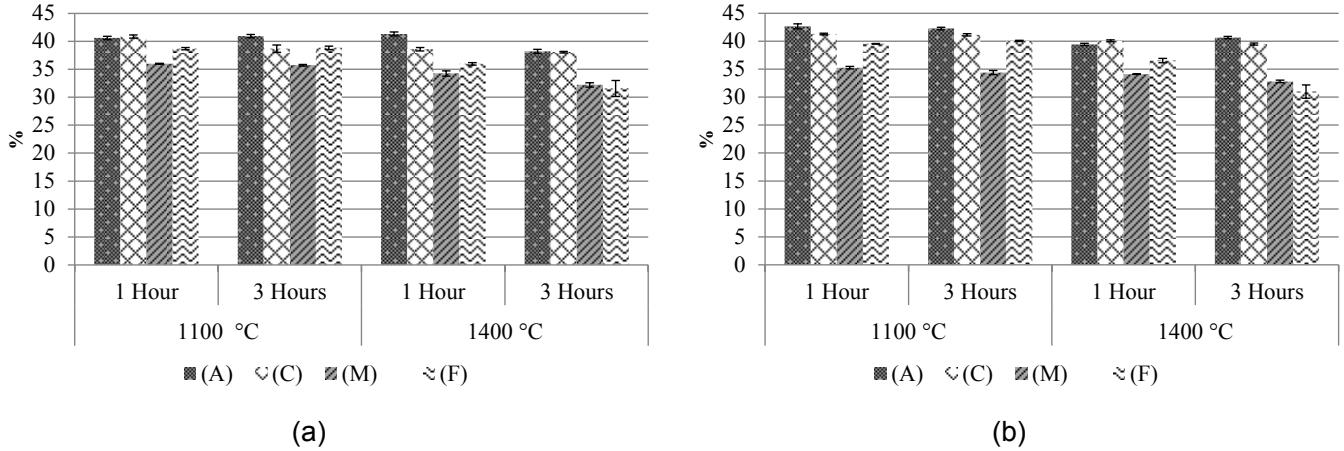

Figure 3-10 Porosity of the porous structures fabricated by varied sizes of Ti powder and sintered with different sintering conditions and composed of (a) 3% PVA (b) 5% PVA.

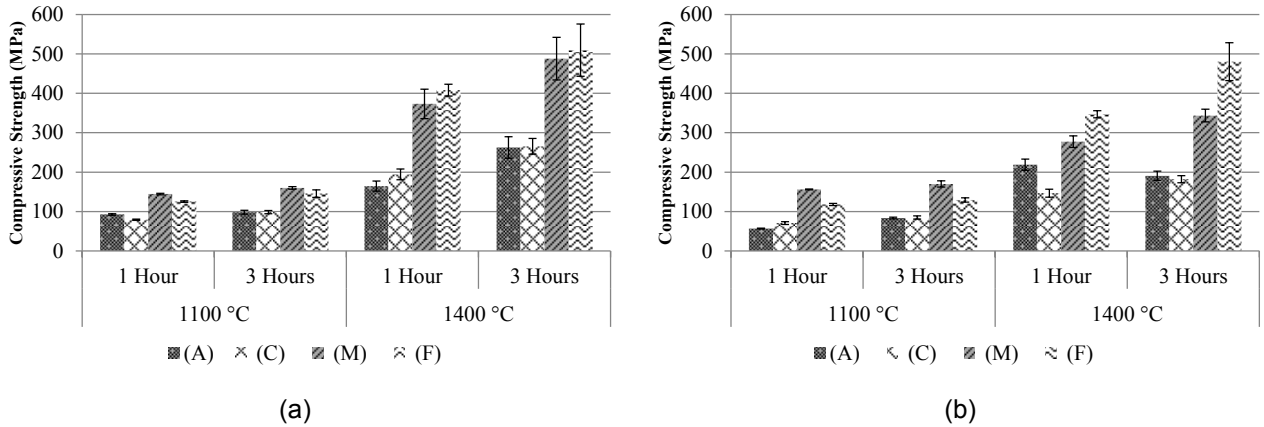

Figure 3-11 Compressive strength of the porous structures fabricated by varied sizes of Ti powder and sintered with different sintering conditions and composed of (a) 3% PVA (b) 5% PVA.

In this study, sintering shrinkages were in the range of 1.28% ± 0.37% to 4.6% ±1.3% in horizontal direction and 2% ± 0.11% to 5% ± 0.91% in vertical direction. The shrinkages observed in the present study obtained via a direct AM process (adhesive bonding 3D printing) is low compared to the shrinkages reported for other fabrication processes including direct[76] and indirect methods[52]. Ti samples fabricated using the electron beam melting (EBM) technique has shown horizontal and vertical shrinkage of 6.5% and 7.1%, respectively[76]. In the indirect 3DP technique (which include 3D printing of mold, casting the Ti powder followed by sintering at 1300 ºC), the horizontal and vertical shrinkages were reported equal to 11.9% ± 1.1% and 9.2% ± 0.6%, respectively[52]. Also, the difference between horizontal and vertical shrinkages in the present study (which is mainly due to gravity effect during sintering) is relatively small (~1%). It should be noted that the above comparison on the shrinkage level of the manufacturing techniques, assuming that optimum results are reported in these articles.

It is also noteworthy that the sintering shrinkage has a relation with the sinter-neck size. To investigate this matter the neck sizes were measured using the SEM images of the microstructures. Figure 3-12 presents the variation of sinter-neck-size to particle-diameter ratio (x/a) for the category F (<75 µm). The trend resembles the trend of sintering shrinkage as shown in Figure 3-8 and Figure 3-9. Sinter neck size has a profound impact on the mechanical strength of structures that will be discussed later.

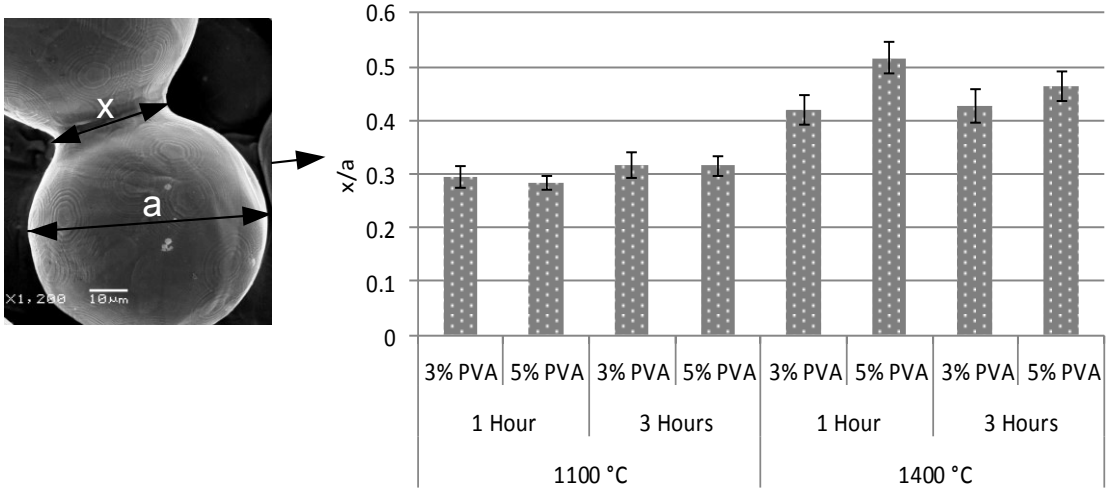

Figure 3-12 Variation of sinter-neck-size to particle-diameter ratio (x/a) for the category F(<75µm).

Other than geometrical dimensions, porosity (i.e., void volume%) of the structures is profoundly affected by the sintering shrinkage. In general, a higher sintering temperature resulted in a higher shrinkage and, in turn, a lower porosity as seen in Figure 3-10. As seen in the SEM image of the microstructures (Figure 3-6), sinter necks has started to form at 1100 °C and well-developed at 1400 °C. Sintering time (3 h vs. 1 h) did not significantly affect the porosity. Only in case of using fine powder (category F), the porosity decreased ~6% more in 3 h sintering. The effect of mixing more PVA with Ti (5% vs. 3%) was observed on the compressive strength of all categories of powder which are sintered at 1400ºC (50-150 MPa). The increase in the amount of PVA caused a decrease in compressive strength especially in categories A, C and M, but in category F the reduction in the strength is not significant. This might be due to the fact that the driving force of sintering is higher for fine particles that compensate the reduction caused by increase of PVA. As shown in Figure 3-8 and Figure 3-9, it is obvious that using finer Ti particles resulted in higher shrinkage and ended up with lower porosity that can be due to higher driving force for atomic diffusion in high temperature[50]. Some may argue that the drop in porosity have been caused by the variation between the compact density of green sample. However, Figure 3-13 shows that category F has the highest drop in the porosity compared to the other categories. About 11% drop in porosity was observed for the samples from category F, while 6% in category A sintered at 1400 ºC for 3 h using 5% PVA. The increase in compact density plays a role in decreasing the porosity, but the powder particles size is the crucial factor in this reduction. It is noteworthy that category M is composed of narrower range of powder particle size (75-106 um) and it presents lowest porosity in all sintering conditions except at 1400 ºC and 3 h.

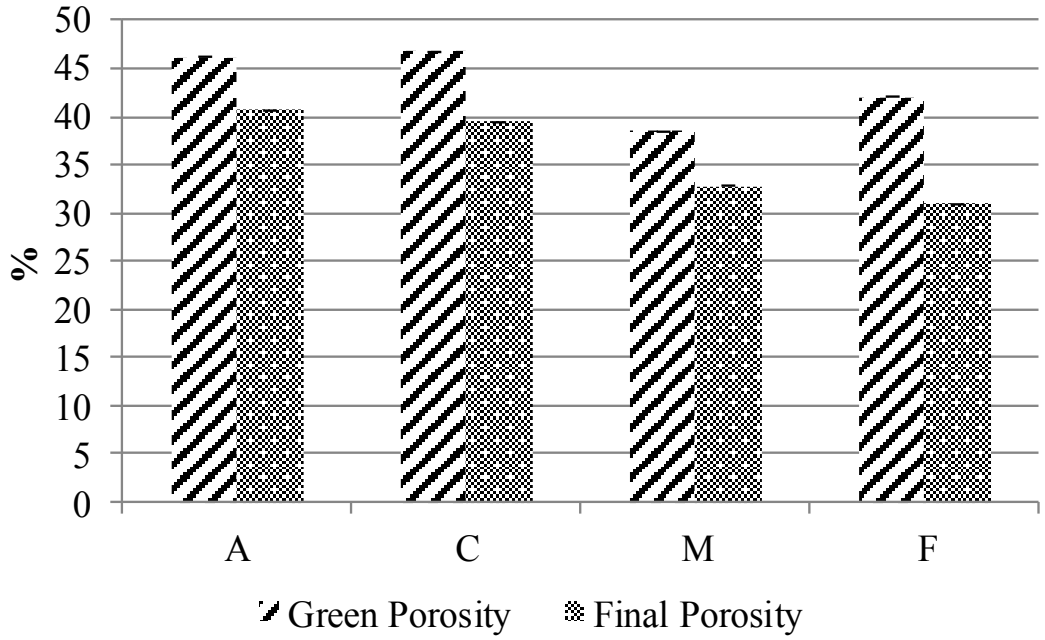

Figure 3-13 A comparison between the porosity of green samples and sintered samples which sintered at 1400 ºC for 3 hours using 5% PVA.

The trend/variation of mechanical strengths of produced samples (Figure 3-11) is almost in an agreement with the variation of associated porosity (Figure 3-10). The samples with lower porosity (that were processed in higher temperature, i.e., 1400 °C) showed higher compressive strength. For instance, the parts made from M and F powders at 1400 °C were about five times stronger than those made at 1100°C (~500 MPa vs. 100 MPa). The effect of increase in sintering time and PVA% on mechanical strength was not significant in samples which were sintered at 1100°C.

In summary, the variation of porosity and compressive strength of samples can be classified into two trends: (1) the samples made from powder categories which have small particles sizes (<100µm, i.e., categories M and F) show lower porosity and higher strength, and (2) the samples consist of larger particles (i.e., categories C and A) have higher porosity and lower strength. As explained previously, this matter may attributed to dissimilarity in sintering driving force for fine and coarse particles. It is obvious that the samples with lower porosity and larger sinter necks have higher mechanical strength

considering the fact that the fracture occurs on the sinter necks as was determined using the SEM images of fracture surface (Figure 3-14).

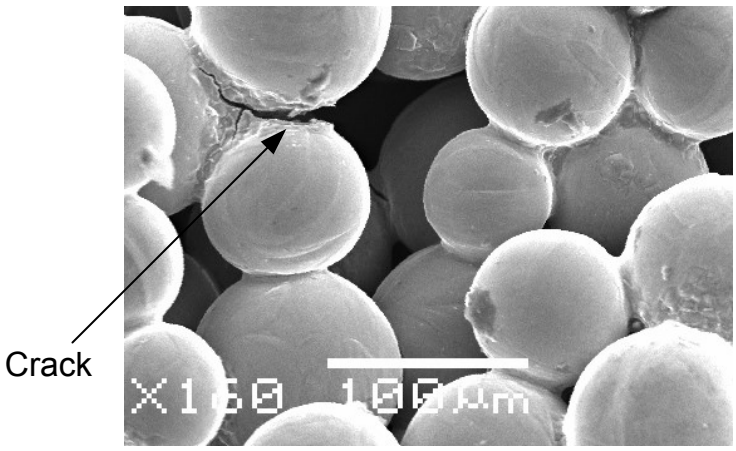

Figure 3-14 SEM images showing the crack initiated at the sinter neck of sample.

In the present study, a wide range of compressive strength was achieved from 56 to 509 MPa. The results give the superiority to the present technique when compare it with other AM techniques i.e., SLS used for the same purpose and the strength were in the range of 0.5-350MPa[40], indirect printing using a wax mould produced samples had strength in the range of 150-350 MPa[52] and EBM which produced a sample with strength of 116 MPa[76].

3.9 Relation between Porosity and Compressive Strength

The model of Gibson and Ashby[77] can predict the compressive strength of porous metals which have a homogenous porous structure[78]. In this model, the relative density ρ/ρ_s (Relative density = 1- Porosity) is the most important parameter in governing the compressive strength of the open-cell porous structure as follows:

$$\frac{\sigma}{\sigma_s} = C\left(\frac{\rho}{\rho_s}\right)^{\frac{3}{2}} \qquad (7)$$

where σ and σ_s denote the strength of the porous and bulk Ti, respectively; ρ and ρ_s are the density of the porous and bulk Ti, respectively; C is the proportionality constant.

In attempts to apply the model of Gibson and Ashby on the Ti porous structures in Wen et al.[79] and Zou et al.[80], they concluded the incompatibility of this model with porous Ti structure since the difference between the experimental results and the theoretical model is large. In the present study, another trial is carried out to fit the experimental results to the model using a compressive strength σ_s = 760 MPa[78]. The proportionality constant C and the exponent factor were modified through regression analysis and curve fitting of the experimental data as listed in Table 3-2.

Table 3-2 Gibson and Ashby Modified Models.

Sintering Temperature (°C)	Relative Compressive Strength
1100	$\frac{\sigma}{\sigma_s} = 3.04\left(\frac{\rho}{\rho_s}\right)^{6.14}$
1400	$\frac{\sigma}{\sigma_s} = 5.81\left(\frac{\rho}{\rho_s}\right)^{6.18}$

In Figure 3-15, two trend lines represent the plotted data of samples sintered at 1100°C (the lower trend line) and 1400°C (the upper trend line). The influence of the sinter neck in increasing the proportionality constant appears in Figure 3-15. When Ti samples were sintered at 1100°C where the sinter necks between the particles were just initiated, the plotted points in the figure are converged from the model line. These points represent all four categories of powder which were sintered at the same temperature. However, a different scenario occurred when the samples were sintered at 1400 °C, since the plotted data remained close to the model line at Categories A and C, which have large particles. After that, the plotted data of Categories M and F diverged away from the model line. This divergence caused an increase in the proportionality constant in the model when the samples sintered at 1400 °C, with the knowledge that a thick sinter neck was formed in the samples of these categories. The difference in the value of the exponent factor between the model of Gibson and Ashby and that in the present study may be due to the geometrical characteristic of the cell wall. It should be noted that the description of Eq.(7) by Gibson and Ashby is based on the structure of the unit cell as a simple cubic array with a square cross-sectional member. However, in the present study

the simple structure of the unit cell is formed by four spherical particles connected to each other by the sinter necks. These necks are in the shape of disc with a circular cross-section.

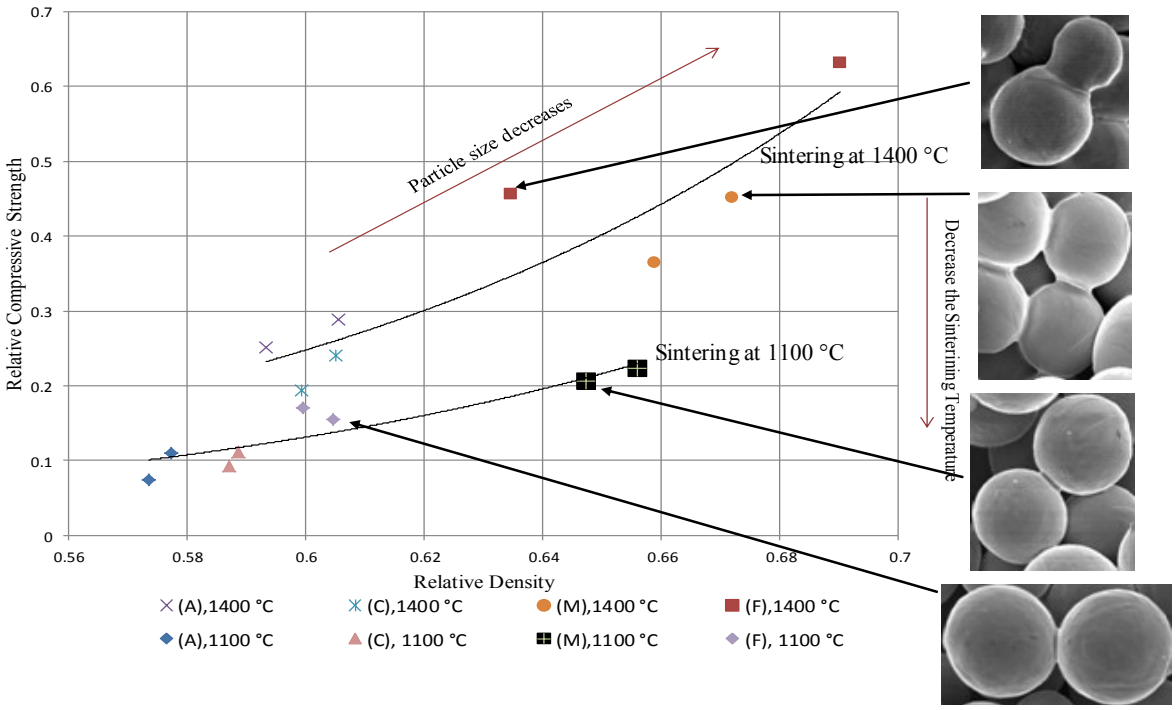

Figure 3-15 Relative density of several powder categories for two sintering protocols as a function of relative compressive strength.

To locate the results of the present study and compare those with the real bone, a data regarding the cancellous bone mechanical properties was adapted from Gibson and Ashby[81] and depicted in Figure 3-16. According to Gibson and Ashby[81], the data of the cancellous bone concentrated around the line defined by Eq. (7) as shown in Figure 3-16. The results of the present study were also plotted in this figure. As seen in Figure 3-16, the categories of Ti which sintered at 1100°C fall in the range of the cancellous bone. However, the powder categories sintered at 1400°C that possessed a percentage of porosity approaching the porosity of the cortical bone fall out of the range of the cancellous bone.

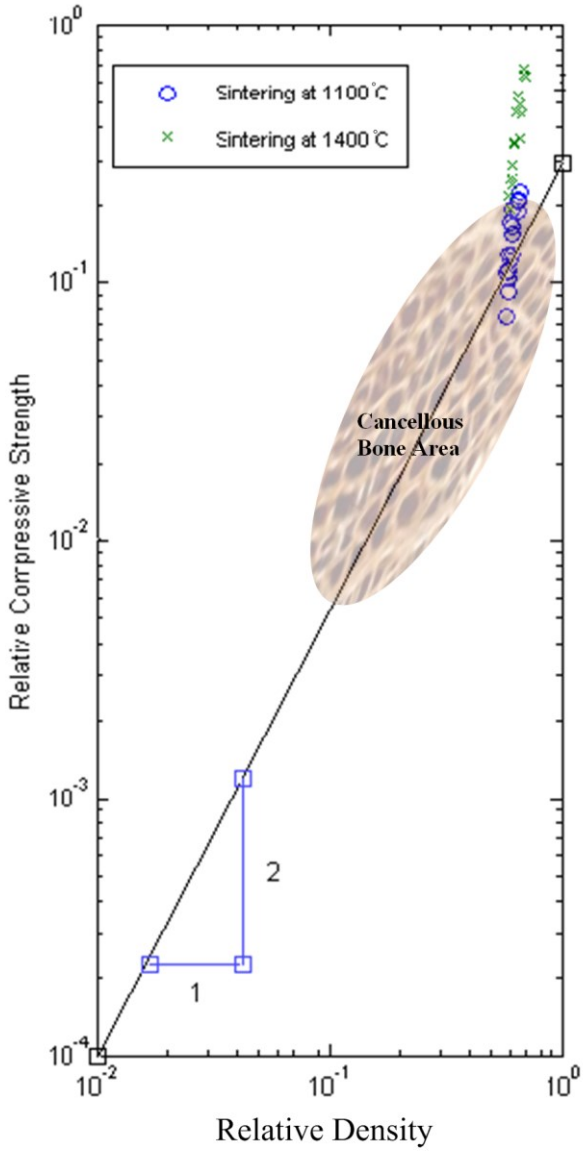

Figure 3-16 Relative density of Ti structure as a function of the relative compressive strength.

According to the obtained results, the mechanical properties are not solely controlled by the relative density, but also the sinter neck plays a major role in strengthening the structure. For instance, the results showed two cases of Ti samples produced with different sizes of powder and sintered at different heating protocols, where both samples have identical porosity of ~36%, but different compressive strengths of 144 and 408 MPa, respectively. This contrast may provide evidence of the effectiveness of sinter neck in controlling the strength of structure. It should be emphasized that this

diversity in the structure properties is beneficial, because mechanical properties of the porous structure can be tailored by selecting the porosity to match those of various bone types.

3.10 Conclusion

In this study, several parameters were varied in the additive manufacturing of the porous Ti structures including sintering temperature, sintering time, amount of PVA and size of Ti powder. The results of the experimental studies have proved the possibility of controlling the porosity and mechanical properties of Ti implant using proper parameters in the direct additive manufacturing done by the 3DP machine. It was found that the primary crucial factor in controlling the mechanical properties of the structure is the sinter neck size. It was observed that the sinter neck was only initiated at 1100°C and the effective sintering began after three hours at 1400°C. The porosity in the produced samples fell in between 31 and 43%. This percentage of porosity is similar to the porosity of the cancellous bone (30 - 90%)[82]. Also, the minimum porosity was produced is 31% which approaches the porosity of the cortical bone (5-30%)[82]. The compressive strength of Ti samples affected by the amount of PVA when sintered at 1400 ºC and were distributed over a wide range between 56 to 509 MPa. One of the most beneficial advantages of this technique is the low level of shrinkage, which was shown to be 1.5-5%.

Chapter 4 On the influence of sintering protocols and layer thickness on the physical and mechanical properties of additive manufactured titanium porous structures

4.1 Introduction

Aseptic loosening is the main cause of revision surgery for total joint replacement [4]. Various factors cause the loosening, and the main mechanical factor is the stress-shielding effect [5]. Stress shielding is due to a mismatch in the stiffness of cementless implant and cortical bone, which in turn leads to bone resorption[83,84]. The structure of the cortical bone is very dense with a porosity ranging between 3-30% [22,82] with varying levels of mechanical properties. This variation is influenced by several factors including bone location, bone age, mineralization, and hydration[85]. As such, the design and fabrication of a bone implant is a sophisticated process due to the anisotropic properties of bone [44].

Ti has been used for many decades due to its biocompatibility, and given the fact that the biocompatibility of the metal mainly depends on the corrosion resistance. Ti provides a higher corrosion resistance compared to other metals due to the protective oxide layer that forms on its surface [34,86]. The best candidate to further minimize stress shielding effects while retaining other beneficial characteristics is Ti foam structure, due to its comparable stiffness with bone and excellent strength to weight ratio[45,46].

Many attempts have been made to mimic cortical bone properties by employing titanium foam. Oh et al.[50] fabricated porous Ti foam by cold pressing before sintering and

obtained porosity in a range from 5 to 37%. In that study, three independent variables, particle size, sintering temperature, and powder compaction level were altered to control the porosity and mechanical properties of the metal foam. The results indicated a decrease in porosity associated with a linear increase in Young's modulus. This porosity was highly affected by varying the powder particle size and level of powder compaction when the same sintering temperature was used. However, changing the sintering temperature did not cause a noticeable variation in the porosity. It was concluded that the crucial factors affecting porosity were initial powder size and the level of powder compaction. Additionally, the best porous Ti structure for the associated cortical bone properties should have a porosity between 32 and 36% [50]. Another study conducted by Guden et al. [87] using a Ti alloy powder (i.e., Ti6Al4V) (spherical and irregular shaped particles) had a similar aim. That study concluded that an increase in the powder compaction of the green samples caused a reduction in the porosity of the structure after sintering, and compressive strength was primarily affected by the porosity of the structure. It was also shown that using a spherical-shaped powder led to higher-strength structures when compared to the strength achieved using irregularly-shaped powder particles. Strength and elastic modulus similar to cortical bone properties were also achieved.

The same concept of varying the compaction level of the green structure can be achieved using powder-bed based additive manufacturing techniques. This approach could be similarly implemented by altering the layer thickness of the 3D printing process. In this regard, Farzadi et al. [88] addressed the effect of varying layer thickness, at 85, 100, 112.5, and 125 μm on the compressive strength, Young's modulus, toughness, and integrity of the structure using calcium sulfate powders. The authors reported that using a 112.5 μm layer thickness demonstrated the highest strength and toughness. This improvement in strength and toughness was attributed to a reduction in the shear force, resulting from a smooth sprinkling of powder by the counter-rotating roller at the powder spreading stage. However, a thinner layer thickness (i.e., 85 μm) led to improved structural integrity. In contrast, Vaezi and Chua [89] found that surface integrity and flexural strength decreased when a thinner layer thickness was used in their investigation of the influence of varying printing layer thicknesses on the strength and printing quality using a plaster-based

powder. However, the tensile strength increased when a thinner layer thickness was used. In the both preceding studies, the materials were not metal, so they did not require post-processing sintering to form the rigid structure.

The influence of various sintering temperatures and binder contents along with the de-binding heating protocol on the physical appearance and shrinkage of a porous Ti structure were studied by Wiria et al. [6]. In that study, two de-binding protocols were followed, and the lower temperature protocol (250 and 415º C) showed lower shrinkage. However, increasing the sintering temperature led to a higher level of shrinkage. According to our previous work and the work of Zou et al. [66,90], sintering temperature has a highly significant impact on the development of the sinter neck, which directly influences the strength of the structure.

There is a lack of contributions in regard to directly using a powder bed ink-jet based additive manufacturing machine to fabricate Ti porous structures. The reason behind this lack comes from the difficulties of dealing with Ti, since it requires a sophisticated sintering condition in post processing and the machine since invented has been mainly designed to fabricate ceramics and polymeric materials.

In this study, the effect of layer thickness which represents the level of compaction of the powder during the 3D printing process will be addressed. In addition, the sintering temperature variations, which represent diffusional bonding among the particles on the printed Ti structure will be investigated and will form the scope of this study. Furthermore, the interaction between both parameters, the level of powder compaction and sintering temperatures, and their influence on the structure's physical and mechanical properties will be investigated. As there is no clear understanding in the literature on the correlation of the sinter neck size between the particles in the additively manufactured structure and the porosity of the structure, an analytical model will be developed in an attempt to clarify the relationship between these factors based on the volume fraction of the compacted powder.

4.2 Methodology

4.2.1 Material

Ti powder with particle size range of 38-45 μm was used in this study to produce the samples. The received powder of CP Ti (CP Ti Grade 1, Advanced Powders and Coatings, Inc., Boisbriand, QC, Canada) was less than 45 μm and a sieve (US standard test sieve, No.400, Cole-Parmer, USA) with a mesh size of 38 μm was used to sift the powder and obtain particles size between 38-45 μm. The metal powder was mixed with the binding agent which was used to bind the Ti particles during the printing stage of the green part. This agent is Polyvinyl alcohol (PVA) powder ,86–89% hydrolyzed, with a low molecular weight (Alfa Aesar, Ward Hill, MA, USA) and the mixing recipe was 3 wt% of PVA mixed with Ti powder. The mixture was milled for four hours in a jar-mill (LABMILL 8000 JAR MILL MACHINE, Paul N. Gardner Company, USA).

4.2.2 Manufacturing

The printing of the samples was carried out by using an ink-jet powder-based 3D printer (ZPrinter310-Plus, 3D Systems, Rock Hill, SC, USA) in which the powder mixture (Ti and PVA) was loaded in the machine. The printing process was implemented by printing the samples layer over layer with the assistance of an aqueous-based binder ($Zb^{TM}60$, 3D Systems, Rock Hill, SC, USA), which was loaded in the print-head of the machine and used to bind the Ti particles with the assistance of the PVA. In the factorial design of this experiment, layer thickness and sintering temperature were chosen as parameters for the variables in this study. There is a limitation in regard to varying the layer thicknesses using the ZPrinter310-Plus. However, we've accessed and modified the machine code so that the printer became capable of printing any layer thickness without limitation. Therefore, different layer thicknesses were used for printing to represent different levels of powder compaction (Table 4-1) and four samples of each layer thickness were printed accordingly.

Table 4-1 Layer thicknesses used for printing and corresponding number of printed layers and average green density for each sample.

Layer thickness (µm)	62.5	87.5	105	125	150	175
Actual No. of layers	177	127	106	89	73	63
Green density (g/cc)	2.53	2.51	2.47	2.42	2.40	2.37

4.2.3 Sintering

Sintering temperatures were selected as: 800 ºC, 1000 ºC, 1200 ºC, and 1400 ºC. Before the sintering process was launched, a PVA de-binding process was conducted over two stages at 295 ºC and 500 ºC (Figure 4-1).

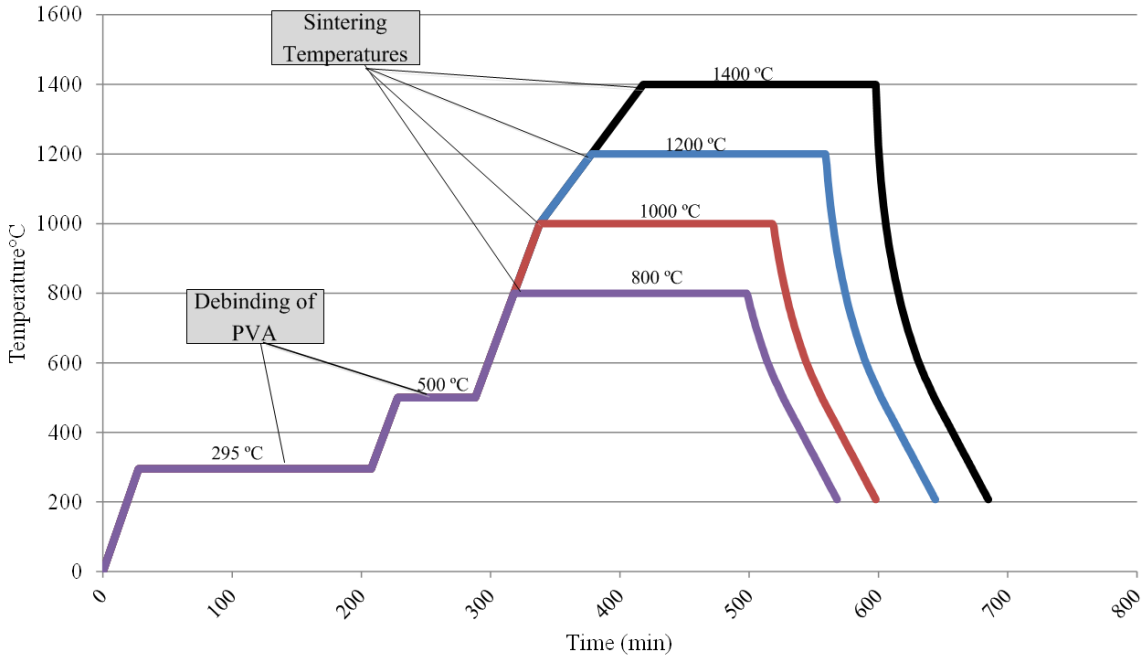

Figure 4-1 Four different heating profiles followed during the sintering process.

4.3 Characterization

4.3.1 Porosity

Porosity measurement was conducted using the Archimedes principal of buoyancy and according to ASTM B 311-08 and ASTM C373-88 [91,92]. This measurement was obtained with the assistance of a Universal Specific Gravity Kit (Sartorius®, Bradford, MA, USA) and an electronic balance (APX-203, Denver Instruments, NY, USA) with a precision of 0.001 g. The steps for measuring the porosity were similar to those followed by Basalah et al. [66].

4.3.2 Compression Test

A compression test was used to obtain the stress-strain curve for each sample. The curves were then used to obtain Young's modulus (E) and 0.2% offset yield strength (σ). The 0.2% yield strength was obtained according to ASTM Standard E9-09 [93]. The compression test was conducted using a uniaxial compression test machine (Instron-4206, USA) with a cross head speed of 1 mm/min. The dimensions of the rounded bar samples (n = 4) were Ø7.49 mm × 11.24 mm.

4.3.3 Shrinkage

Shrinkage measurements were conducted using an electronic Vernier caliper (Mitutoyo Corp., Kawasaki, Japan) with a precision of 0.01 mm. The vertical and horizontal dimensions of the samples were collected before and after the sintering process and the compact dimensional change was divided by the initial dimension to obtain the rate of shrinkage as reported by Basalah et al. [66].

4.3.4 Microscopic Characterization

In this study, the sinter neck between the particles was quantified using the image processing toolbox 8.3 (MATLAB R2013b, USA). The characterization was conducted on an image shot by a scanning electron microscope (SEM) (JEOL JSM-6460). The diameters of the necks between the particles and the diameters of the particles were measured using the roller option from the image processing toolbox and compared to the

image scale. Next, the measured pixels were interpolated and converted to a real value based on the image scale to obtain the real sinter neck diameter and particle diameters. Finally, the sinter neck ration was calculated by dividing the sinter neck diameter over the particle diameter.

4.3.5 Statistical Analysis

Two-way ANOVA test (a multifactorial statistical test) was conducted on the results for porosity, yield strength, Young's modulus, and vertical and horizontal shrinkages to detect any significance among the results of each property. This test was used to investigate the influence of two factors - compaction of powder (layer thickness) and sintering temperature - on the above properties. Also, this test was able to detect whether the interaction of both factors was influencing any property.

4.4 Results

4.4.1 Microscopic characterization

Figure 4-2 shows the SEM images which are used to characterize the microstructural arrangements of particles. The sinter neck measurements obtained from these images by dividing the sinter neck dimension (X) over the particle diameter (D).

4.4.2 Porosity

The porosity of the structure is significantly influenced by increasing the sintering temperature ($p<0.05$) as shown in Figure 4-3. Furthermore, the decrease in the layer thickness causes a significant reduction in the porosity at the highest sintering temperature (1400 ºC) and relative reduction in porosity at other sintering temperatures. Moreover, the interaction of the sintering temperature and the compaction of the powder decrease the porosity of the structure significantly ($p<0.05$). In the current study, the porosity levels in the produced samples are in the range of 17-44%.

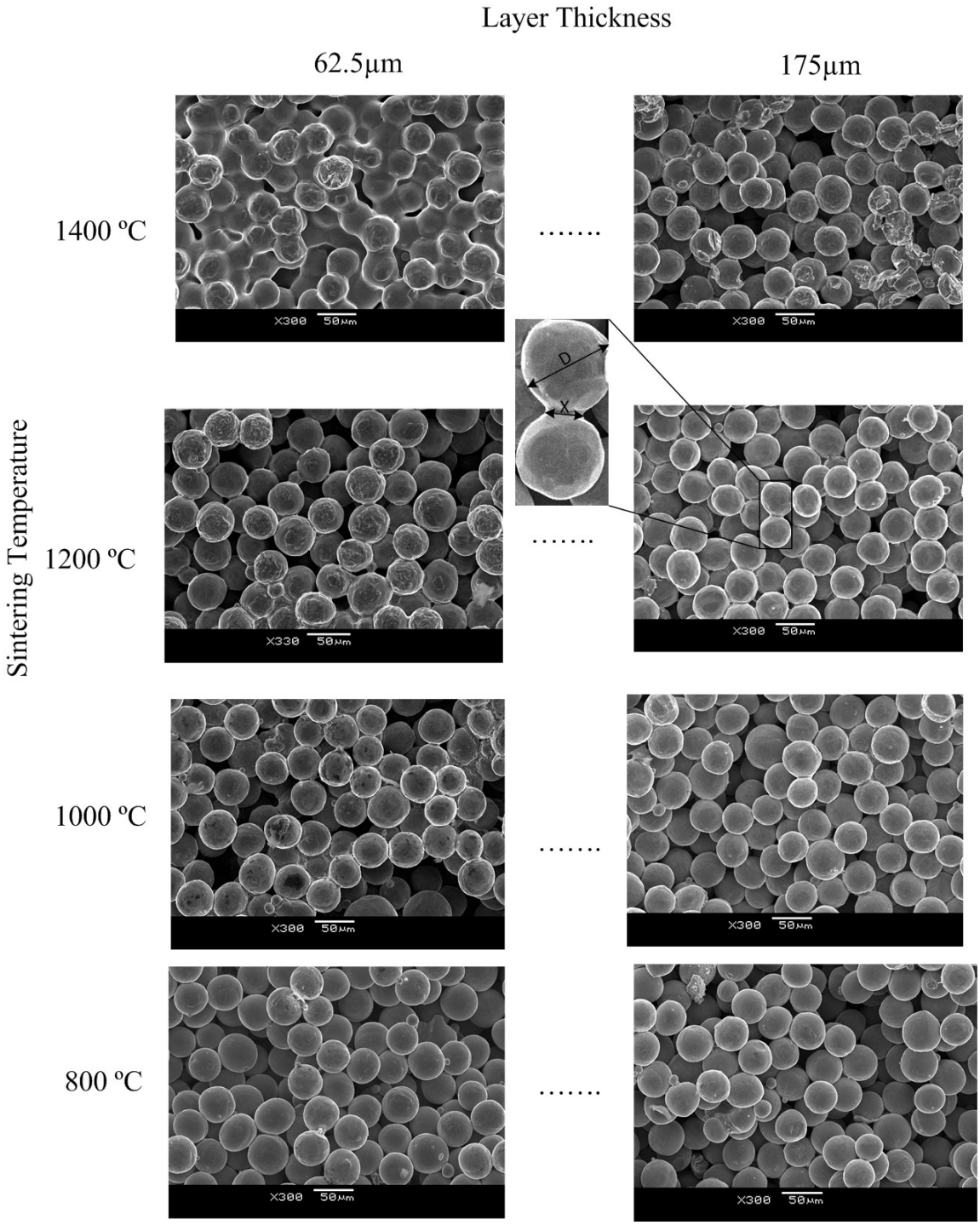

Figure 4-2 SEM images of various samples sintered at different sintering temperature and printed using two layers thickness, i.e. 62.5 and 175 represent the extreme edges of powder compaction.

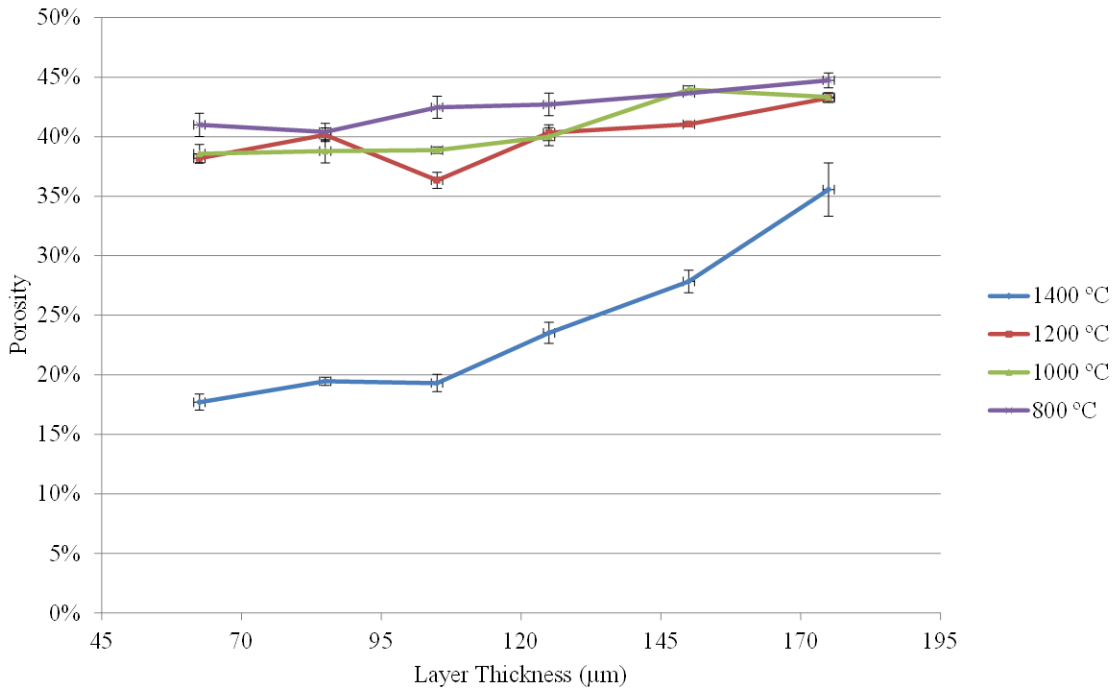

Figure 4-3 Influence of two independent variables - layer thickness and sintering temperature - on the porosity of the structure.

4.4.3 Young's Modulus

In general, increasing the sintering temperature and/or increasing the compaction of powder lead to an increase in the Young's modulus, as depicted in Figure 4-4. The statistical analysis using two-way ANOVA clarified that the interaction of both factors (sintering temperature and powder compaction) is significantly influential in increasing Young's modulus of the structure ($p<0.05$). In addition, the results show that each factor individually influences Young's modulus significantly ($p<0.05$). The samples observed a Young's modulus ranging between 0.77-11.46 GPa.

4.4.4 Yield Strength

The average yield strength of the samples increased significantly ($p<0.05$) when the sintering temperature is increased, as depicted in Figure 4-5. Increasing the compaction of powder has a significant influence on the yield strength of the structure at sintering conditions of 1000, 1200, and 1400 ° C; however, a sintering temperature of 800 ºC,

which is below the phase transformation temperature of Ti (882 ° C)[94] , was not significant. The interaction between the sintering temperature and the compaction of powder also increases the yield strength of the samples significantly ($p<0.05$), especially at higher sintering temperatures (1000, 1200, and 1400 ºC). The observed results of the yield strength ranged between 27-383 MPa.

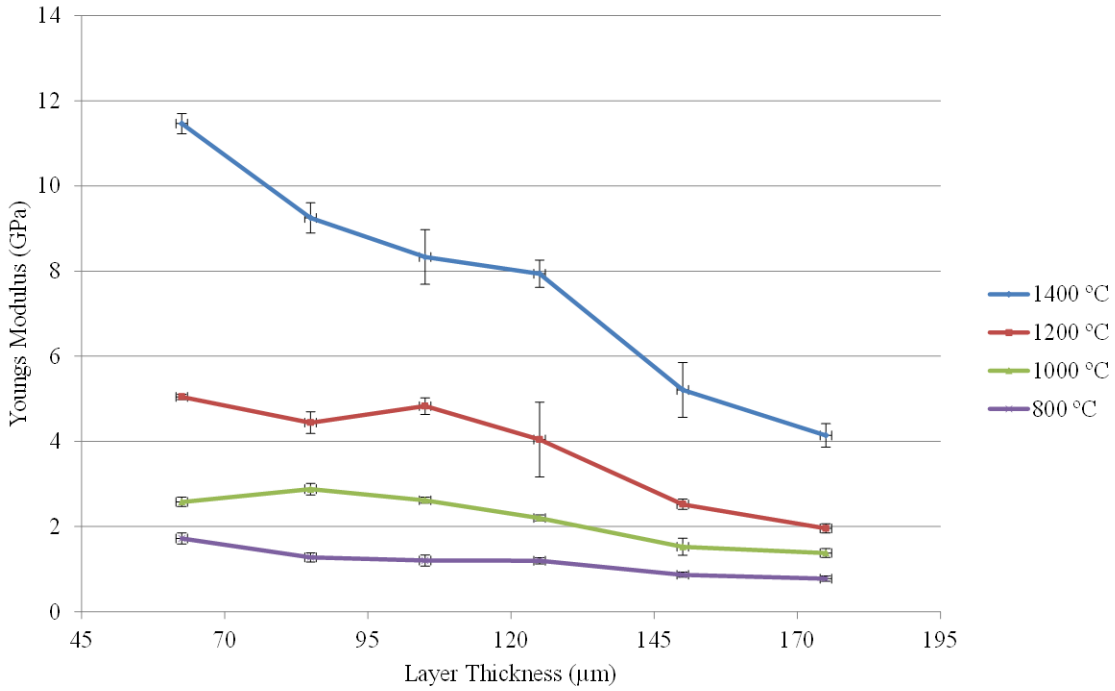

Figure 4-4 Variation in Young's modulus due to variations in layer thickness and sintering temperature.

4.4.5 Shrinkage

Figure 4-6 and Figure 4-7 show the dimensional variations in the samples following the sintering process. It is obvious that increasing the sintering temperature lead to significant shrinkage in both directions ($p<0.05$), particularly at the highest sintering temperature (1400 ºC). Similarly, increasing the powder compaction lead to an increase in shrinkage ($p<0.05$). In addition, the interaction between the sintering temperature and the compaction of powder significantly increases the shrinkage in both directions ($p<0.05$) according to a two-way ANOVA statistical test.

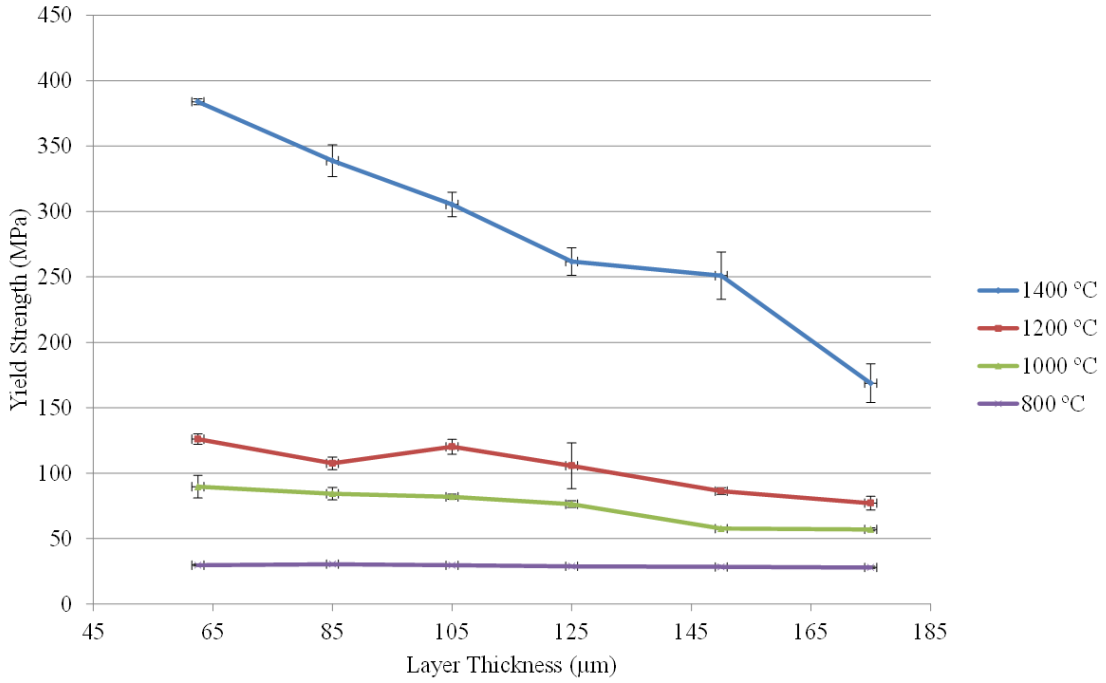

Figure 4-5 Variation in yield strength due to variations in layer thickness and sintering temperature.

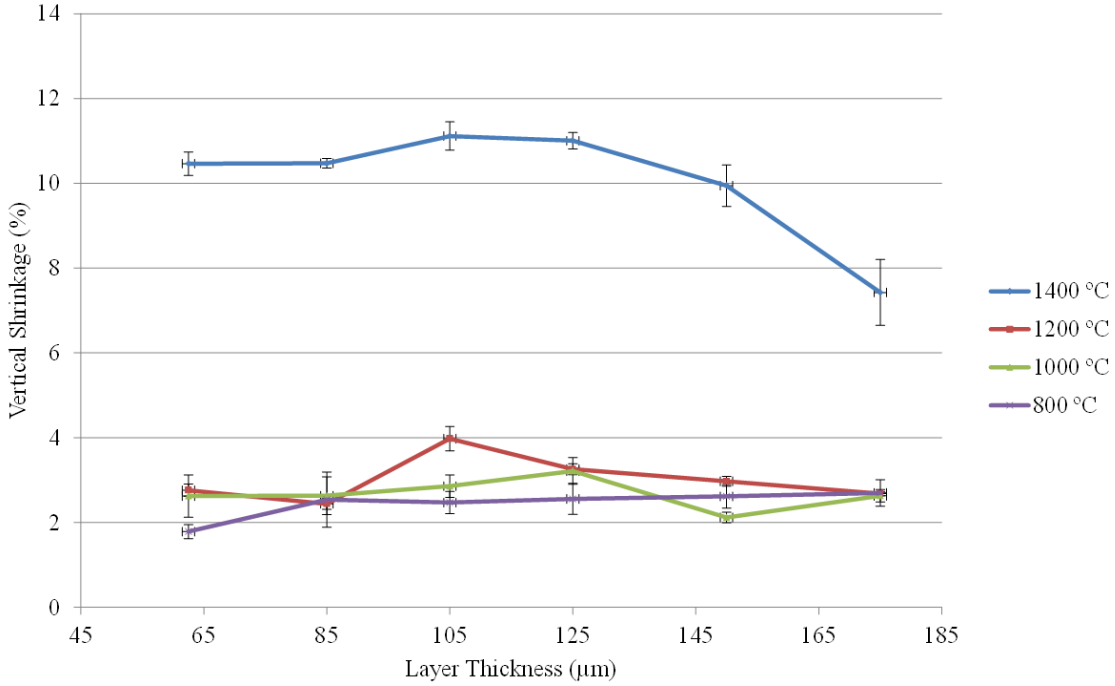

Figure 4-6 Vertical shrinkage variation as a function of sintering temperature and printing layer thickness.

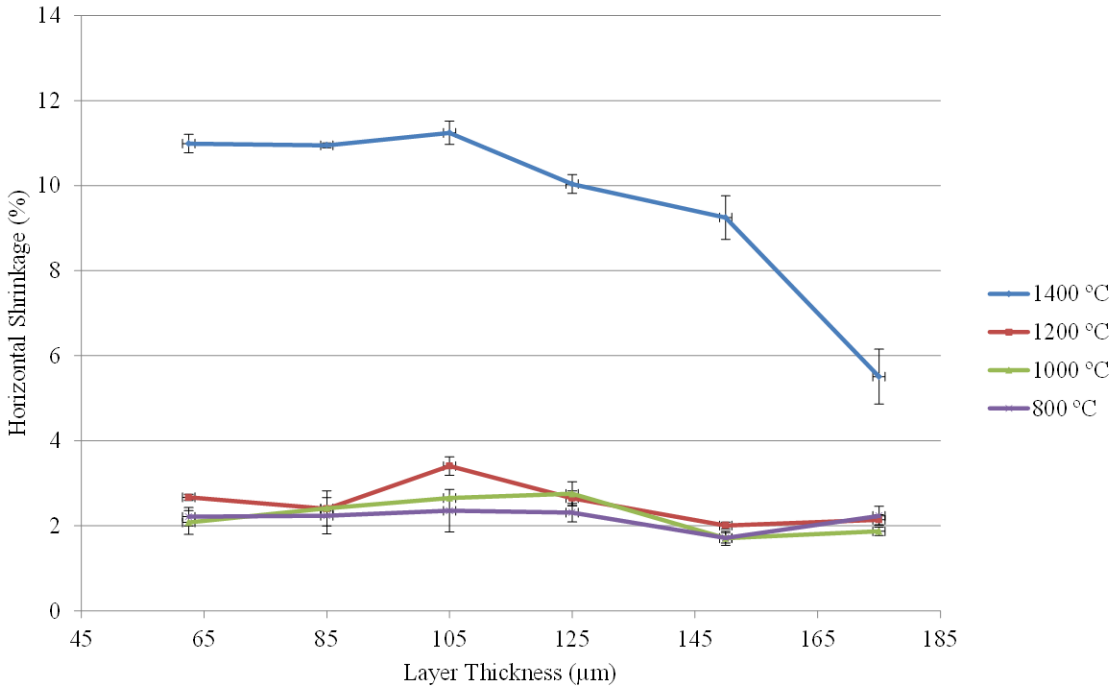

Figure 4-7 Horizontal shrinkage variation as a function of sintering temperature and printing layer thickness.

4.5 Analytical Model of the Microstructural Arrangement of Ti Particles

The aim of this section is to derive a formula that relates the sinter neck between the particles to the volume fraction (Porosity) of the simplest unit cell. The accumulations of these unit cells form the entire porous structure. In the model of Gibson and Ashby[77], the simplest level of the foam structure was assumed to be a cubic array with square cross sections. However, in the present study, the assumption for the unit cell geometry was evolved based on the microstructural observation, where four spherical particles of the powder (Figure 4-8) form the simplest cubic unit cell, and the wall of the unit cell are the sinter neck between the particles as shown in Figure 4-9. Knowing the volume fraction or the porosity in the unit cell could be reflected to the larger scale or the entire structure's porosity.

In this study, the simplest cubic unit cell includes eight particles and each contributed by one-eighth of its volume (Figure 4-9). In this model, the volume of this portion (Figure 4-9b) of the particle is calculated and the total volume of the eight portions is used to obtain the volume fraction of the unit cell. First, a geometrical analysis for the spherical particle is conducted, where the particle radius is (r) as shown in Figure 4-8. The

dimension from the center of the particle to cutting plane of the sinter neck segment is (r-h), and the dimension of the edge of the unit cell (d) is as shown in Figure 4-9:

$$d = 2 \times (r - h) \quad (1)$$

Thus, the bulk volume of the unit cell (V_b):

$$V_b = (2 \times (r - h))^3 \quad (2)$$

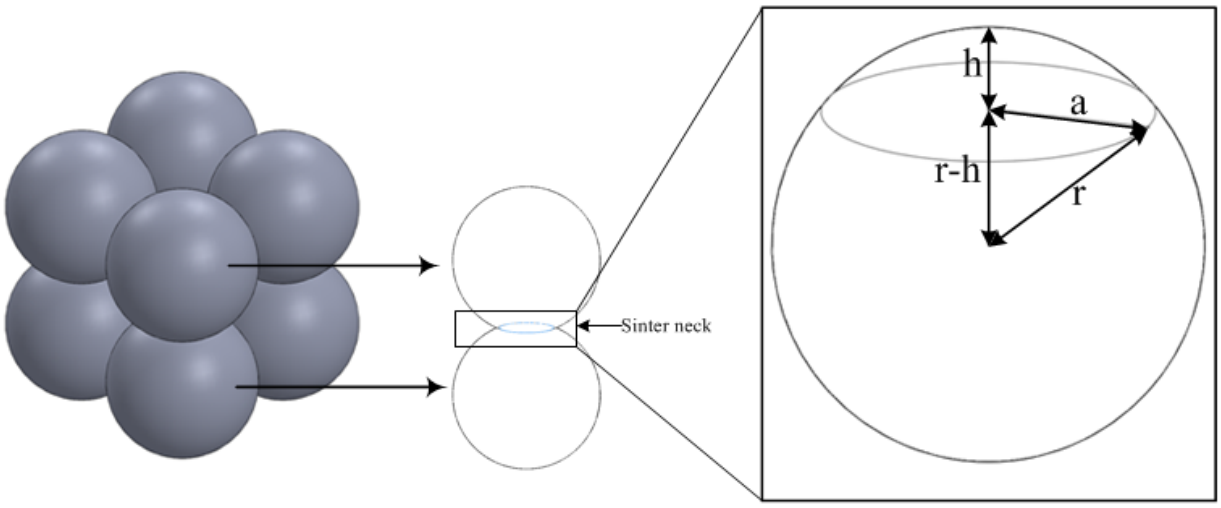

Figure 4-8 Assumed arrangement of particles at micro-scale

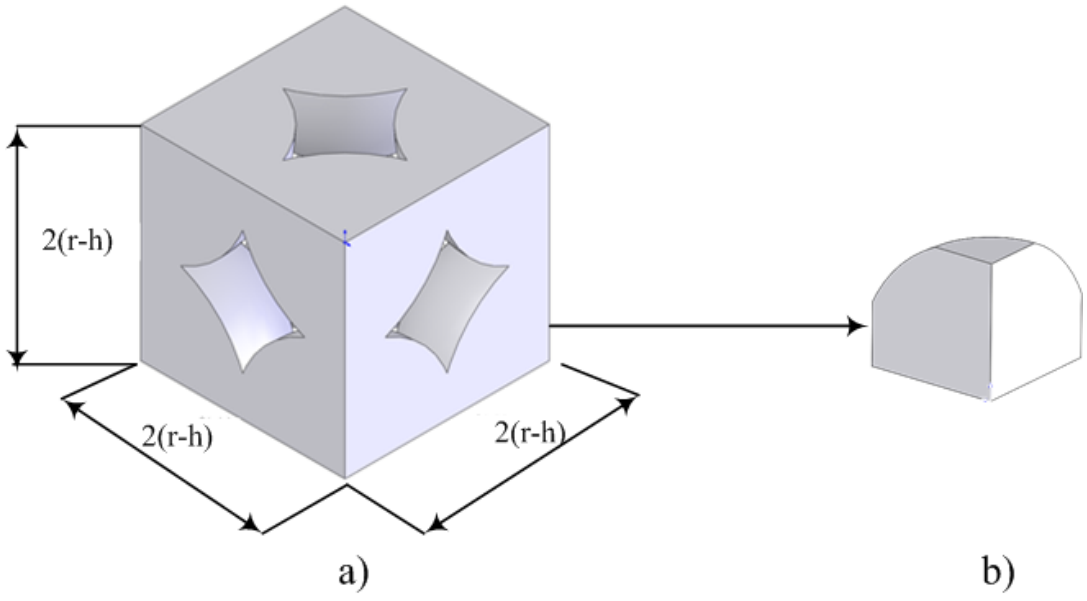

Figure 4-9 a) A cubic unit-cell which represents eight particles each contributed by one-eighth of its volume, b) One-eighth particle represents the participation of the particle in the unit cell after subtracting the volume of the sinter neck from three sides.

In order to calculate the volume of the material that is included in the unit cell, the volume of the overlapped area between the sintered particles is subtracted from the total volume of the material in the unit cell. Thus, the volume of three segments of the participated particle is subtracted from the volume of the particle itself (Figure 4-9b). Generally, the volume of a sphere segment according to Harris and Stocker [95] is:

$$V_{segment} = \frac{1}{3}\pi h^2(3r - h) \quad (3)$$

The interface between any two particles includes a quarter of segment from each particle shared in the sinter neck. Thus, the volume of subtracted segment ($V_{\text{subtracted}}$) from each particle:

$$V_{\text{subtracted}} = \frac{1}{4}V_{segment} \quad (4)$$

Given the volume of the unit cell and the spherical shape, the grain volume (V_g) or total volume of eight particles contributed in the unit cell after subtracting segments of the sinter neck is:

$$V_g = 8 \times \frac{1}{6}\pi r^3 - \frac{1}{4}\pi h^2(3r - h) \quad (5)$$

The volume fraction (V_f) of the unit cell is:

$$V_f = \frac{V_b - V_g}{V_b}$$

$$= \frac{((2 \times (r - h))^3) - (8 \times \frac{1}{6}\pi r^3 - \frac{1}{4}\pi h^2(3r - h))}{(2 \times (r - h))^3} \quad (6)$$

where

V_g= grain volume

V_b= Bulk volume

Porosity (P) is:

$$P = V_f = 1 - \frac{V_g}{V_b} \quad (7)$$

From Figure 4-8, the sinter neck (X) = $2a$, and given the cell geometry and geometrical relationship between r, h and a, the relation between porosity and sinter neck diameter is:

$$P = 1 - \frac{\pi\left(\frac{1}{6}r^3 - \frac{1}{4}\left(r - \sqrt{r^2 - \left(\frac{x}{2}\right)^2}\right)^2\left(3r - \left(r - \sqrt{r^2 - \left(\frac{x}{2}\right)^2}\right)\right)\right)}{\left(r - \left(r - \sqrt{r^2 - \left(\frac{x}{2}\right)^2}\right)\right)^3} \quad (8)$$

This equation is used to predict porosity based on the measured values for X. The sinter neck(X) obtained from the microstructural characterization of the SEM images were used to calculate the theoretical porosity. The porosity obtained from the model was compared against the experimental porosity data to validate the effectiveness of the model in prediction of the porosity of the porous structure using the regression analyses.

4.6 Discussion

The results of this study demonstrate the significant influence of the layer thickness (compaction of powder) and sintering temperature on the porosity, strength, stiffness, and dimensional variation of a Ti porous structure made by a powder bed ink-jet based additive manufacturing technique. The microstructural observation provides an insight into sinter neck size among the particles and its progressive development due to an increase in the compaction of powder or sintering temperature as shown in Figure 4-2. The increase in the compaction of powder increased the contact area/force among the particles, which positively influences the diffusion process among the particles. According to Oh et al.[50], the influence of increasing the pressure in decreasing the porosity is due to the plastic deformation of the particle above the β transition temperature, which may lead to an increase in the contact area between the particles and caused a decrease in the porosity. This effect was clearly proven from the porosity results in Figure 4-3, where at 800 ºC sintering temperature, which is below the β transition temperature, the variation in the porosity due to alteration of the compaction of powder is not remarkable. However, with an increase in the sintering temperature the reduction in the porosity increased significantly with the decrease in the layer thickness. The correlation between the powder compaction and the sinter neck ratio is shown in Figure

4-10. At the thicker layer (175 um), which represents the lowest level of powder compaction, the correlation between the neck ratio and the sintering temperature is linear; however, this linearity degrades gradually when the compaction of powder is increased, as shown by the R^2 value for the other layer thickness.

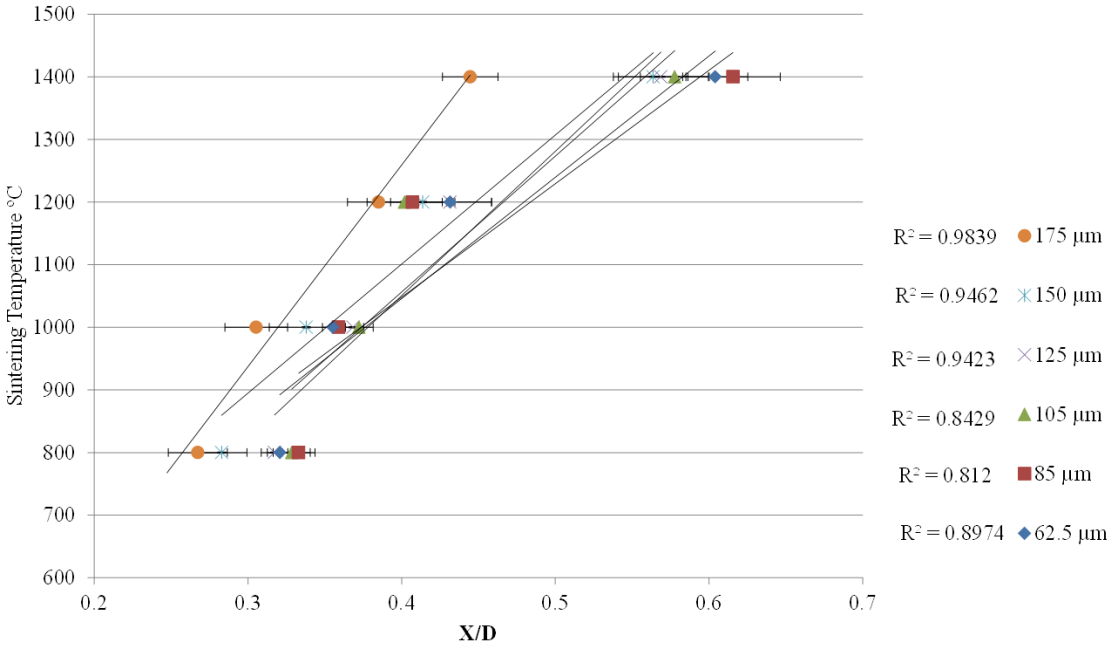

Figure 4-10 The progression of the sinter neck ratio versus sintering temperature

In this study, a model was developed that could predict the porosity of the structure based on the sinter neck measurements achieved by the microstructural observation of sinter neck size using SEM (as typically shown in Figure 4-2). To examine the validity of this model, experimental data is compared with the model output as shown in Figure 4-11. As seen, an excellent correlation ($r^2 = 0.92$) is observed between the model porosity and the experimental porosity of the structure. Statistically, this means that the experimental results are in good agreement with the model results.

Furthermore, the sinter neck has a highly significant impact on yield strength and stiffness of the structure. Figure 4-12 shows that the increase in the sinter neck ratio is associated with an increase in the yield strength of the samples. However, the relationship between the sinter neck and the yield strength at the highest temperature (1400 ºC)

exponentially increases by increasing the level of powder compaction. The correlation of yield strength and Young's modulus is linear, as shown in Figure 4-13. However, this linearity does not occur at the lower sintering temperature (800 ºC). This difference can be attributed to the fragility of the structure at this sintering temperature, since the sinter neck is not fully developed and the elasticity of the structure is very poor under this condition.

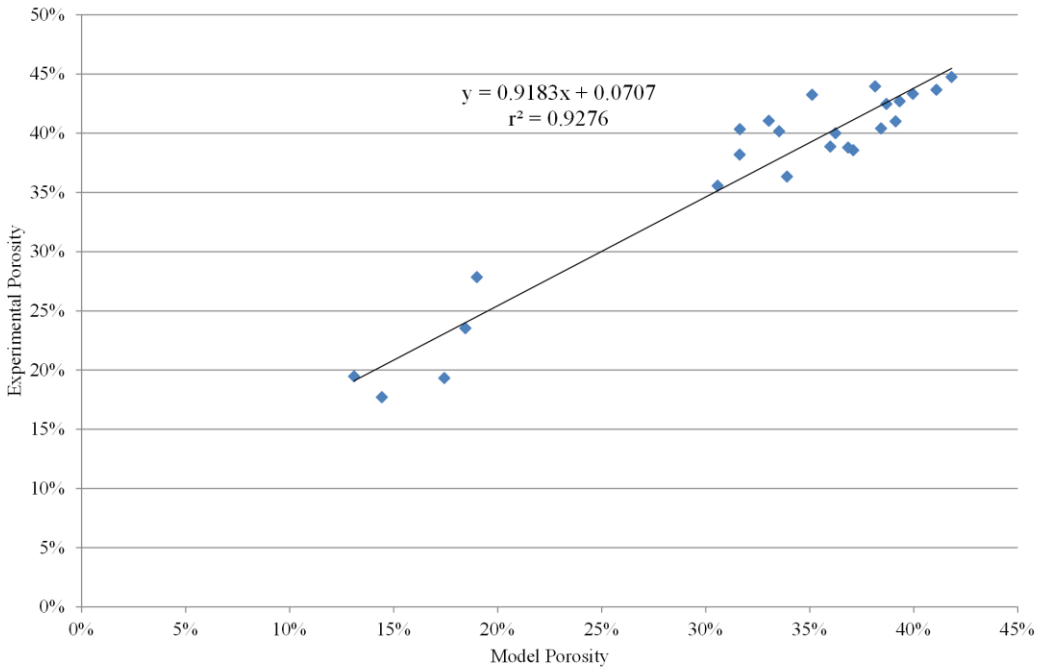

Figure 4-11 Correlation between the experimental porosity and modeled porosity.

In this study, yield strength was considered to characterize the strength in a comparative study among the groups. The highlight over the yield strength comes due to the variation of this property between middle-aged and elderly cortical bone yield strength, while no significant variation in ultimate strength results was detected[96]. According to Figure 4-13, samples compacted by varied layer thicknesses and sintered at 1200 ºC are comparable to cortical bone mechanical properties, yield strength, and stiffness, as reported in the literature [87,97].

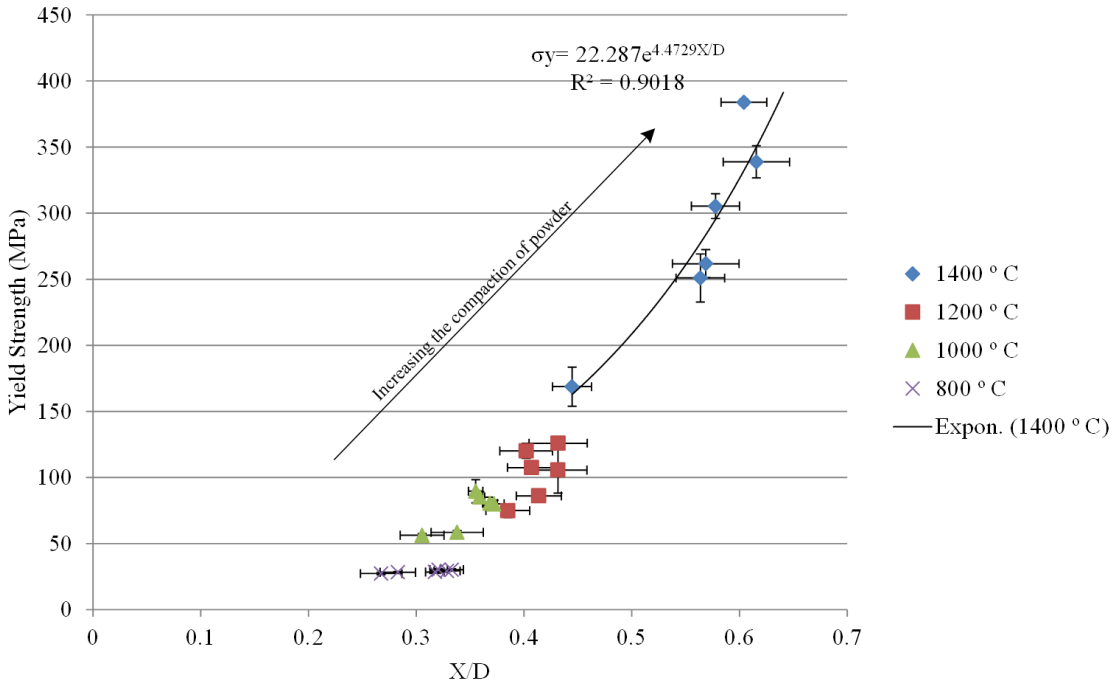

Figure 4-12 Sinter neck ratio as a function of the yield strength at different sintering temperatures.

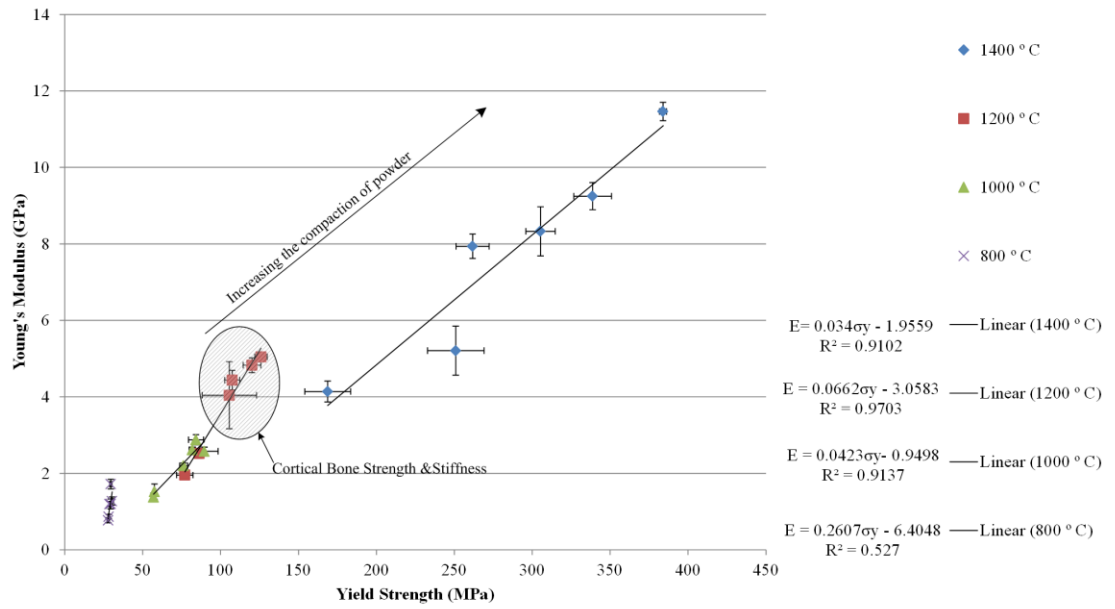

Figure 4-13 Correlation of the yield strength and the Young's modulus and the governing equations for each sintering temperature.

The influence of the compaction level could also explain the variation in the vertical and horizontal shrinkage, as depicted in Figure 4-14. For instance, at a higher compaction level of powder, the horizontal shrinkage is higher than the vertical shrinkage, while at a lower compaction level the vertical shrinkage is higher than the horizontal shrinkage. Our previous work [66] and Wiria et al.[6] suggest that vertical shrinkage was greater than horizontal shrinkage due to gravitational effects. Thus, we considered the horizontal shrinkage as the constant and vertical shrinkage as the variable according to the conditions of the printing or sintering. Accordingly, the effect of the powder compaction on the shrinkage isotropy is shown in Figure 4-14. This figure shows that the optimum layer thickness for maintaining isotropic shrinkage is 105 μm; however, a decrease in the layer thickness leads to less shrinkage in the vertical direction compared to the horizontal direction due to a well compaction of powder and no much of voids left as in the other extreme edge of layer thickness (175 μm). These voids allow for more reliance of the structure toward shrinking in the vertical direction to fill these voids influenced by the gravitational effect.

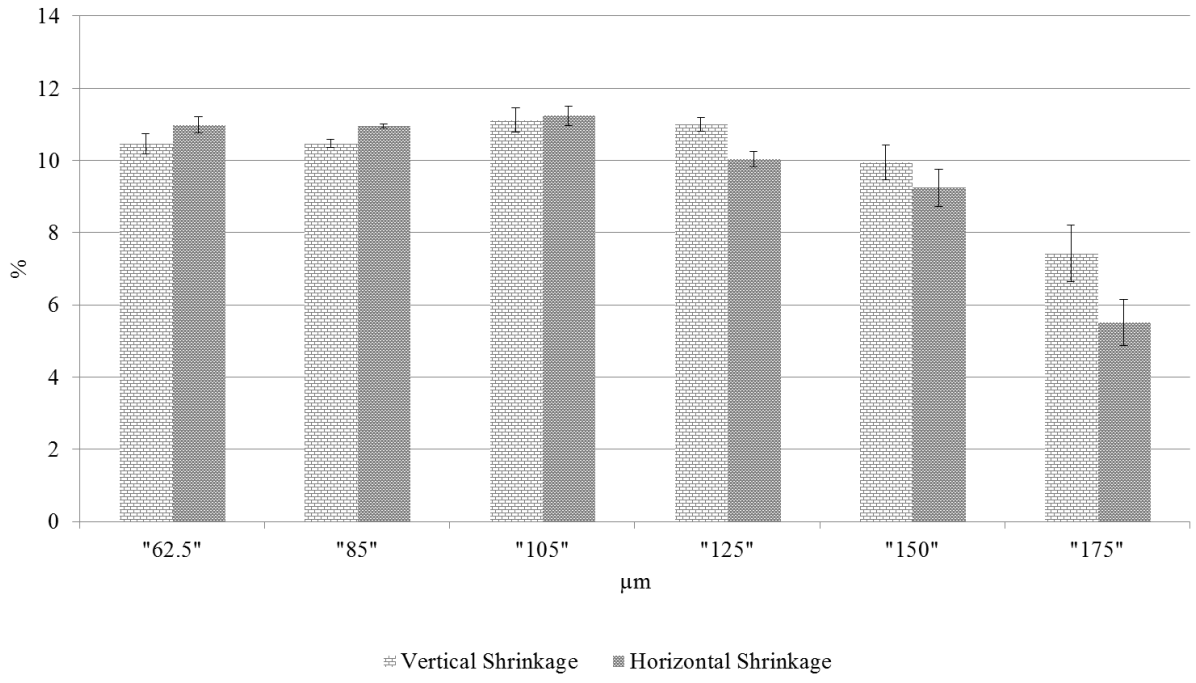

Figure 4-14 Influence of the compaction of powder on the anisotropy of shrinkage in the structure for samples sintered at 1400 ºC.

4.7 Conclusions

Porous Ti samples were additive manufactured using a powder-based ink-jet additive manufacturing process followed by post sintering. The porosity of samples ranged between 17–44 %; Young's modulus ranged between 0.77-11.46 GPa; and yield strength ranged between 27 - 383 MPa, which was achieved by varying the layer thickness and sintering temperature. It was observed that the level of compaction of powder and sintering temperature were two parameters that significantly affect the mechanical and physical properties of the printed structure. In addition, the regression analysis demonstrates a good fit between the porosity model and the experimental data.

Chapter 5 Mechanical Properties of Additive Manufactured Porous Titanium Bio-Structures with Oriented Macro-Scale Channels

5.1 Introduction:

Recently, with improvements in health systems, global life expectancy has increased, thereby leading to an increase in the average age of the world population. Joint diseases and osteoporotic fractures account for 50% of the chronic diseases that affect senior citizens. Specifically, the parts of the body most susceptible to these diseases are the spine, hip, and forearm[69].

For several decades, Ti and its alloys have been increasingly utilized for orthopedic implants, in particular, in repairing large bone defects and in joint replacement owing to their desirable physical and mechanical properties along with their biocompatibility[45]. However, loosening of the implant or failed bonding between the bone and the implant is a common issue associated with the fixation of the bone implant which arise over time[5,70]. This problem is caused by several factors, including mechanical and biological factors. One crucial biological factor is the poor osseointegration between the bone and the implant[5]. For instance, inadequate integration between the cementless implant and the bone allows debris particles to access the interface area between the implant and the bone which in turn leads to the loosening of the implant[5]. Therefore, improving the osseointegration process between the implant and the host bone would be beneficial in

avoiding aseptic loosening. An effective way to alleviate this problem is by designing porous Ti structures that enhance the integration with the bone.

Recently, a few additive manufacturing techniques stated in ASTM F2792 - 12a have been used in fabricating orthopaedic implants due to the ease of production compared to conventional techniques [40,50,52–55,76]. Additive manufacturing techniques are capable of building scaffolds (bone implant) with fine internal and external features. These features might include macro-scale channels and micro-scale pores, and these channels assist the osteointegration process between the implant and the host bone[98,99]. The influence of channels' various sizes or shapes on osteointegration has been the subject of two recent studies[98,99]. In these studies additive manufacturing techniques were used to fabricate macro size channels in the implants. These fabricated implants were biologically tested while the outcomes proving the importance of the channels in improving the osteointegration process. However, no studies have addressed the influence of these channels on the implant's mechanical and physical properties. This study will address the effects of open channels with various orientations on the physical and mechanical properties of additive manufactured porous Ti samples. Porosity, shrinkage, and mechanical properties of additive manufactured porous structure will be investigated.

5.2 Methodology:

The machining process of Ti using conventional techniques is complex; moreover, creating macro channels inside of a Ti construct is considered challenging when using conventional techniques, due to the rigidity and stiffness of Ti. However, with advances in additive manufacturing techniques, this process has become possible with the assistance of a powder based 3D printing (3DP) machine, which is capable of controlling precise features of the internal and external architecture.

In the present study, commercially pure Ti powder (CP Ti, Phelly Materials, Bergenfield, NJ) that meets the ASTM (F67-06 Grade 2) characteristics was used to build the testing samples with the 3DP machine. The as-received powder had a spherical shape with a size range of 45-90 μm. This powder was sifted through a sieve with a mesh size of 200 (US Standard Sieve Series, Cole-Parmer, USA) and the outcome of this process was powder particles in the range of 45-75 μm. Polyvinyl alcohol (PVA) powder 86–89% hydrolyzed

with low molecular weight (Alfa Aesar, Ward Hill, MA) was used as a binder. A mixture of Ti and 3 wt% PVA was mixed for 4 hours using a jar-mill (LABMILL 8000 JAR MILL MACHINE, Paul N. Gardner Company, USA). The production process of samples conducted in two stages: manufacturing and sintering of green samples.

5.2.1 Manufacturing of Green Samples:

Solid-WorksVR, Ver. 2006 (SolidWorks, Concord, MA) was used to create a 3D model for rounded bars with dimensions of Ø10.3×H15.45 mm×mm. These rounded bars were classified into 4 categories according to the design of the experiment. The first category (a) included control samples, as seen in Figure 5-1a. The second category (b) included samples with two vertical channels (Ø1000 μm) running all the way through the sample, as shown in Figure 5-1b. The third category (c) included samples which had two channels (Ø1000 μm) that intersected at the centre and were inclined at 65.3º (Figure 5-1c). This angle is equivalent to the principal stress angle corresponding to the geometry of the control samples obtained by the assistance of COMSOL MULTIPHYSICS 3.5a. ®. The last category (d) included the channels in category (c) in addition to a horizontal channel, which also intersected other two channels at the center, as shown in Figure 5-1d.

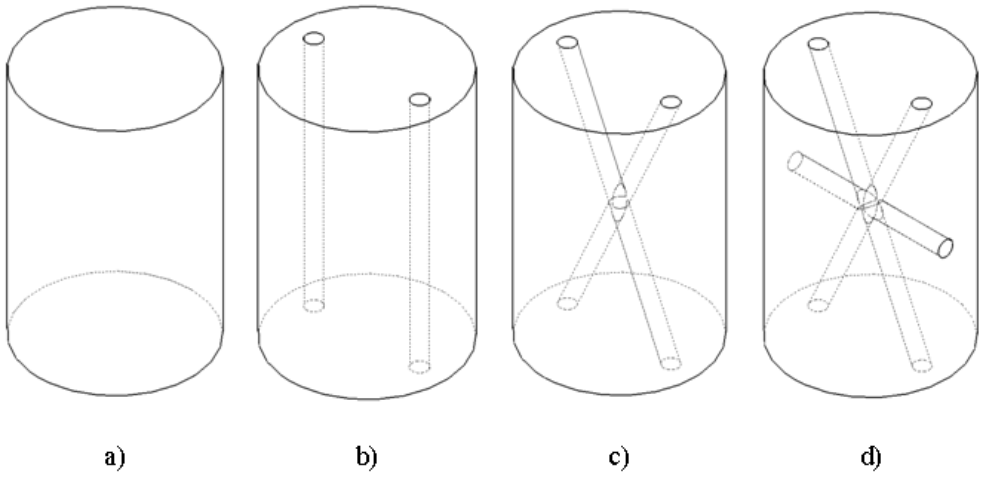

Figure 5-1 Schematic presentation of Ti samples investigated in the current study and classified into four categories: a) control, b) 2 vertical channels at 90º angle, c) 2 channels with 65.3º inclination angle, and d) 2 channels inclined by 65.3º and one horizontal channel

These models were exported to a retrofitted powder-based 3D printing machine (ZPrinter310-Plus, Z Corporation, Burlington, USA) in stereolithography (STL) format.

The printing process depended mainly on the packing of powder layers until the entire structure was built. This process was concurred by the injection of an aqueous solvent (Zb58^{TM}, Z Corporation, Burlington, USA) interfacially between the layers, which represents the 2D shape of the targeted structure. This process was implemented using two pistons, one in the feeding powder side and another in the build, as shown in Figure 5-2. The synchronized movements of these pistons along with the roller, which was used in spreading of powder from the feeding side to the building side, allowed for the packing the powder during the printing process of the structure as reported in our previous work[66].

In order to dry the printed samples, they were kept in the printer at 38 ºC for 1.5 hours following printing. They were then pulled up from the machine and cleaned by compressed air to extract the powder from the channels.

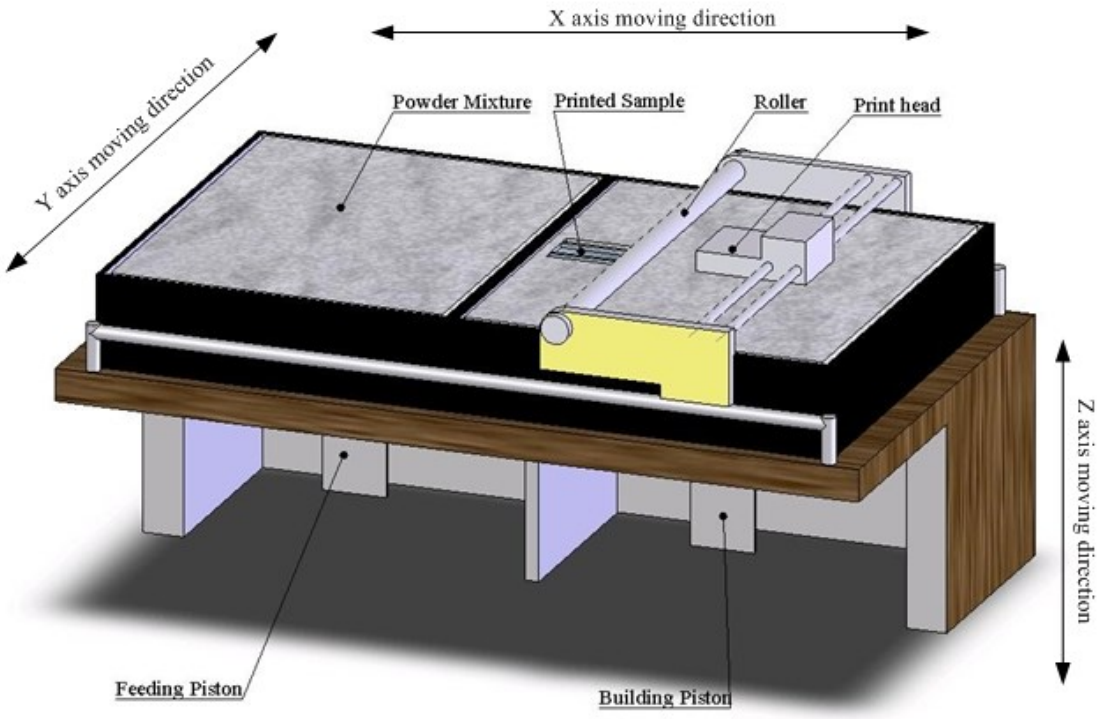

Figure 5-2 A schematic of the powder based 3D printer machine.

5.2.2 Sintering:

Green samples produced by the printing process were sintered to obtain the final porous structure. An MTI® High Temperature Tube Furnace (GSL—1500X-50, Richmond, CA) and Argon atmosphere were used for sintering. The sintering process was initiated by first burning the PVA used for the binding of Ti particles of green samples. The PVA burning process was implemented through two stages: first at 295 ºC for 3 hours in an air environment, and second at 500 ºC for 1 hour in an Argon environment. Next, samples were sintered at 1400ºC for 1 hour. The heating rate was 10ºC/min until reaching 1000ºC, and then reduced to 5ºC/min until reaching 1400ºC, as shown in Figure 5-3. The samples were then furnace cooled at the end of sintering. Finally, the sintered samples were cleaned in an ultrasonic bath filled with distilled water for 5 minutes. Figure 5-4, shows a sintered and cleaned sample.

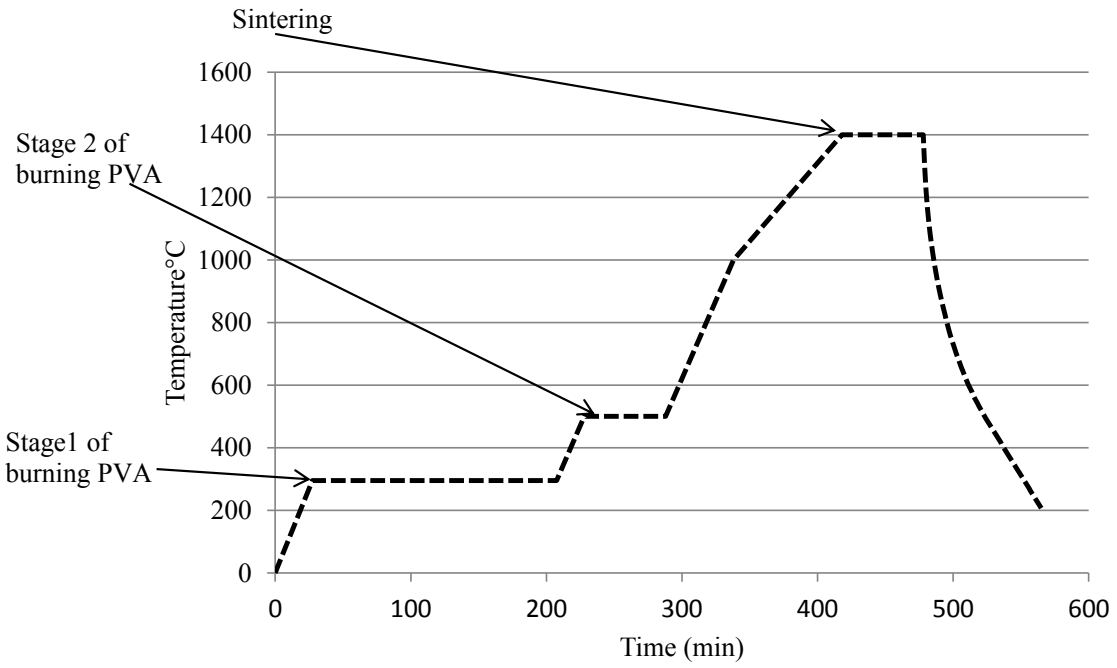

Figure 5-3 Heating profile used in the sintering process.

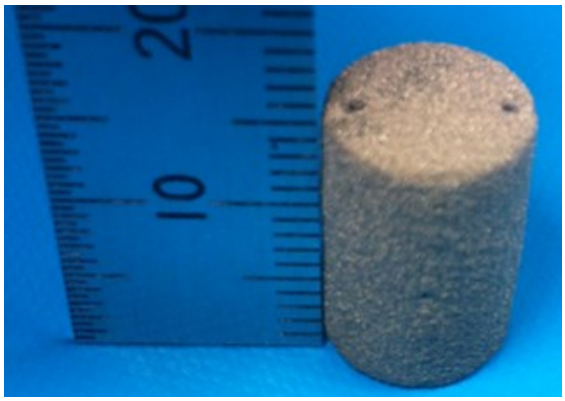

Figure 5-4 Ti sample with two diagonal channels with dimensions of Ø10 mm X H15mm.

5.2.3 Characterization:

In this study, samples were characterized by two non-destructive test methods; i.e shrinkage and porosity measurements, and one destructive test method, which was the compression test.

An electronic Vernier Caliber was used for the shrinkage measurements. As reported in our previous work[66], this test was implemented by measuring the sample diameter before (d_b) and after (d_a) the sintering process, and height before (h_b) and after (h_a) the sintering process three times for each sample and the averages were considered. The percentages of shrinkage in vertical (%V) and horizontal (%H) directions were calculated from the following formula:

$$H\% = \frac{d_a - d_b}{d_b} \times 100 \quad (1)$$

$$V\% = \frac{h_a - h_b}{h_b} \times 100 \quad (2)$$

Archimedes' principle of buoyancy was adopted to measure the porosity of the samples based on ASTM B 311& C373. In this characterization technique, three readings were taken before and after boiling the sample in distilled water to remove air bubbles trapped inside the sample's pores. These readings were; sample dry weight (W_{dry}), wet weight (W_{wet}), and submerged weight (W_{sub}). The measured porosity was obtained from the following formula:

$$\text{Porosity } \% = \frac{W_{wet} - W_{dry}}{W_{wet} - W_{Sub}} \quad (3)$$

An Instron machine (Instron-4206, USA) was used for compression testing with a cross head speed of 1mm/min. Sample dimensions were Ø10.3× 15.45 mm^2, and 4 samples from each category were tested. The results were analysed statistically using analysis of variance (ANOVA) technique to examine the differences between categories' averages. Any significant result within the collected data was detected by alpha value ($p<0.05$), and if that condition was satisfied then a Bonferroni correction technique was used to discover the significance within the categories [100].

5.2.4 Modelling:

Finite Element Analysis (FEA) using COMSOL MULTIPHYSICS 3.5a ® was employed to investigate the mechanical influence of macro channels on the structure among four different categories with different channels orientation. The outcome of the printing process was a porous structure. Due to the technical complication in the modelling of a porous structure[101], the structure was assumed to be solid and the mechanical data and equivalent density based on the porosity of the structure were then used as input material properties in the FEA. A static analysis was implemented by applying an axial load on the samples to simulate the compression test. The results of the mesh generation process (as shown in Figure 5-5) were 2888 elements for category a) , 16571 elements for category b), 17192 elements for category c) and 23141 elements for category d). The Von Mises results were used to address the influence of macro channels existence in the structure and the stress concentration among four different categories of samples.

5.2.5 Biological Study:

Human osteosarcoma cell line (Saos-2) were cultured in McCoy's-5A medium supplemented with 10% fetal bovine serum (Sigma–Aldrich). Prior to seeding process, the samples (n=20) were placed in a 24-well tissue culture plate to be equilibrated with the 1 ml complete culture medium for 15 min. After that, the medium removed from the plate before the seeding process, and followed by an immediate seeding of 100,000 cells per sample. Samples were left for 30 min for cell attachment. Then, 1 ml of medium added to the samples at 37 ºC, and this medium was changed on days 3,7,10 ,and 14.

The cell proliferation and osteoblast phenotype were assessed through; the alamarBlue® Assay,Picogreen® assay DNA content, alkaline phosphatase activity, and Osteocalcin production .

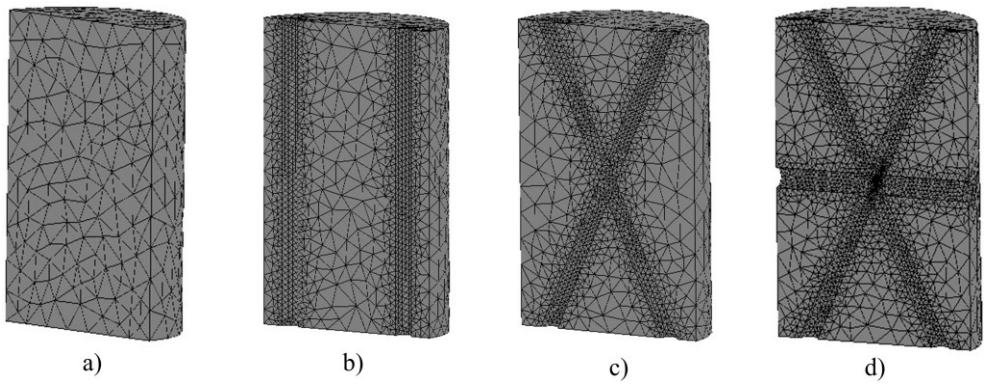

Figure 5-5 Samples after meshing process : a) control, b) 2 vertical channels with 90º angle, c) 2 channels with 65.3º inclination angle, and d) 2 channels inclined by 65.3º and one horizontal channel.

5.3 Results

5.3.1 Shrinkage:

The results of the shrinkage analysis in the horizontal and vertical directions are presented in Figure 5-6. No significant variation in horizontal or vertical shrinkage among the categories is observed. The percentage of shrinkage is between 3.5 and 4.5% in both directions.

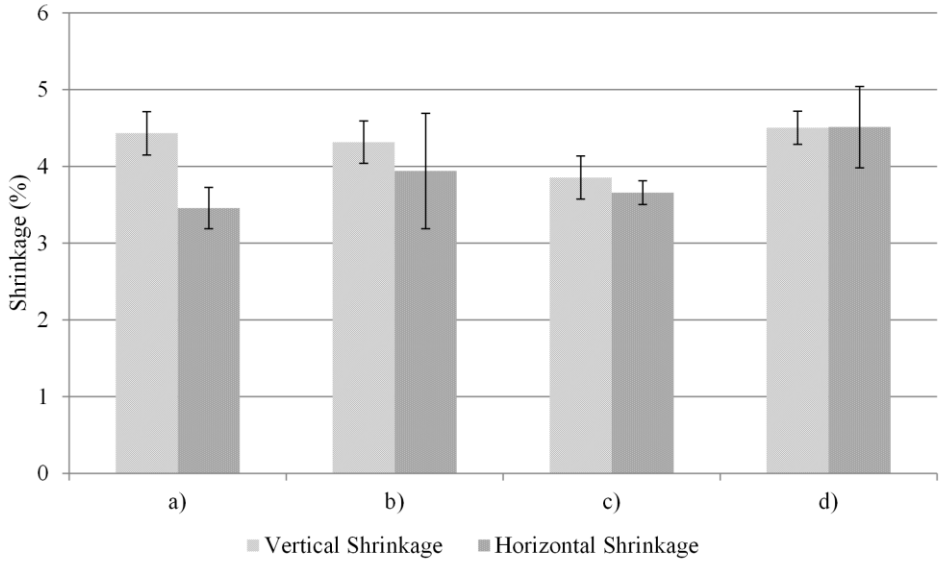

Figure 5-6 Vertical and horizontal shrinkage of Ti samples after the sintering process.

5.3.2 Porosity:

The average porosities of 4 samples from each category are presented in Figure 5-7. From this figure, there appears to be no significant variation between the first three categories and the porosities range from 35-35.5%; however, a significant reduction ($p<0.05$) in the porosity of category (d) compared to (a) , i.e. ~33.6%, is observed.

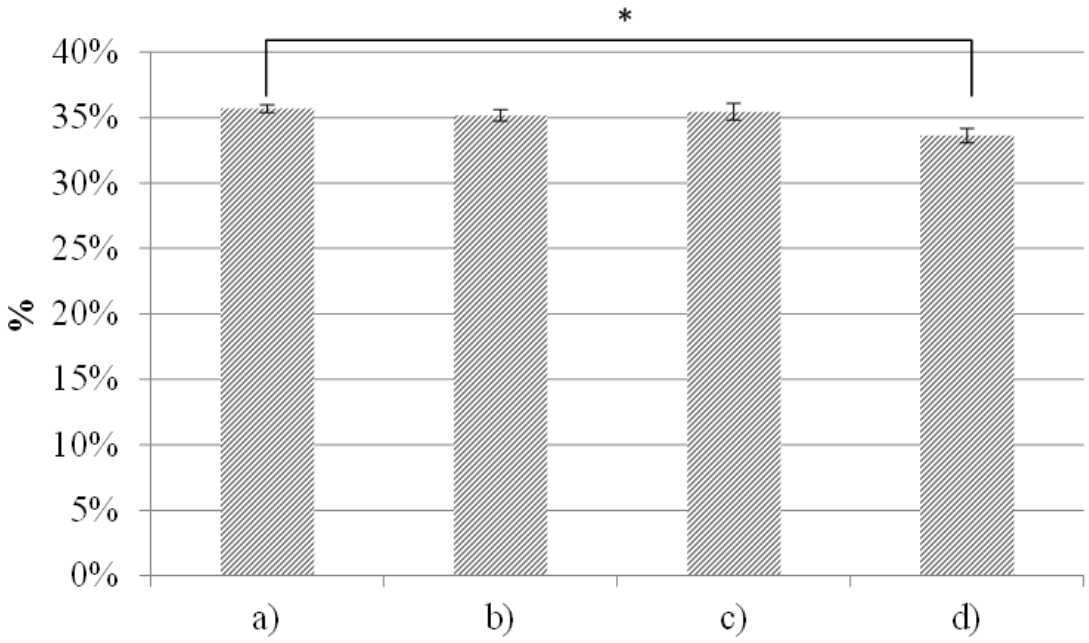

Figure 5-7 Porosity of Ti samples fabricated with different channel orientations.

5.3.3 Mechanical Properties:

The mechanical properties of the different samples characterized by the compression test are listed in Table 5-1. In addition, the table includes the range of the mechanical properties of cortical bone based on various ages as characterized by the compression test. The statistical examination test (ANOVA) revealed no significance difference in terms of the mechanical properties among categories a, b, c, and d with the exception of the ultimate compressive strength. The ultimate compressive strength results are presented in Figure 5-8. As shown in this figure, there is a slight improvement in the strength of the structure due to the creation of vertical or inclined channels in the

direction of the principal stress; however, a significant reduction in the strength ($p<0.05$) occurred after adding a horizontal channel.

Table 5-1 Mechanical properties obtained from the stress-strain curve for a) control; b) 2 vertical channels with 90º angle; c) 2 channels with 65.3º inclination angle; and d) 2 channels inclined by 65.3º and one horizontal channel.

	Yield Strength 0.2%(σ_y) MPa	**Elastic Modulus (E) GPa**	**Yield Strain(ε) %**	**Ultimate Strength MPa**
a	154.9 ± 9.2	3.25 ± 0.35	5.25 ± 0.84	374.27 ± 31.7
b	155.09 ± 3.4	3.37 ± 0.32	4.96 ± 0.54	392.70 ± 23.5
c	148.83 ± 6.2	3.18 ± 0.13	4.91 ± 0.37	414.51 ± 25.2
d	165.61 ± 3.3	2.98 ± 0.16	5.79 ± 0.28	306.61 ± 8.5
Cortical Bone Based on Age[102]	50-232.5	4.25-22.5	0.72-1.45	52.7-246.3

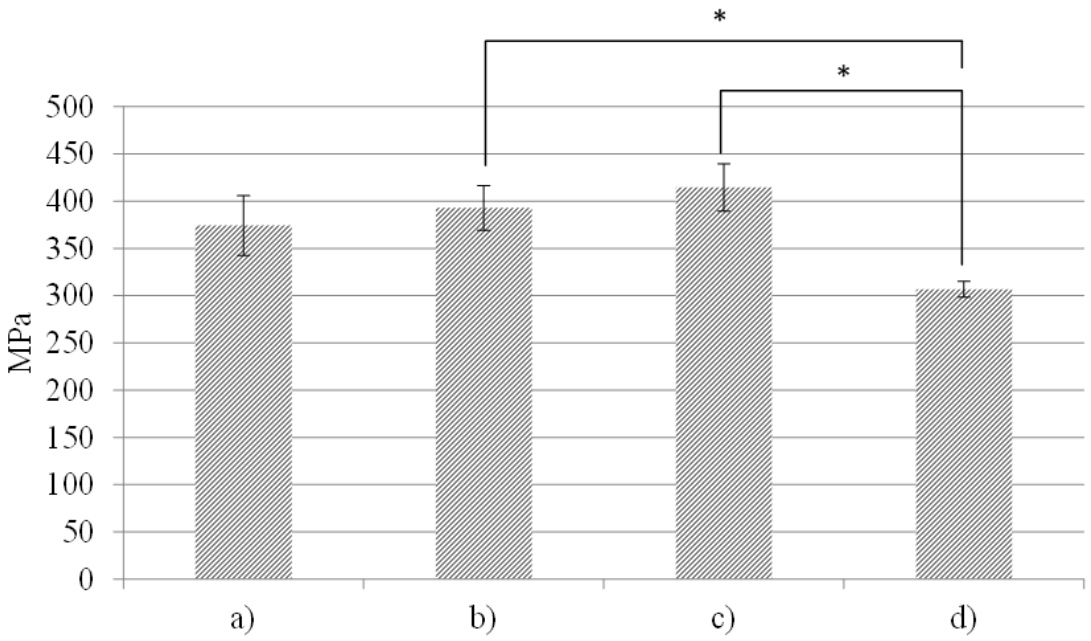

Figure 5-8 Compressive strength resulting from testing Ti samples under the uniaxial compression test: reduction in the strength of the (d) category was significant ($p<0.05$) when compared to the (c) category.

5.3.4 Biological Study:

A cell culturing on the samples conducted at The University of Manchester to assess the cell proliferation within the porous structure as shown in Appendix A. The results of the channels orientation influence on the cell proliferation available in Appendix B, however,

it's early to judge on these preliminary results. This result needs further investigation in the future.

5.4 Discussion

A powder-bed additive manufacturing was deployed to make porous Ti structures with macro-sized channels with different orientations. While the additive manufacturing was enabled to make such structures, the shrinkage due to the sintering post-processing could potentially undermine the potential of the manufacturing process. And giving the fact that orthopaedic implant should be manufactured precisely to be able to fit in the affected area. So, any change in dimensions during manufacturing may cause part rejection due to dimensional variation. Thus, shrinkage level should be maintained at a minimum level and preferably be consistent in all Cartesian coordinates.

Generally, the level of shrinkage is anisotropic that differs for the horizontal and vertical directions of the sintered samples and usually occurs more so in the vertical direction due to the effect of gravity[6,66]. Thus, maintaining isotropic level of shrinkage in all directions will facilitate control over the exact dimensions of the final product, especially in a complex structure. Early control of shrinkage should be implemented from the beginning at the CAD model stage before printing by adding a compensation factor as a percentage of shrinkage for the whole structure, which usually occurs after the sintering process.

In general, according to the shrinkage analysis in the current study, the vertical shrinkage fell between 4.24±0.16 - 4.50±0.11%, while the horizontal shrinkage fell in the range of 3.46±0.11-4.51±0.26%. The influence of the gravitational force on the structure shrinkage cannot be neglected. However, for samples with vertical channels in category (b), the result showed an isotropic shrinkage in both directions (as shown in Figure 5-6 b). A close look at the channel opening in Figure 5-9 suggests that a cluster of well-sintered particles formed around the channel compared to the particles scattering out of the red circle. This phenomenon can explain the isotropic shrinkage which occurred in category (d) and partially in category (b) and (C) samples, since the inner surface of the vertical channels was exposed more to the heat treatment compared to the other parts of the structure. Therefore, particles in the inner wall of the channels built thicker sinter necks and bonded to each other. This formed a higher density area which resists the

gravitational influence and prevented the structure from shrinking vertically during the cooling period. Also, the reduction in the porosity of the category (d) samples which has higher surface area exposed to heat treatment supports the hypothesis of the variation of density within the structure. This variation in sintering performance between the internal structure and the extremity surfaces is supported by the study of Gagg et al. [103]. Based on the morphology data in their study, the authors observed that the porosity in the centre of the cylindrical samples was higher than the porosity at the periphery. This could be attributed to the thicker sinter neck in the peripheral area, which is more exposed to the thermal source.

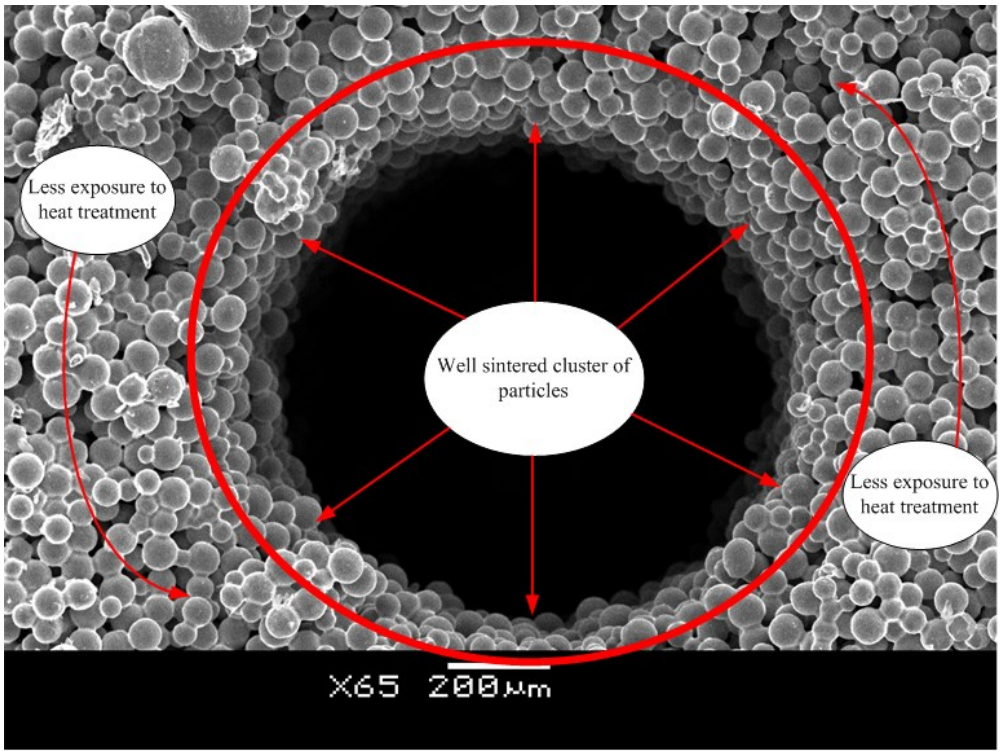

Figure 5-9 SEM images of the channel opening of category (b) samples.

This technique of manufacturing Ti implants proved its superiority in having a low shrinkage level compared to other costly manufacturing counterparts which have been used in the manufacturing of porous Ti, such as electron beam melting (EBM), which has shown a horizontal shrinkage of 6.5% and vertical shrinkage of 7.1%[76]. As well, other techniques such as the indirect additive manufacturing of Ti scaffold by printing a

scaffold of wax and filling it with Ti slurry showed horizontal and vertical shrinkages after sintering at 1300°C equal to 11.9%±1.1% and 9.2%±0.6%, respectively[52].

In the current study, the level of porosity was between 33.64±0.47% and 35.69±0.25%, as shown in Figure 5-7. The presence of channels in the structure affected the porosity of category (d) samples significantly, due to an increase in the surface area which was exposed to heat treatment. In general, the compressive strength inversely scales with the porosity of a porous material [77]. In contrast, Figure 5-8 shows a different behaviour associated with the horizontal channel in category (d) structures. Apparently, the significant reduction in the strength is caused by the existence of the horizontal channels.

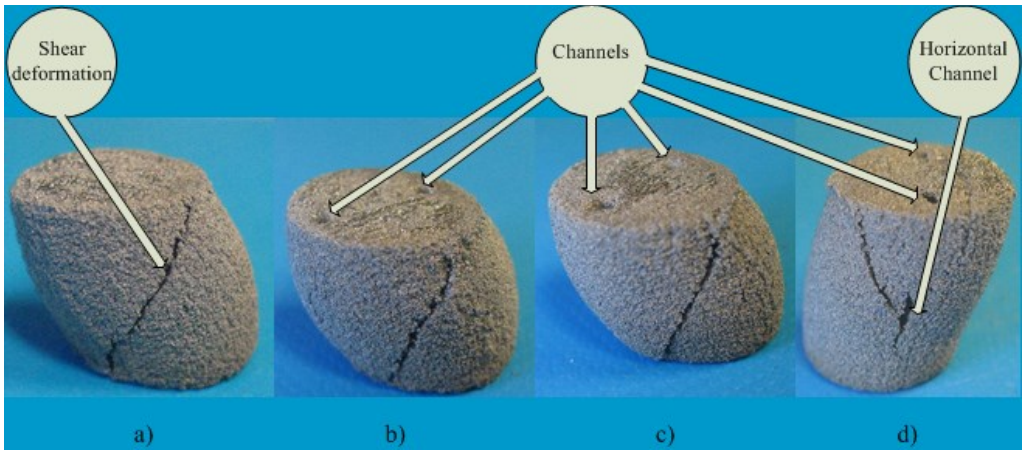

Figure 5-10 Deformed Ti samples after the compression test: a) control, b) 2 vertical channels with 90º angle, c) 2 channels with 65.3º inclination angle, and d) 2 channels inclined by 65.3º and one horizontal channel.

As seen, the inclusion of vertical or inclined channels in the structure does not negatively affect the strength of the structure; in the contrary, these channels enhanced the strength of the structure slightly as shown in Figure 5-8 (b) and (c). However, adding a horizontal channel to the structure, as in category (d), has significantly reduced the compressive strength ($p<0.05$). This observation can be evaluated by the visual examination of the mechanically tested samples. As Figure 5-10 depicts, the failure mechanism in the samples of all categories is sheared along a ~65° plane, which represent the principal stress angle and the shear stress at this specific plane is the maximum. Also, cracks have not initiated or passed through vertical or inclined channels as in the first three categories

[Figure 5-10 (a), (b), and (c)], while these cracks clearly passed through a horizontal channel as in Figure 5-10 (d). The FEA results provide insight into the influence of these channels on the structure. Figure 5-11 (d) shows that the stress concentration is more highly localized in the horizontal channel due to axial loading, while such concentration does not appear in the vertical channels [Figure 5-11 (b)] and appear slightly in the inclined channels [Figure 5-11 (c)]. Although the FEM analysis dealt with the structure as a bulk metal with a reduced density, the case is completely different during the experimental characterization. Characterization of a porous structure is not similar to the bulk material because the mechanical properties of the porous structure conceptually depends upon the density and the microstructural architecture of the construct [104,105]. As the variation in the microstructure will highly change the mechanical properties, the same doctrine could be applied to the macro- structure. Thus, including macro channels in the structure should influence the mechanical properties of the structure. In the present study, adding more channels to the structure as in category (d) led to a significant reduction in the ultimate strength of the structure, as seen in Figure 5-8. This point can be advantageous as one may tailor the mechanical strength of the implant by adding channels that can be realized by AM. In this study, as seen from Table 5-1 some of the obtained mechanical properties fell in the range of the cortical bone and other are very close to this range. The scope of this study was to assess the influence of channel orientation on the properties of the structure when the processing parameters were fixed and not altered. However, several processing parameters could be manipulated to match the properties of the structure to those of the bone, as conducted in our previous work[66]. Overall, a few number of channels have been used in each category and the results showed some variations up and down. These variations expected to be scaled up or down if the number of channels increased in a certain category.

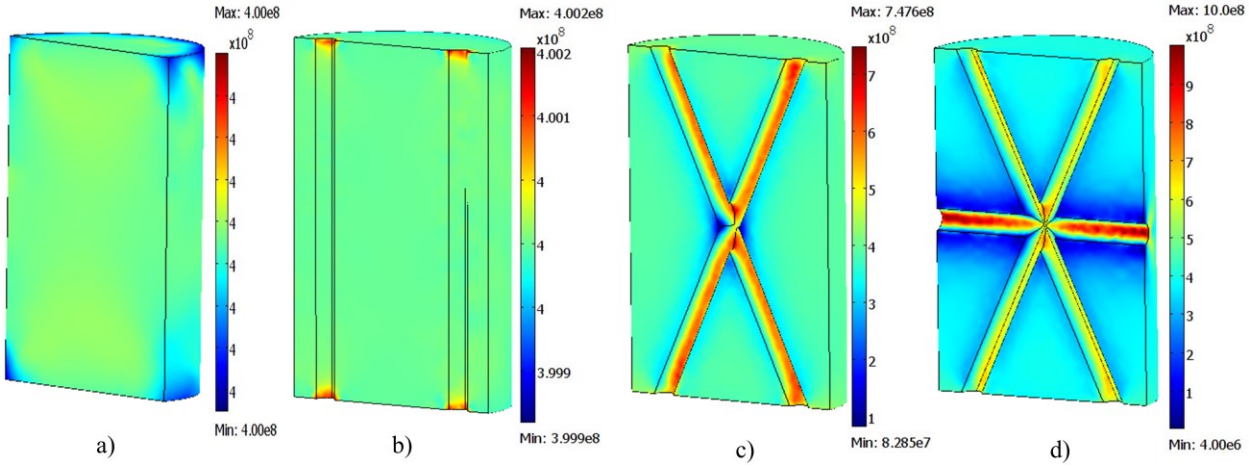

Figure 5-11 Von Mises stress distribution within the compressed samples: a) control, b) 2 vertical channels with 90º angle, c) 2 channels with 65.3º inclination angle, and d) 2 channels inclined by 65.3º and one horizontal channel.

5.5 Conclusions

The influence of macro channels with different orientations upon the mechanical and physical properties of a porous Ti structure fabricated by additive manufacturing technique was investigated. The following conclusions can be drawn from this study:

- The results of the experimental work have proved the possibility of customizing the mechanical and physical properties of the porous structure through the additive manufacturing of bio-structures with macro-scale channels at different orientations.
- The results of the compression test indicated that the ultimate strength of the additively manufactured structure can be tailored and reduced by adding horizontal channels.
- An increase in the number of channels in the additively manufactured structures led to a reduction in porosity due to an increase in the surface area which is exposed to heat treatment during the sintering process.
- The investigation suggested that shrinkage in both horizontal and vertical directions of the sample can be isotropic by adding horizontal channels to the structure.

Chapter 6 A Novel Additive Manufacturing-based Technique for Developing Bio-structures with Conformal and Encapsulated Channels

6.1. Introduction

Most fractured bones heal without any need to surgery. Yet treatment of a fracture can be challenging if the gap between the fractured parts of the bone exceeds 2 mm [106], as this gap will hinder revascularization and cell proliferation [107]. Therefore, utilizing a customized implant to precisly mimic the anatomical shape as well as geometrical features of the cuts required for surgery can be considered a viable solution to this issue.

The structure of an appropriate bone implant should mimic the structure of real bone. Cortical bone is composed of hydroxyapatite and type-I collagen, and its porosity is in the range of 3-12% [22,108]. The structure of this type of bone includes the osteon system, which consists of a network of channels: longitudinal channels (Haversian canals) linked by transverse channels (Volkmanns canals). The main function of these channels is to serve as conduits for blood vessels, which are crucial for nutrition, growing bone, and repairing fractured sites [109].

According to Frosch et al. and Fukuda et al. [98,99], it is essentail for Ti bone implants to have such channels to improve the osseointegration process. In these studies, longitudinal channels ranging in size from 300-1000 μm were drilled, as in [98], or channels were

fabricated ranging in size from 500-1000 μm using one of the additive manufacturing (AM) techniques, i.e., Selective Laser Melting (SLM), as introduced in reference [99]. In the studies conducted in [98,99] no encapsulated channels were created due to difficulties in creating macro-sized encapsulated and conformal channels in the printed structure as a result of the depowdering issue [110].

The fabrication of a macro-sized channel using the powder bed AM technique is complex because of the difficulty associated with depowdering, i.e., removing loose powder from the fine details of the structure [58,68,111,112]. Macro-channels exemplify the fine details inside the 3D printed structure. So, while depowdering of straight macro channels is challenging, it is not a practical process for the case of conformal and encapsulated macro-channels. Thus, depowdering after printing is a significant issue, and the inability to accomplish this task is considered to be a major impediment in the use of powder bed additive manufacturing techniques.

There have been many attempts to overcome the depowdering issue in 3D printed green parts. Some of these attempts have focused on the design of the targeted model to overcome this problem, as dicussed in reference [111], according to which the scaffold was designed as a cage with large windows to facilitate the depowdering process. Other attempts have included changing some of the manufacturing parameters. For instance, the orientation of the samples in the powder bed and its influence on the depowdering process were investigated by Farzadi et al. [88]. In that study, cylindrical scaffolds were printed in the X (horizontally in the powder spreading direction), Y (horizontally perpendicular to the powder spreading direction), and Z direction (vertical). The depowdering of samples that were printed horizontally in the X direction was somewhat easier to accomplish than the depowdering of samples that were printed in the Y direction. For both the X and Y printing directions, the samples were easier to depowder in terms of the cleaning time required compared to those printed in the Z direction.

Since the primary goal of this study was the creation of macro-sized channels in order to mimic the structure of real cortical bone, depowdering of these horizontal and vertical channels (which has not been addressed in the literature to date) was a major concern. In this study, the new approach of combining three manufacturing techniques, i.e. additive manufacturing of laminated/partial parts and assembling/stacking the laminated parts,

followed by a propoer sintering protocol was used in an attempt to overcome the depowdering obstacle of these channels. This new manufacturing approach was assessed by a comparative characterization of mechanical and physical properties of the fabricated samples (i.e. shear and compressive strengths, and porosity and dimensional shrinkage).

6.2. Methodology

6.2.1 Materials and Fabrication

The CAD model of the assembled additive manufactured (AAM) part was first developed using SolidWorksVR, Ver. 2013 (SolidWorks, Concord, MA, USA). After developing the model, which included a vertical channel (ϕ 1000 μm) and a horizontal channel (ϕ 500 μm), the model was sliced with a cut that went all the way through the channels, as shown in Figure 6-1. Then, two slide guiders were added to the part at the plane of the cut. The appropriate clearance was considered in the design of these guiders to allow them to fit in the holes part of the counterpart. Then, the individual models were printed separately using a powder-bed 3D Printer (ZPrinter310-Plus, Z Corporation, Burlington, VT, USA) with a layer thickness of 85 μm packed with a mixture of powder. This mixture was composed of commercially pure Ti powder (CP Ti Grade 1, Advanced Powders and Coatings, Inc., Boisbriand, QC, Canada) that had spherically-shaped particles with diameters less than 38 μm and 3 wt% of low molecular weight polyvinyl alcohol (PVA) powder that was 86–89% hydrolyzed (Alfa Aesar, Ward Hill, MA, USA). The PVA was used to bind the spherical Ti particles together after the jetting of the liquid binder (Zb^{TM}58 , 3D Systems, Rock Hill, SC, USA) from the print head. Once the printed parts dried, the green parts were depowdered and cleaned using compressed air and a soft brush.

The next processing step is the sintering of the green parts after the assembly. This process was conducted in an MTI® High Temperature Tube Furnace (GSL—1500X-50, Richmond, CA, USA) under a high-purity argon atmosphere. The sintering process consists of two stages. First, the binding agent, PVA, is burned by heating in air for three hours at 295°C, followed by purging argon gas and heating for one hour at 500° C. Second, the Ti is sintered by heating the structure at the rate of 10°C/min to 1000°C,

followed by heating at 5°C/min to 1400°C. This temperature is maintained for three hours, followed by furnace cooling. The heating protocol for sintering is shown in Figure 6-2.

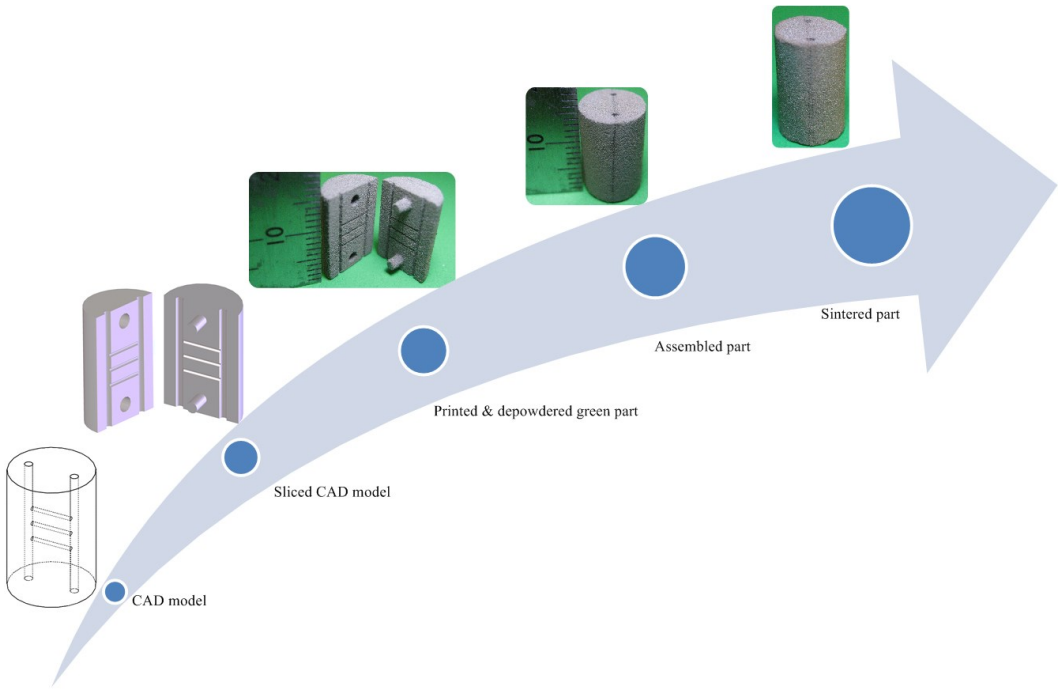

Figure 6-1 Steps of building a structure using the AAM concept, starting with the CAD model and ending with the final sintered structure.

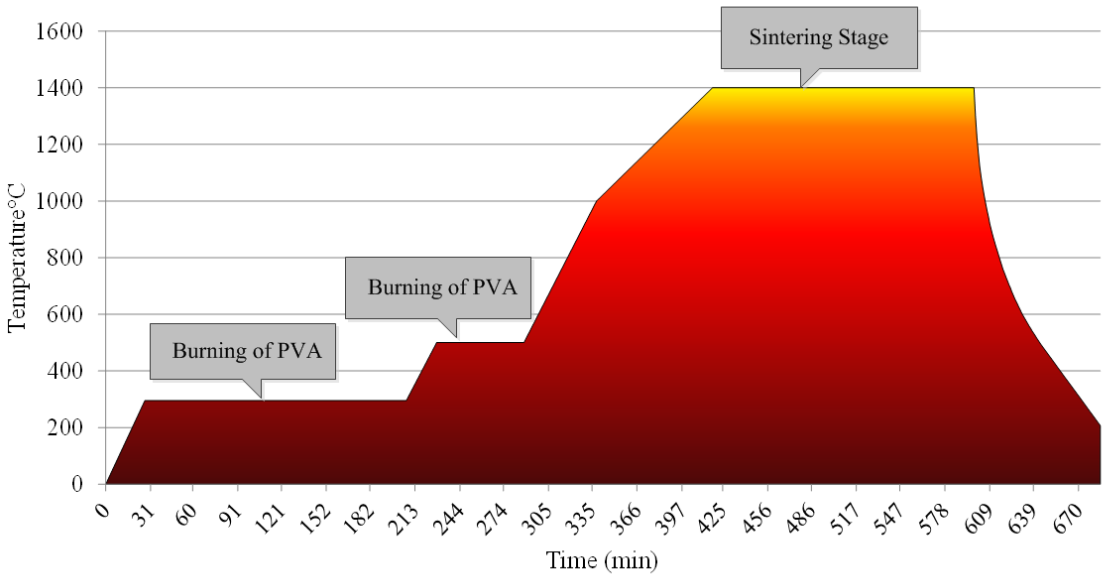

Figure 6-2 Heating protocol used in the sintering process: two stages for burning PVA and one stage for sintering Ti particles.

6.2.2 Characterization

To validate the AAM concept, samples (B) fabricated by this technique were characterized for their mechanical and physical properties and compared with control samples (A), which were printed in one printing cycle as shown in Figure 6-3. In addition, the characterization included a comparison between two categories of samples with horizontal channels (ϕ 750µm). The samples in the first category were printed entirely during one printing job as in category (C), while the second category (D) included the samples printed using the AAM technique. The sample shape characteristics are shown in Figure 6-3. A sample with a straight horizontal channel was chosen to make the depowdering process easier, particularly in category C, since, as mentioned previously, it is not possible to depowder small-sized conformal channels that are printed using a commercially-available 3D printer. Thus, this choice provides the basis for a valid comparison between the two categories.

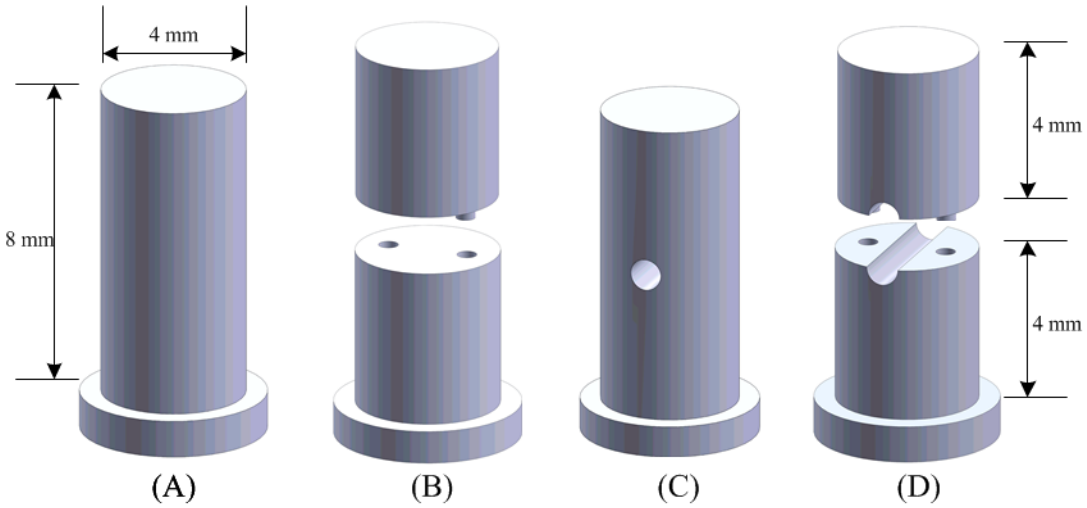

Figure 6-3 Schematic representation of the shear test samples: A) control sample printed entirely in one cycle of printing; B) AAM sample; C) control sample printed in one printing cycle with a horizontal channel; D) AAM sample with a horizontal channel.

6.2.2.1 Shear Test

First, the samples were characterized through a shear testing method to quantify the shear strength of the adhesive bonding in the assembled structure. A specific fixture (Figure 6-4), similar to the fixture used by Bondioli et al., Salazar et al., and Cocr et al. [113–115],

was fabricated to conduct the shear test. The fixture consisted of two pieces: a piston and a cylinder composed of hardened tools steel . One side of the both piston and cylinder was flattened, and a plate was installed in the section that was cut from the cylinder to ensure that a straight shear cut was applied on the interfacial portion between the two parts in categories (B) and (D) and on the control sample categories. The test sample was placed in the 4-mm hole that had been drilled in both the plate and the piston. The entire set, i.e., the sample and the fixture, was subjected to a compression load in a uniaxial Instron machine (Instron-4206, MA, USA) with a crosshead speed of 0.5 mm/min. This compression loading resulted in the application of a shear load at the interface layer between the two assembled parts.

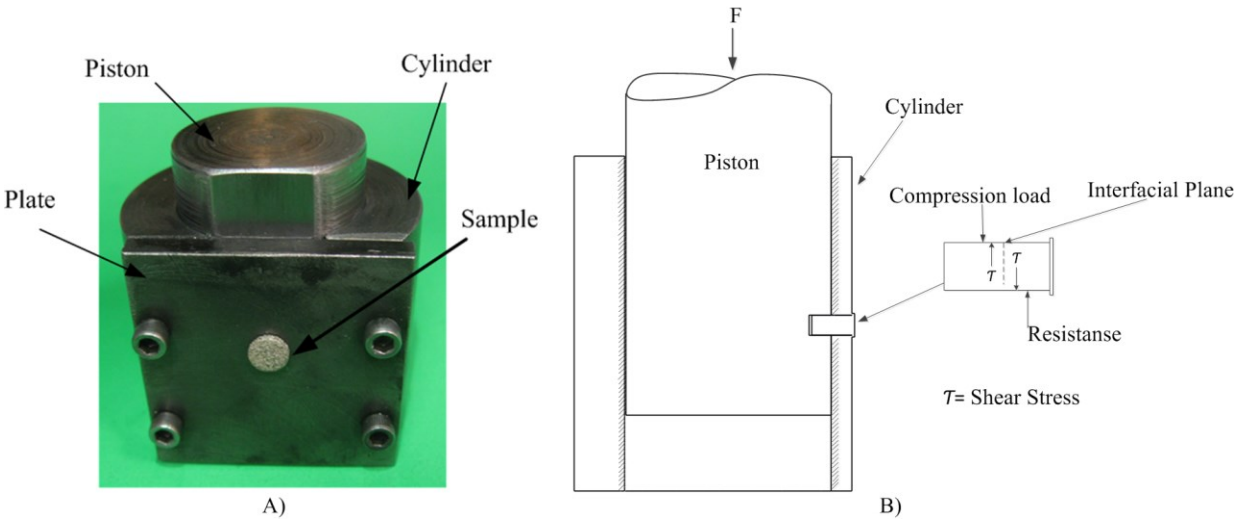

Figure 6-4 Shear test apparatus: A) fixture comprised of a fixed part (cylinder) attached to the plate holds the sample and a moving part (piston), B) schematic of the loading force on the sample that generates a shear force at the interfacial plane.

6.2.2.2 Compression Test

Compression test was conducted on the AAM and control samples. The dimensions of the samples that were used for this test were Ø7.49 mm× 11.24 mm with a height to diameter ratio of 1.5 according to ASTM E9-09. Categories (C) and (D) had a 750-µm channel placed horizontally in the middle of the samples, as shown in Figure 6-5. A uniaxial testing machine (Instron-4206, MA, USA) and a crosshead speed of 1 mm min^{-1} were used to compress (crush) the samples.

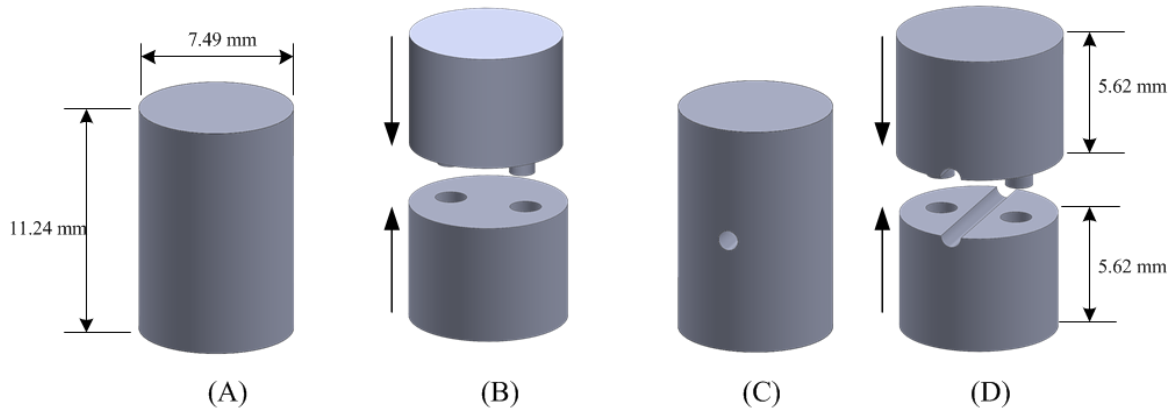

Figure 6-5 Schematic representation of the shear test samples: a) control sample printed entirely in one cycle of printing; B) AAM sample; C) control sample printed in one printing cycle with a horizontal channel; D) AAM sample with a horizontal channel.

6.2.2.3 Porosity Measurement

ASTM B311 and C373 require that porosity measurements are conducted using samples with weight larger than 1g. Therefore, the compression test samples, which had weights >1g, were used. Porosity of the structure was measured based on the Archimedes principle, using the Universal Specific Gravity Kit (Sartorius®, Bradford, MA, USA) and an electronic balance (APX-203, Denver Instruments,NY, USA) with a precision of 0.001g. The same procedure was used as the one previously reported by Basalah et al. [66].

6.2.2.4 Shrinkage Measurements

The dimensional precision of the manufactured bone implant is very important. In this study, an electronic Vernier caliper (Mitutoyo Corp., Kawasaki, Japan) with a precision of 0.01mm was used to measure the variation in the dimensions of the rounded bar samples (Ø7.49 mm × 11.24 mm), and the number of samples (n) was 6.

6.2.2.5 Visual Examination

A scanning electron microscope (SEM) (JEOL JSM-6460) was used to visually examine the adhesive bonded surface of the assembled parts before and after sintering and to observe the effect of sintering on the micro-structure of the fine particles.

6.2.2.6 Statistical Analysis

The analysis of variance (ANOVA) technique was used with the data that were obtained to determine whether there were significant differences between the groups. This significant difference was detected by alpha values of $p < 0.05$.

6.3. Results

6.3.1 Adhesive Bonding Shear Strength

Figure 6-6 shows the adhesive bonding strength for the two assembled parts produced by the AAM concept and the control samples. The diagram of Figure 6-6 compares the average shear strengths of (n = 9) samples in categories A, B, C and D. The results show a significant reduction in shear strength when the AAM process is used (category B), with a reduction in shear strength of approximately 25%. Similarly, when the horizontal channel is added to the structure, as in categories C and D, the shear result shows a reduction of approximately 32% in strength when applying the new concept, as in category D.

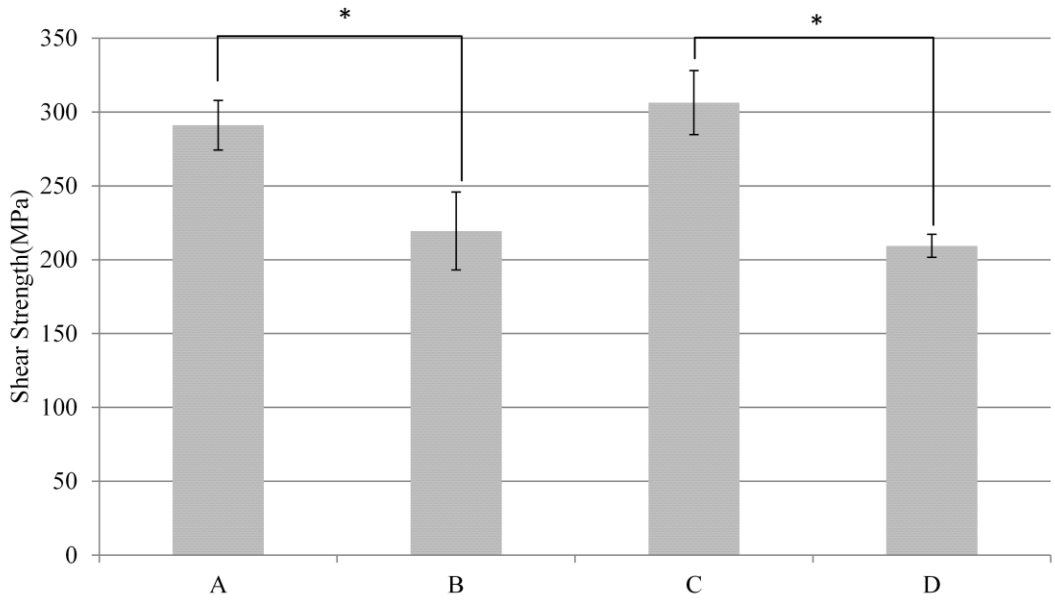

Figure 6-6 Results of shear strength tests of Ti samples in four categories: A) control sample without a channel; B) AAM-fabricated sample without a channel; C) control sample with a channel; D) AAM-fabricated sample with a channel.

6.3.2 Compressive Strength

Figure 6-7 shows the compressive strength of the AAM-made structures. The figure presents the average compressive strengths of (n = 6) samples from each category. The figure indicates that there are no significant differences among the results of the four categories. However, the variations in the margin of error in categories B and D, in which AAM is used, are greater than those in categories A and C, the control samples.

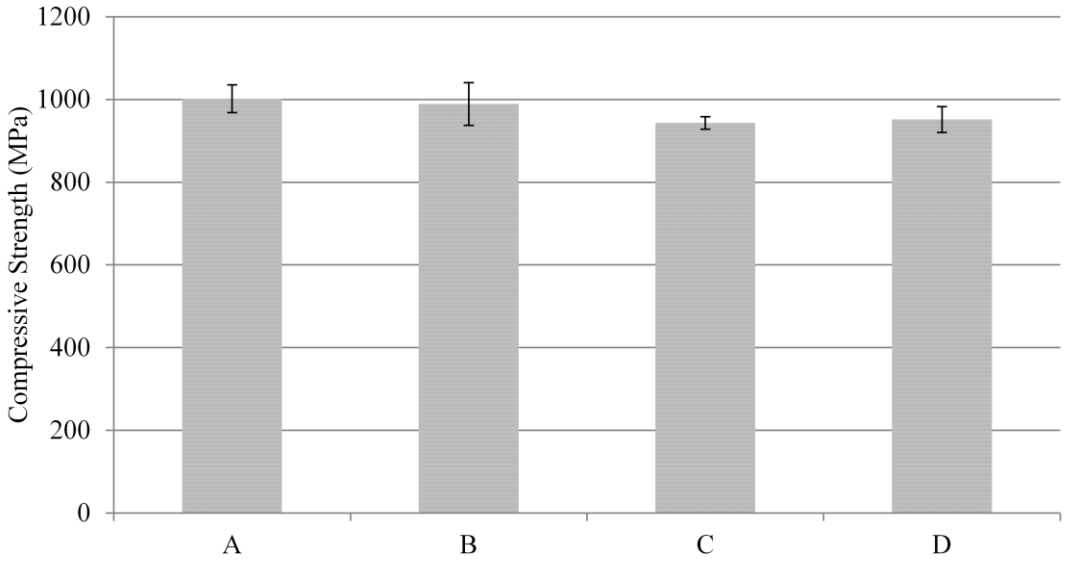

Figure 6-7 Compressive strength results of Ti samples of four categories: A) control sample without a channel; B) AAM-fabricated sample without a channel; C) control sample with a channel; D) AAM-fabricated sample with a channel.

6.3.3 Porosity

Figure 6-8 compares the results of porosity measurements for A and C samples with those of B and D samples (n = 6). The results show that there is a significant increase ($p < 0.05$) in the porosity of category B compared to the porosity of category A of approximately 2.2%. Also, there is a slight increase in the porosity of category D compared to the porosity of category C. The results of the porosity measurements in all cases varied between 12 and 16%.

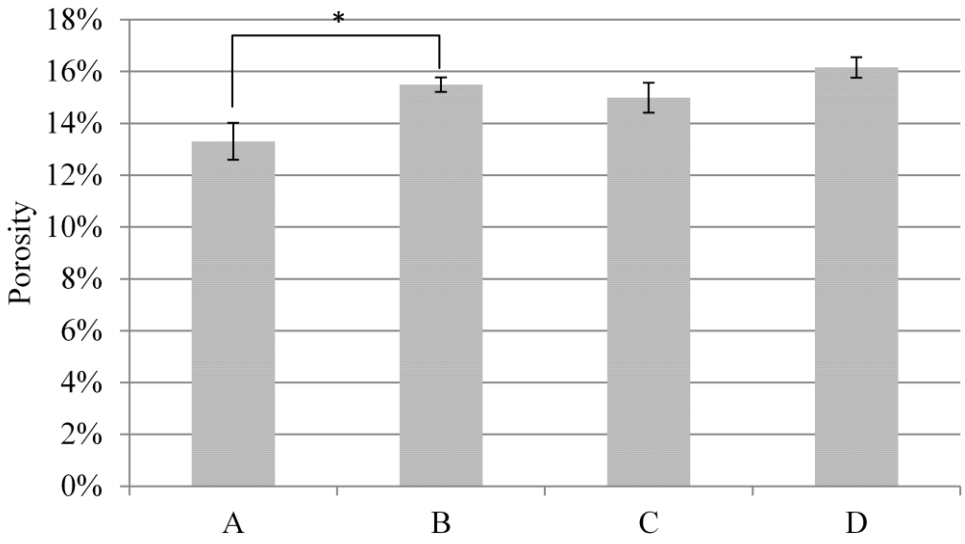

Figure 6-8 Results of porosity tests of the Ti samples for the four categories: A) control sample without a channel; B) AAM-fabricated sample without a channel; C) control sample with a channel; D) AAM-fabricated samples with a channel.

6.3.4 Shrinkage Measurements

Measurements of the average vertical and horizontal shrinkage were obtained from the samples before and after sintering. The reults of these measurements are shown in Figure 6-9. The data indicates that there are no significant differences between the horizontal and vertical shrinkages of categories A and C, the control samples. However, a significant increase ($p < 0.05$) is observed in the vertical shrinkage of the samples in categories B and D, the samples which were prepared using the AAM technique. The average shrinkage for all conditions and in both directions, i.e., horizontal and vertical, is ~12%.

6.4. Discussion

In this study, a new method is introduced for manufacturing of titanium based implants in an effort to resolve the depowdering issue that is inherent in powder-bed additive manufacturing techniques. In this new approach, a combination of additive manufacturing and traditional assembly, followed by sintering, is used to build the structure. Applying the shear test to validate this new technique of manufacturing is crucial to quantify the diffusional bonding between the two assembled parts in comparison with the one-part structure that is printed entirely in one cycle.

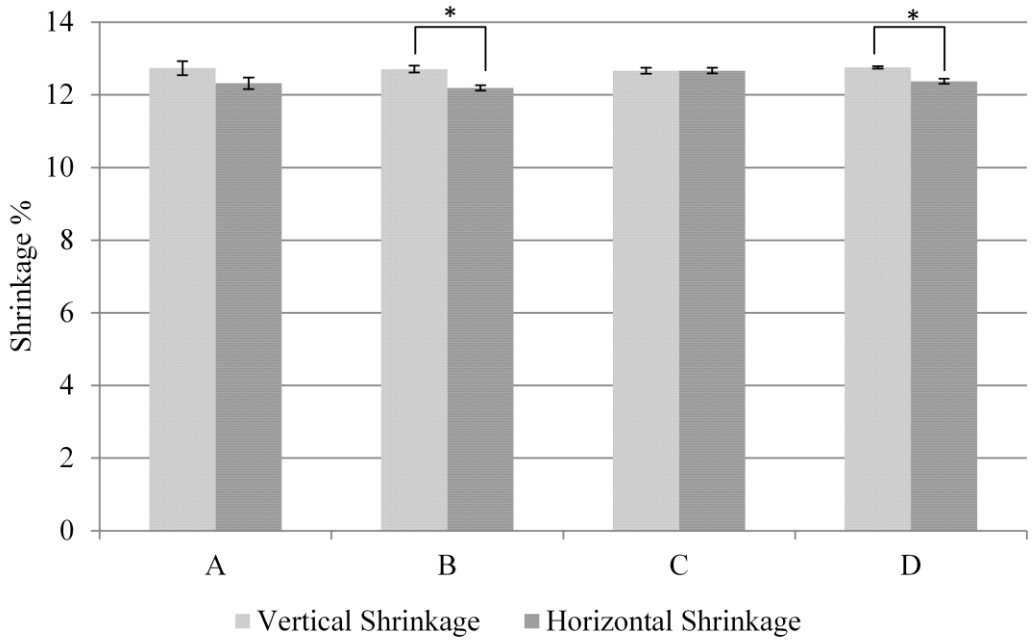

Figure 6-9 Vertical and horizontal shrinkages of the Ti samples in the four categories: A) control sample without a channel; B) AAM-fabricated sample without a channel; C) control sample with a channel; D) AAM-fabricated samples with a channel.

A close look at the attachment interface through the SEM images (Figure 6-10 and Figure 6-11) provides insight into the reason for the variation in the shear and shrinkage results among the different categories. Figure 6-10 shows that there are gaps at the interface of the two assembled parts in the case of samples (B) and (D). The gaps attributes to more shrinkage occurs in the vertical direction than in the horizontal direction, as Figure 6-9 suggests. A diffusional bonding occurs among the adjacent particles from each side of the attached parts. However, full bonding between the two parts does not consistently occur. The lack of such full bonding can (at least partially) explain the reduction in the shear strength of the AAM structures. It should, however, be noted that this reduction in strength is considered to be beneficial in the case of an orthopedic implant [66] because the reduced shear strength can help to avoid a mismatch in the strength between the bone and the implant. The minimum shear strength observed in this study is 200 MPa, and the cortical bone shear strength, according to Turner et al. [116], is ~51.6 MPa. However, other factors, such as sintering conditions and the size of the particles, could affect the reduction of the shear strength of the structure to provide a better match with the strength

of cortical bone. These factors mainly reduce the density of the structure, which leads to a reduction in the strength, as reported in the previous work [66].

In addition, the SEM image in Figure 6-12 shows that sintering is extensive, relative to the cases presented in reference [66], where only sinter necks were formed among Ti particles and the spherical shape of the particles was preserved. Comparison of the two cases indicates that the very small size of the particles used in the current work (i.e. diamters less than 38 μm, compared to 45-75 μm range) results in significant sintering progress. This is an important consideration because the diameter of the particles is an essential variable in all of the mass transport equations that address neck growth during sintering [50,117]. The level of sintering is a crucial factor in determining the level of porosity. In the present study, the porosity that is observed is in the same range as that of cortical bone, i.e. 3-12%, which is approximately 50% of the level observed in the previous work [66] (i.e. 31%). Comparing the porosity of the control to the AAM samples indicates that the increase in the porosity of the AAM samples is influenced by several factors including the availability of the guiders inside the structure, the voids surrounding the guiders, and the precision of the human hand in applying the desired amount of pressure, when both parts are stacked together.

From the manufacturing point of view, it is preferable for the shrinkage caused by sintering to be minimal and isotropic. In this study, the shrinkage in all sintered samples is relatively moderate due to the used fine particles. Furthermore, the inconsistant shrinkage occuring in the AAM samples could be reduced or prevented by choosing different compensation factors for each direction in the CAD model. Conversely, the compressive strength is not affected by stacking the parts, since the force that is applied axially is perpendicular to the plane of the stacked layers.

As evident in this study, this new method of manufacturing is feasible with a slight sacrifice in terms of the shear strength of the structure. According to Butscher et al. [15], the precision of the powder-bed 3DP machine is 350-500 μm. However, in the screening phase of this study, the minimum thickness of a sheet of Ti that could be printed and handled was 250 μm, and as many laminated sheets of this size as required could be assembled to form a complex-shaped structure with conformal channels. The use of AAM may establish a new era of economical manufacturing, in which extremely

complex structures composed of many layers including complex channel networks could be fabricated.

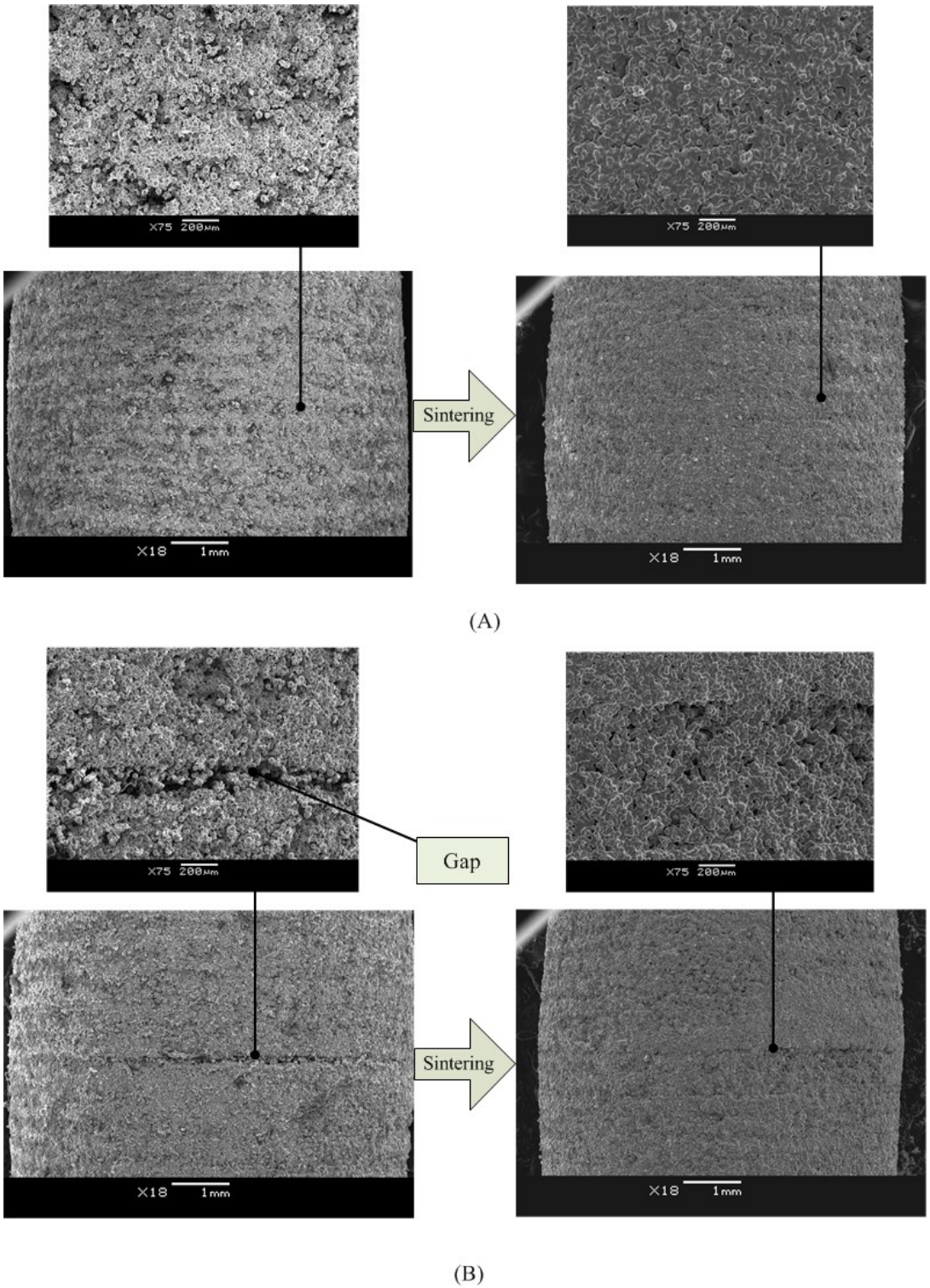

Figure 6-10 SEM images of samples before (green parts) and after sintering of: A) control sample without a channel; B) AAM-fabricated sample without a channel.

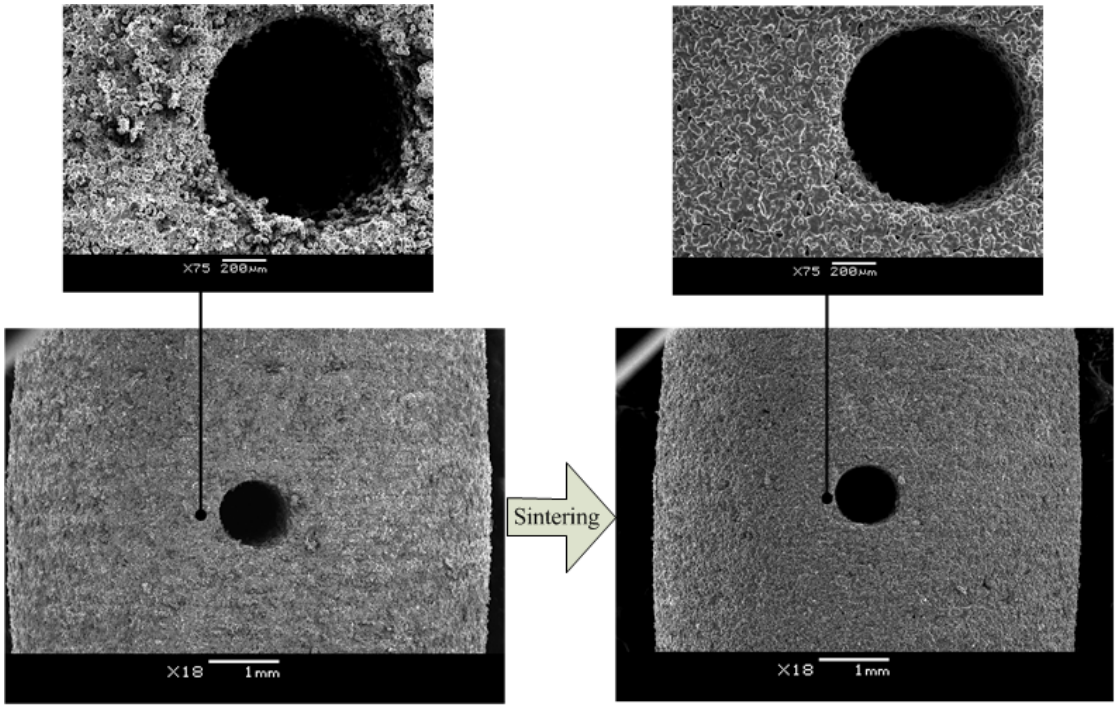

(C)

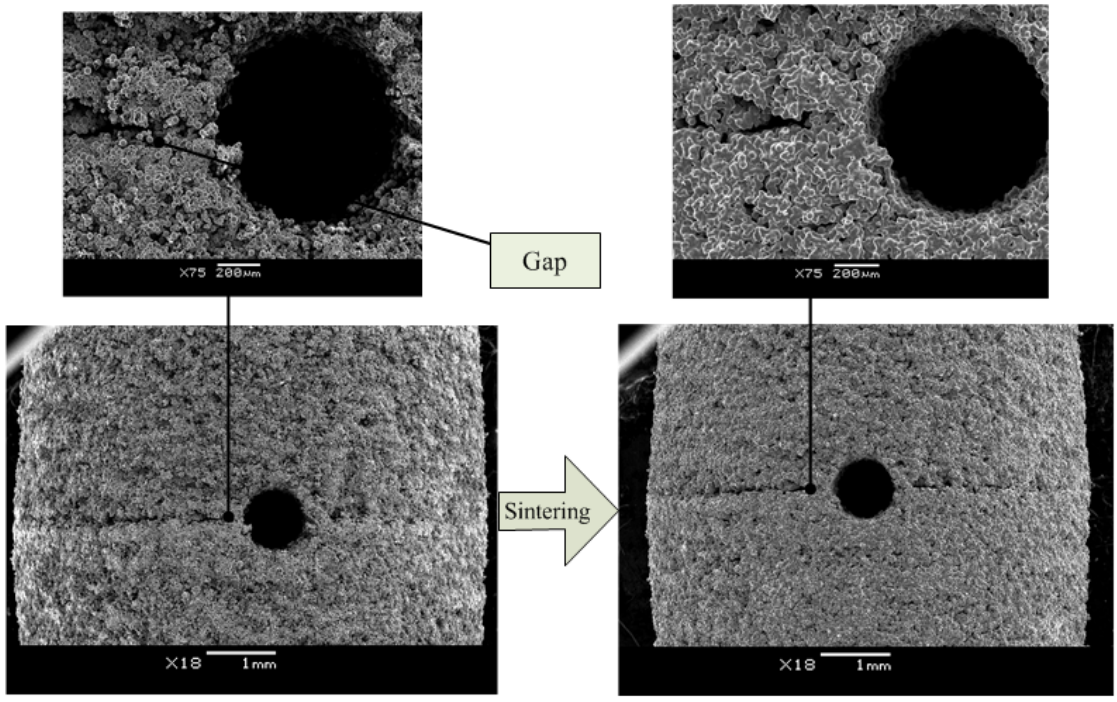

(D)

Figure 6-11 SEM images of samples before (green parts) and after sintering of: C) control sample with a channel; D) AAM-fabricated sample with a channel.

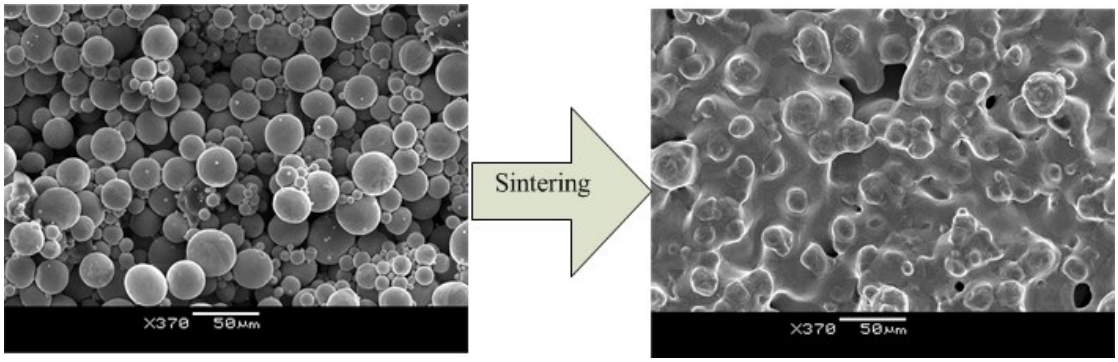

Figure 6-12 Shape of Ti particles before and after the sintering process.

6.5. Summary

In this study, we developed a new technique for manufacturing titanium bone implants. The fabricated parts that made by stacking the additive manufactured segments of a part followed by sintering was validated using various characterization techniques. The experimental results indicated that this manufacturing technique has the potential to produce a structure with macro-sized channels with a reduction in shear strength of 24-30% compared to control samples. This technique did not affect compressive strength. However, there was a relatively low increase in porosity of approximately 1.17-2.2% in the AAM samples, with the total porosity falling in the range of 12-16%, which is comparable to the porosity of cortical bone. Also, a slight increase in the vertical shrinkage of ~ 0.4-0.5% was observed compared to horizontal shrinkage due to the use of this new technique.

Chapter 7 Conclusions and Future Work

7.1 Conclusions

The following conclusions can be drawn from this thesis:

- A powder based ink-jet printer was effectively used to print a porous Ti construct with a highly complex external and internal geometry.
- The minimum amount of PVA in the powder mixture was determined to be no less than 3%. Increasing the PVA content could play a role of the space-holder and increase the porosity of the structure.
- It was found that the porosity contributes significantly to the strength of the structure and can be controlled through different processing parameters such as binder contents, the particle's shape, and the powder's level of compaction.
- The compressive strength of the porous Ti structure varied according to the processing parameters. Some categories of powder failed at a very high value ~ 1000 MPa which could be attributed to the microdamage among the sinter necks of the particles that occurred at the large plastic region (yield plateau). Thus, the compressive strength is not an effective measure compared to yield strength in characterizing and comparing the strength of the porous structure to the bone properties. Overall, the compressive strength ranged from 56-1000 MPa and the yield strength ranged from 27-383 MPa in the produced samples.
- Characterizing the stiffness of the structure was achieved by obtaining the Young's modulus value. The achieved Young's modulus was comparable to the bone modulus and ranged from 0.77-11.46 GPa.

- The level of shrinkage that was achieved using the powder based ink-jet printer was lower than what has been achieved by using additive manufacturing counterparts and using the spherical powder, particularly, with a limited particles range contributed significantly in lowering the level of shrinkage. The achieved levels of shrinkage ranged from 1.5-12%.
- The isotropic shrinkage in the structure is very important. Thus, it was found that manipulating the architecture of the structure by adding horizontal channels assisted in producing isotropic shrinkage. The level of compaction also helps in this regard.
- The assembled additive manufacturing (AAM) technique was developed. This novel method has high potential to create a complex network of conformal encapsulated macro-sized channels in the structure.
- The developed model which predicts the porosity based on the sinter neck was validated by the experimental data. The results indicate a good match between the experimental result and the model.

7.2 Recommendations and Future Work

7.2.1 Manufacturing

-In our commercial printer there is a limitation in manipulating two crucial printing parameters, i.e. the linear speed of the gantry system and the rotational speed of the counter rotating roller which are responsible about the process of spreading powder. These parameters could potentially influence the printing quality.

- The assembled additive manufacturing (AAM) concept opens the possibility for developing a highly complex structure with a sophisticated conformal channel by assembling a large number of layers.

- The main purpose of using the PVA during the printing process is to form the green samples. The existence of the PVA in the printed samples increases the heterogeneity and the porosity of the structure. Thus, it would be beneficial to dispense the PVA during the printing process. This could be achieved by increasing the binding agent in the injected liquid binder. Any modification to this binder will cause the thermal actuator of the

printhead to overheat. Therefore, using a different printhead such as a micro piezoelectric printhead which is principally works based on a vibrator actuator instead of the thermal actuator will solve this problem.

7.2.2 Material Processing

- It was found that sintering was effective at 1400º C. Sintering at 1300 º C has not been a part of my thesis. Future work should extensively investigate the range of effective sintering starting from 1300 º C. This study was limited by the furnace not heating above 1400 º C to preserve the heating elements of the furnace.
- It seems that a discoloring on the top surface of the samples which is mainly comprised of carbon was most likely left by one of two sources: the residue of the debinding process or the contents of the flowing Argon gas. According to German [118], Ti could react with the carbon and form TiC. This discolouring could be alleviated by installing a vent at the inlet of the tube furnace to properly suction the residue of the debinding process. Alternatively, placing the samples in a crucible covered by a lid would avoid direct contact between the flowing gas and the samples.

7.2.3 Modelling

- In this study, a model was developed to predict the porosity in the structure based on the sinter necks progression among the particles. This model could be linked to the sinter neck growth equations which include several material processing parameters related to particle size, sintering temperature, and sintering duration.
- Starting from the cubical unit cell proposed in this study, an analytical model could be developed to address the force which is applied to the unit cell and then reflected onto the entire structure to predict the strength and the stiffness of the structure accordingly.

7.2.4 Biological Study

-Further investigation is required to assess cells behavior within the microstructure of the porous Ti samples. Also the influence of channels number and orientation on the cell proliferation requires a deep investigation.

- The mineralization need to be measured to assess the formation of the hydroxyapatite in the culture.

Appendices

Appendix A

Cell culturing conducted on some samples of chapter 5 at The University of Manchester by Prof. Julie Gough and Louise Carney, two groups of samples; the first group cultured for one day, and the second group for three days. The SEM images (Fig. A-1) and (Fig. A-2) shows the osteoblast spreaded and attached to the porous structure. Also, the cells are bridging and filling the gap of the pores.

Figure A-1: Samples were cultured with an osteoblast for 1day.

Figure A-2: Samples were cultured with an osteoblast for 3 days.

Appendix B

In vitro cell culturing results of four different categories of samples used in chapter 5 with different channels orientations conducted by Prof. Julie Gough and Louise Carney.

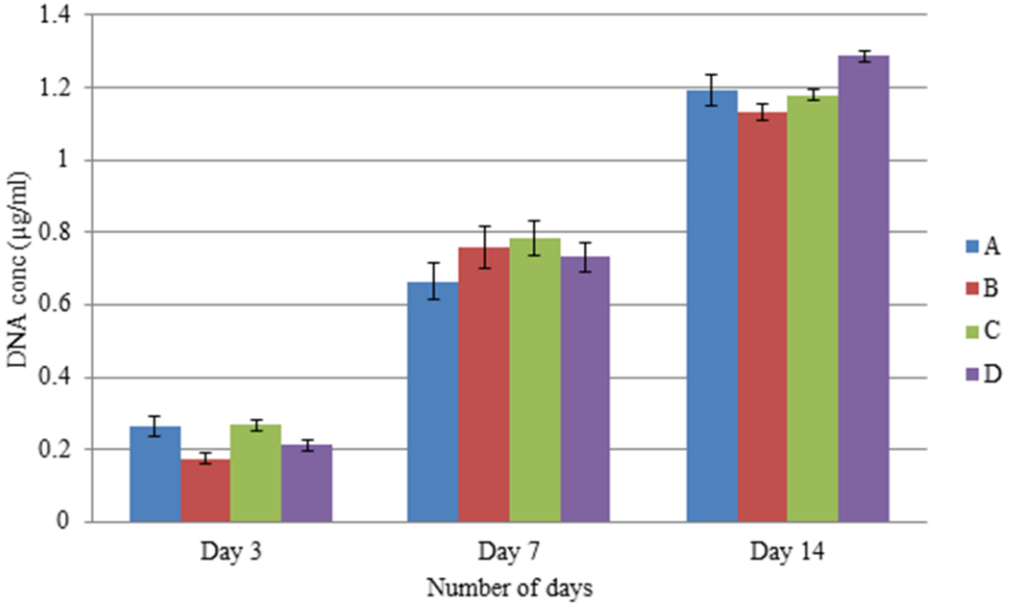

Figure B-1 DNA Content (picogreen assay) shows the influence of the channel orientation on cell density, there is a steady increase in the cell numbers with the time.

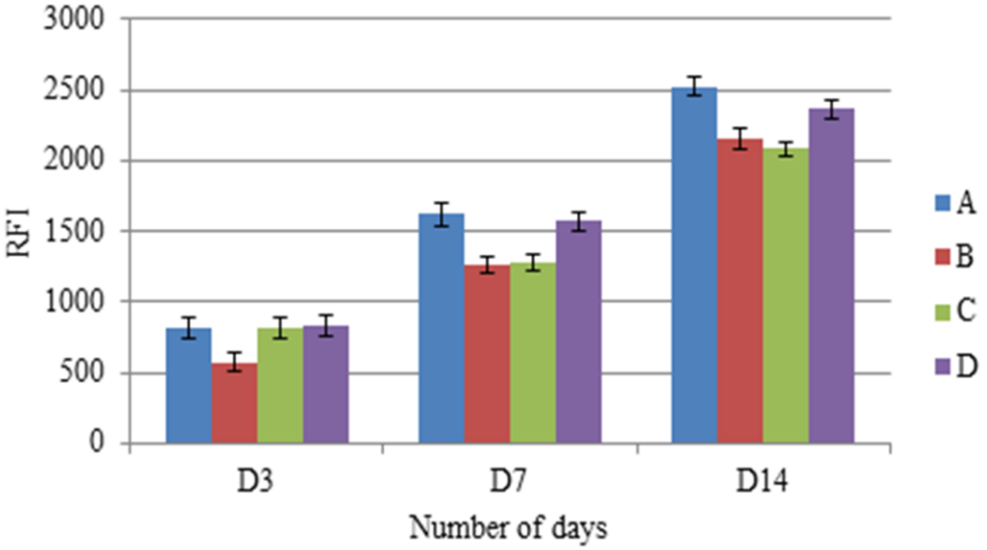

Figure B-2 Raw alamar blue data shows the metabolic activity at days 3, 7 and 14 of samples from four different categories.

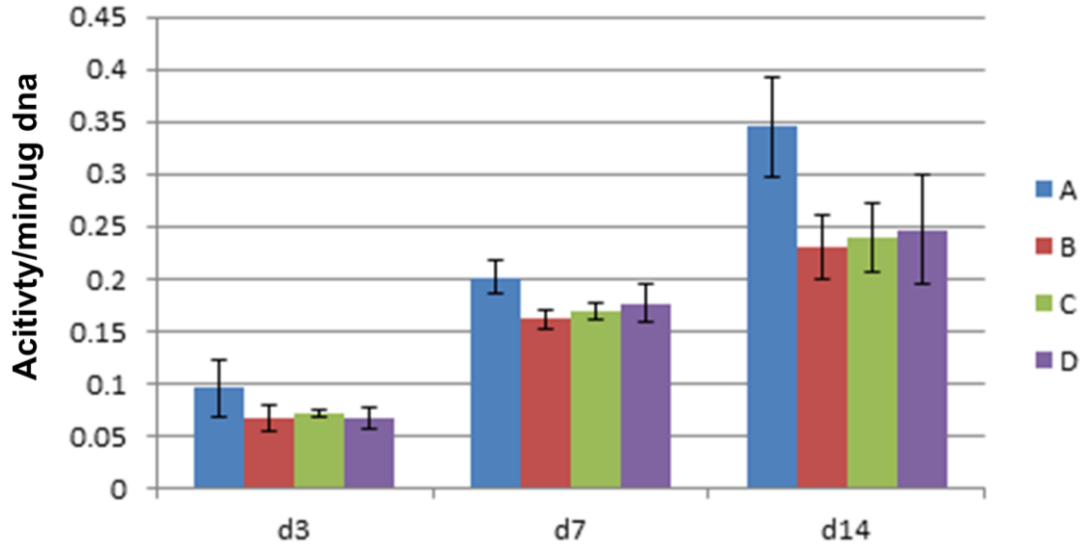

Figure B-3 Channels orientation influence on Alkaline Phosphate activity at days 3, 7 and 14.

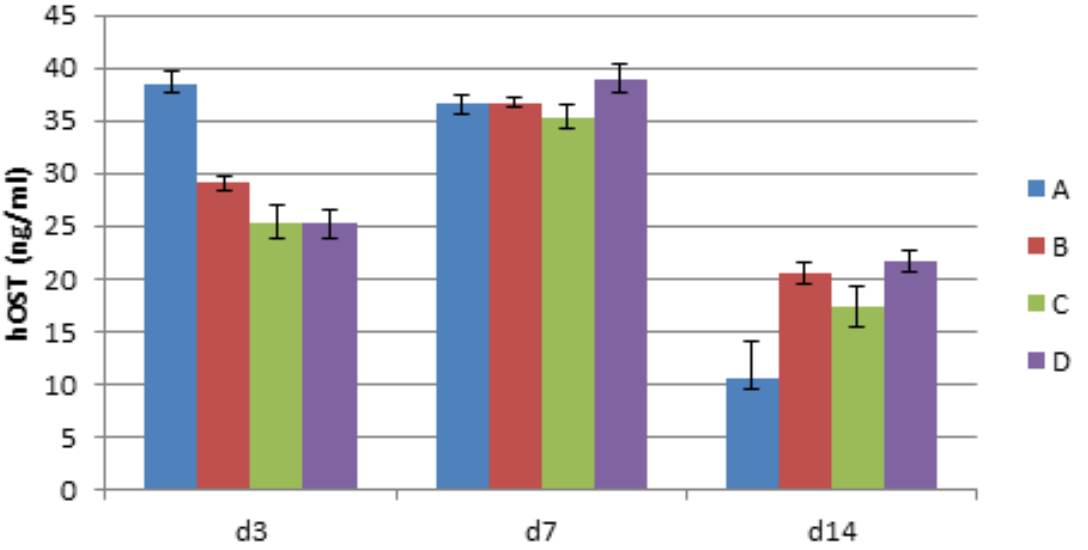

Figure B-4 Channels orientaion Influence on osteocalcin production at days 3, 7 and 14.

Appendix D

Matlab code for the develped model in Chapter 4 which correlate between the porosity and the sinter neck among the particles:

```
prompt = 'What is the mean diameter of the particles? ';
D = input(prompt);% The user input the mean particle
diameter
prompt1= 'What is the sinter neck ratio';
XD=input(prompt1);%The user input the sinter neck ratio
X=XD*D;
r=D/2;
a=X/2;
h=r-sqrt((r^2)-(a^2));
V=(((pi*((1/6)*r^3))));
f=((1/4)*pi*(h^2)*((3*r)-h));
vf=V-f;
vff=vf;
OT=(r-h)^3;
vfff=vff/OT;
Porosity=(1-vfff)*100
```

Appendix E

Copyright Clearance Center RightsLink®

Home | Account Info | Help

Title: Characterizations of additive manufactured porous titanium implants
Author: Ahmad Basalah,Yaser Shanjani,Shahrzad Esmaeili,Ehsan Toyserkani
Publication: Journal of Biomedical Materials Research
Publisher: John Wiley and Sons
Date: Aug 1, 2012

Logged in as:
Ahmad Basalah
LOGOUT

Order Completed

Thank you for your order.

This Agreement between Ahmad Basalah ("You") and John Wiley and Sons ("John Wiley and Sons") consists of your license details and the terms and conditions provided by John Wiley and Sons and Copyright Clearance Center.

Your confirmation email will contain your order number for future reference.

Get the printable license.

License Number	3618951420676
License date	Apr 30, 2015
Licensed Content Publisher	John Wiley and Sons
Licensed Content Publication	Journal of Biomedical Materials Research
Licensed Content Title	Characterizations of additive manufactured porous titanium implants
Licensed Content Author	Ahmad Basalah,Yaser Shanjani,Shahrzad Esmaeili,Ehsan Toyserkani
Licensed Content Date	Aug 1, 2012
Licensed Content Pages	10
Type of use	Dissertation/Thesis
Requestor type	Author of this Wiley article
Format	Print and electronic
Portion	Full article
Will you be translating?	No
Title of your thesis / dissertation	Additive Manufacturing of Porous Titanium Structures for Use in Orthopaedic Implants
Expected completion date	Jun 2015
Expected size (number of pages)	130
Requestor Location	Ahmad Basalah 206-350 Columbia Street West Waterloo, ON N2L 6P6 Canada Attn: Ahmad Basalah
Billing Type	Invoice
Billing address	Ahmad Basalah 206-350 Columbia Street West Waterloo, ON N2L 6P6 Canada Attn: Ahmad Basalah
Total	0.00 USD

ORDER MORE | CLOSE WINDOW

Appendix F

ELSEVIER LICENSE
TERMS AND CONDITIONS

Jul 22, 2015

This is a License Agreement between Ahmad Basalah ("You") and Elsevier ("Elsevier") provided by Copyright Clearance Center ("CCC"). The license consists of your order details, the terms and conditions provided by Elsevier, and the payment terms and conditions.

All payments must be made in full to CCC. For payment instructions, please see information listed at the bottom of this form.

Supplier	Elsevier Limited The Boulevard,Langford Lane Kidlington,Oxford,OX5 1GB,UK
Registered Company Number	1982084
Customer name	Ahmad Basalah
Customer address	206-350 Columbia Street West Waterloo, ON N2L 6P6
License number	3638311376381
License date	May 29, 2015
Licensed content publisher	Elsevier
Licensed content publication	Elsevier Books
Licensed content title	3D Bioprinting and Nanotechnology in Tissue Engineering and Regenerative Medicine
Licensed content author	None
Licensed content date	2015
Number of pages	33
Start Page	231
End Page	263
Type of Use	reuse in a thesis/dissertation
Intended publisher of new work	other
Portion	full chapter
Format	both print and electronic
Are you the author of this Elsevier chapter?	Yes
How many pages did you author in this Elsevier book?	32
Will you be translating?	No
Title of your thesis/dissertation	Additive Manufacturing of Porous Titanium Structures for Use in Orthopaedic Implants
Expected completion date	Jun 2015
Estimated size (number of pages)	
Elsevier VAT number	GB 494 6272 12

References:

1. Bombardier, C, Hawker, G, & Mosher D. the Impact of Arthritis in Canada : Today and Over the Next 30 Years. *Arthritis Alliance of Canada* 2011. Available at: http://www.arthritisalliance.ca/images/PDF/eng/Initiatives/20111022_2200_impact_of_arthritis.pdf.

2. Public Health Agency of Canada. *Life with Arthritis in Canada: A Personal and Public Health Challenge.*; 2010. Available at: http://www.phac-aspc.gc.ca/cd-mc/arthritis-arthrite/lwaic-vaaac-10/pdf/arthritis-2010-eng.pdf.

3. Macdonald K V, Sanmartin C, Langlois K, Marshall DA. Symptom onset, diagnosis and management of osteoarthritis. *Stat. Canada* 2014;25(9):10-17.

4. Canadian Institute for Health Information. Hip and Knee Replacements in Canada: Canadian Joint Replacement Registry 2014 Annual Report. 2014;(June).

5. Sundfeldt M, Carlsson L V, Johansson CB, Thomsen P, Gretzer C. Aseptic loosening, not only a question of wear: a review of different theories. *Acta Orthop.* 2006;77(2):177-197. doi:10.1080/17453670610045902.

6. Wiria FE, Maleksaeedi S, He Z. Manufacturing and characterization of porous titanium components. *Prog. Cryst. Growth Charact. Mater.* 2014. doi:10.1016/j.pcrysgrow.2014.09.001.

7. Hutchinson MR. The Burden of Musculoskeletal Diseases in the United States: Prevalance, Societal and Economic Cost, 1st Edition. *J. Am. Coll. Surg.* 2009;208(1):e5-e6. doi:10.1016/j.jamcollsurg.2008.06.146.

8. Canadian Institute for Health Information. Hip and Knee Replacements in Canada : Canadian Joint Replacement Registry 2013 Annual Report. 2013:1-94.

9. Gikas PD, Bayliss L, Bentley G, Briggs TWR. An overview of autologous chondrocyte implantation. *J. Bone Joint Surg. Br.* 2009;91(8):997-1006. doi:10.1302/0301-620X.91B8.21824.

10. Bartel DL, Davy DT, Keaveny TM. Orthopaedic Biomechanics: Mechanics and Design in Musculoskeletal Systems. 2006.

11. Koh JL, Wirsing K, Lautenschlager E, Zhang L-O. The effect of graft height mismatch on contact pressure following osteochondral grafting: a biomechanical study. *Am. J. Sports Med.* 2004;32(2):317-320. doi:10.1177/0363546503261730.

12. Vasiliadis HS, Wasiak J, Salanti G. Autologous chondrocyte implantation for the treatment of cartilage lesions of the knee: A systematic review of randomized studies. *Knee Surgery, Sport. Traumatol. Arthrosc.* 2010;18(12):1645-1655. doi:10.1007/s00167-010-1050-3.

13. Hutmacher DW. Scaffolds in tissue engineering bone and cartilage. *Biomaterials* 2000;21(24):2529-2543. doi:10.1016/S0142-9612(00)00121-6.

14. Bohner M, Loosli Y, Baroud G, Lacroix D. Commentary: Deciphering the link between architecture and biological response of a bone graft substitute. *Acta Biomater.* 2011;7(2):478-84. doi:10.1016/j.actbio.2010.08.008.

15. Butscher A, Bohner M, Hofmann S, Gauckler L, Müller R. Structural and material approaches to bone tissue engineering in powder-based three-dimensional printing. *Acta Biomater.* 2011;7(3):907-20. doi:10.1016/j.actbio.2010.09.039.

16. Porter JR, Ruckh TT, Popat KC. Bone tissue engineering: A review in bone biomimetics and drug delivery strategies. *Biotechnol. Prog.* 2009;25(6):1539-1560. doi:10.1002/btpr.246.

17. Szpalski C, Wetterau M, Barr J, Warren SM. Bone Tissue Engineering: Current Strategies and Techniques—Part I: Scaffolds. *Tissue Eng. Part B Rev.* 2012;18(4):246-257. doi:10.1089/ten.teb.2011.0427.

18. Bose S, Tarafder S. Calcium phosphate ceramic systems in growth factor and drug delivery for bone tissue engineering: a review. *Acta Biomater.* 2012;8(4):1401-21. doi:10.1016/j.actbio.2011.11.017.

19. Pilliar R., Filiaggi M., Wells J., Grynpas M., Kandel R. Porous calcium polyphosphate scaffolds for bone substitute applications — in vitro characterization. *Biomaterials* 2001;22(9):963-972. doi:10.1016/S0142-9612(00)00261-1.

20. Leong KF, Cheah CM, Chua CK. Solid freeform fabrication of three-dimensional scaffolds for engineering replacement tissues and organs. *Biomaterials* 2003;24(13):2363-2378. doi:10.1016/S0142-9612(03)00030-9.

21. Yang S, Leong KF, Du Z, Chua CK. The design of scaffolds for use in tissue engineering. Part I. Traditional factors. *Tissue Eng.* 2001;7(6):679-689. doi:10.1089/107632701753337645.

22. Karageorgiou V, Kaplan D. Porosity of 3D biomaterial scaffolds and osteogenesis. *Biomaterials* 2005;26(27):5474-91. doi:10.1016/j.biomaterials.2005.02.002.

23. Frost HM. Bone's mechanostat: a 2003 update. *Anat. Rec. A. Discov. Mol. Cell. Evol. Biol.* 2003;275(2):1081-1101. doi:10.1002/ar.a.10119.

24. Mehrali M, Shirazi FS, Mehrali M, Metselaar HSC, Kadri NA Bin, Osman NAA. Dental implants from functionally graded materials. *J. Biomed. Mater. Res. - Part A* 2013;101(10):3046-3057. doi:10.1002/jbm.a.34588.

25. Chang BS, Lee CK, Hong KS, et al. Osteoconduction at porous hydroxyapatite with various pore configurations. *Biomaterials* 2000;21(12):1291-8. Available at: http://www.ncbi.nlm.nih.gov/pubmed/23732684.

26. Kujala S, Ryhänen J, Danilov A, Tuukkanen J. Effect of porosity on the osteointegration and bone ingrowth of a weight-bearing nickel–titanium bone graft substitute. *Biomaterials* 2003;24(25):4691-4697. doi:10.1016/S0142-9612(03)00359-4.

27. Lin CY, Kikuchi N, Hollister SJ. A novel method for biomaterial scaffold internal architecture design to match bone elastic properties with desired porosity. *J. Biomech.* 2004;37(5):623-36. doi:10.1016/j.jbiomech.2003.09.029.

28. Cai S, Xi J. A control approach for pore size distribution in the bone scaffold based on the hexahedral mesh refinement. *Comput. Des.* 2008;40(10-11):1040-1050. doi:10.1016/j.cad.2008.09.004.

29. Sanz-Herrera J a, García-Aznar JM, Doblaré M. A mathematical approach to bone tissue engineering. *Philos. Trans. A. Math. Phys. Eng. Sci.* 2009;367(1895):2055-2078. doi:10.1098/rsta.2009.0055.

30. Hollister SJ. Porous scaffold design for tissue engineering. *Nat. Mater.* 2005;4(7):518-24. doi:10.1038/nmat1421.

31. Yarlagadda PKD V, Chandrasekharan M, Shyan JYM. Recent advances and current developments in tissue scaffolding. *Biomed. Mater. Eng.* 2005;15(3):159-77. Available at: http://www.ncbi.nlm.nih.gov/pubmed/15911997.

32. Stevens B, Yang Y, Mohandas A, Stucker B, Nguyen KT. A review of materials, fabrication methods, and strategies used to enhance bone regeneration in engineered bone tissues. *J. Biomed. Mater. Res. B. Appl. Biomater.* 2008;85(2):573-82. doi:10.1002/jbm.b.30962.

33. Navarro M, Michiardi A, Castaño O, Planell JA. Biomaterials in orthopaedics. *J. R. Soc. Interface* 2008;5(27):1137-58. doi:10.1098/rsif.2008.0151.

34. Long M, Rack HJ. Titanium alloys in total joint replacement--a materials science perspective. *Biomaterials* 1998;19(18):1621-39. Available at: http://www.ncbi.nlm.nih.gov/pubmed/9839998.

35. Dabrowski B, Swieszkowski W, Godlinski D, Kurzydlowski KJ. Highly porous titanium scaffolds for orthopaedic applications. *J. Biomed. Mater. Res. B. Appl. Biomater.* 2010;95(1):53-61. doi:10.1002/jbm.b.31682.

36. Navarro M, Michiardi a, Castaño O, Planell J a. Biomaterials in orthopaedics. *J. R. Soc. Interface* 2008;5(27):1137-58. doi:10.1098/rsif.2008.0151.

37. Krishna BV, Bose S, Bandyopadhyay A. Low stiffness porous Ti structures for load-bearing implants. *Acta Biomater.* 2007;3(6):997-1006. doi:10.1016/j.actbio.2007.03.008.

38. Reclaru L, Eschler P-Y, Lerf R, Blatter A. Electrochemical corrosion and metal ion release from Co-Cr-Mo prosthesis with titanium plasma spray coating. *Biomaterials* 2005;26(23):4747-56. doi:10.1016/j.biomaterials.2005.01.004.

39. Billi F, Campbell P. Nanotoxicology of metal wear particles in total joint arthroplasty: a review of current concepts. *J. Appl. Biomater. Biomech.* (Vol 8 issue 1 (January-April 2010)):1-6. Available at: http://www.jab-fm.com/article/nanotoxicology-of-metal-wear-particles-in-total-joint--arthroplasty--a-review-of-current-concepts-art006572. Accessed May 15, 2014.

40. Shishkovsky I V., Volova LT, Kuznetsov M V., Morozov YG, Parkin IP. Porous biocompatible implants and tissue scaffolds synthesized by selective laser sintering from Ti and NiTi. *J. Mater. Chem.* 2008;18(12):1309. doi:10.1039/b715313a.

41. Michiardi A, Aparicio C, Planell J a, Gil FJ. New oxidation treatment of NiTi shape memory alloys to obtain Ni-free surfaces and to improve biocompatibility. *J. Biomed. Mater. Res. B. Appl. Biomater.* 2006;77(2):249-56. doi:10.1002/jbm.b.30441.

42. Wataha JC, Dell NLO, Singh BB, Ghazi M, Whitford GM, Lockwood PE. Relating Nickel-Induced Tissue Inflammation to Nickel Release in vivo. 2001:537-544. doi:10.1002/jbm.xxxx.

43. Staiger MP, Pietak AM, Huadmai J, Dias G. Magnesium and its alloys as orthopedic biomaterials: a review. *Biomaterials* 2006;27(9):1728-34. doi:10.1016/j.biomaterials.2005.10.003.

44. Alvarez K, Nakajima H. Metallic Scaffolds for Bone Regeneration. *Materials (Basel).* 2009;2(3):790-832. doi:10.3390/ma2030790.

45. Frosch K-H, Stürmer KM. Metallic Biomaterials in Skeletal Repair. *Eur. J. Trauma* 2006;32(2):149-159. doi:10.1007/s00068-006-6041-1.

46. Ryan G, Pandit A, Apatsidis DP. Fabrication methods of porous metals for use in orthopaedic applications. *Biomaterials* 2006;27(13):2651-70. doi:10.1016/j.biomaterials.2005.12.002.

47. Okazaki Y. A New Ti–15Zr–4Nb–4Ta alloy for medical applications. *Curr. Opin. Solid State Mater. Sci.* 2001;5(1):45-53. doi:10.1016/S1359-0286(00)00025-5.

48. Matassi F, Botti A, Sirleo L, Carulli C, Innocenti M. Porous metal for orthopedics implants. *Clin. Cases Miner. Bone Metab.* 2013;10(2):111-115. Available at: http://www.pubmedcentral.nih.gov/articlerender.fcgi?artid=3796997&tool=pmcentrez&rendertype=abstract. Accessed May 5, 2014.

49. Balla VK, Bodhak S, Bose S, Bandyopadhyay A. Porous tantalum structures for bone implants: fabrication, mechanical and in vitro biological properties. *Acta Biomater.* 2010;6(8):3349-59. doi:10.1016/j.actbio.2010.01.046.

50. Oh I-H, Nomura N, Masahashi N, Hanada S. Mechanical properties of porous titanium compacts prepared by powder sintering. *Scr. Mater.* 2003;49(12):1197-1202. doi:10.1016/j.scriptamat.2003.08.018.

51. Weber JN, White EW. Carbon-metal graded composites for permanent osseous attachment of non-porous metals. *Mater. Res. Bull.* 1972;7(9):1005-1016. doi:10.1016/0025-5408(72)90092-X.

52. Ryan GE, Pandit AS, Apatsidis DP. Porous titanium scaffolds fabricated using a rapid prototyping and powder metallurgy technique. *Biomaterials* 2008;29(27):3625-35. doi:10.1016/j.biomaterials.2008.05.032.

53. Murr LE, Esquivel EV, Quinones S a., et al. Microstructures and mechanical properties of electron beam-rapid manufactured Ti–6Al–4V biomedical prototypes compared to wrought Ti–6Al–4V. *Mater. Charact.* 2009;60(2):96-105. doi:10.1016/j.matchar.2008.07.006.

54. Mullen L, Stamp RC, Brooks WK, Jones E, Sutcliffe CJ. Selective Laser Melting: a regular unit cell approach for the manufacture of porous, titanium, bone in-growth constructs, suitable for orthopedic applications. *J. Biomed. Mater. Res. B. Appl. Biomater.* 2009;89(2):325-34. doi:10.1002/jbm.b.31219.

55. Dinda GP, Song L, Mazumder J. Fabrication of Ti-6Al-4V Scaffolds by Direct Metal Deposition. *Metall. Mater. Trans. A* 2008;39(12):2914-2922. doi:10.1007/s11661-008-9634-y.

56. Campanelli SL, Contuzzi N, Angelastro A, Ludovico AD. Capabilities and Performances of the Selective Laser Melting Process. 1994.

57. Wong K V., Hernandez A. A Review of Additive Manufacturing. *ISRN Mech. Eng.* 2012;2012:1-10. doi:10.5402/2012/208760.

58. Woesz A. Rapid Prototyping to Produce POROUS SCAFFOLDS WITH CONTROLLED ARCHITECTURE for Possible use in Bone Tissue Engineering. In: Bidanda B, Bártolo P, eds. *Virtual Prototyping & Bio Manufacturing in Medical Applications*. Springer US; 2008:171-206. doi:10.1007/978-0-387-68831-2_9.

59. Van Noort R. The future of dental devices is digital. *Dent. Mater.* 2012;28(1):3-12. doi:10.1016/j.dental.2011.10.014.

60. Wen CE, Yamada Y, Shimojima K, Chino Y, Hosokawa H, Mabuchi M. Novel titanium foam for bone tissue engineering. 2002;(July):22-25.

61. Pupo Y, Delgado J, Serenó L, Ciurana J. Scanning Space Analysis in Selective Laser Melting for CoCrMo Powder. *Procedia Eng.* 2013;63:370-378. doi:10.1016/j.proeng.2013.08.228.

62. Murr LE, Gaytan SM, Ramirez DA, et al. Metal Fabrication by Additive Manufacturing Using Laser and Electron Beam Melting Technologies. *J. Mater. Sci. Technol.* 2012;28(1):1-14. doi:10.1016/S1005-0302(12)60016-4.

63. Lin JG, Li YC, Wong CS, Hodgson PD, Wen CE. Degradation of the strength of porous titanium after alkali and heat treatment. *J. Alloys Compd.* 2009;485(1-2):316-319. doi:10.1016/j.jallcom.2009.05.048.

64. Li JP, Habibovic P, van den Doel M, et al. Bone ingrowth in porous titanium implants produced by 3D fiber deposition. *Biomaterials* 2007;28(18):2810-20. doi:10.1016/j.biomaterials.2007.02.020.

65. Li JP, de Wijn JR, van Blitterswijk C a, de Groot K. Porous Ti6Al4V scaffolds directly fabricated by 3D fibre deposition technique: effect of nozzle diameter. *J. Mater. Sci. Mater. Med.* 2005;16(12):1159-63. doi:10.1007/s10856-005-4723-6.

66. Basalah A, Shanjani Y, Esmaeili S, Toyserkani E. Characterizations of additive manufactured porous titanium implants. *J. Biomed. Mater. Res. B. Appl. Biomater.* 2012;100(7):1970-9. doi:10.1002/jbm.b.32764.

67. Curodeau a, Sachs E, Caldarise S. Design and fabrication of cast orthopedic implants with freeform surface textures from 3-D printed ceramic shell. *J. Biomed. Mater. Res.* 2000;53(5):525-35. Available at: http://www.ncbi.nlm.nih.gov/pubmed/10984701.

68. Hutmacher DW, Sittinger M, Risbud M V. Scaffold-based tissue engineering: rationale for computer-aided design and solid free-form fabrication systems. *Trends Biotechnol.* 2004;22(7):354-62. doi:10.1016/j.tibtech.2004.05.005.

69. WOOLF AD. The Bone and Joint Decade 2000-2010. *Ann. Rheum. Dis.* 2000;59(2):81-82. doi:10.1136/ard.59.2.81.

70. Sargeant A, Goswami T. Hip implants: Paper V. Physiological effects. *Mater. Des.* 2006;27(4):287-307. doi:10.1016/j.matdes.2004.10.028.

71. Bram BM, Stiller C, Buchkremer HP, Stöver D, Baur H, Ag D. High-Porosity Titanium , Stainless Steel , and Superalloy Parts. 2000;(4):196-199.

72. Miyao R, Omori M, Watari F, et al. Fabrication of functionally graded implants by Spark Plasma Sintering and their properties. *Funtai Oyobi Fummatsu Yakin/Journal Japan Soc. Powder Powder Metall.* 2000;47(11):1239-1242. Available at: http://www.scopus.com/inward/record.url?eid=2-s2.0-0034314790&partnerID=tZOtx3y1.

73. Li JP, Li SH, de Groot K, Layrolle P. Preparation and Characterization of Porous Titanium. In: *Key Engineering Materials*.Vol 218-220.; 2001:51-54. Available at: http://www.scientific.net/KEM.218-220.51. Accessed June 29, 2014.

74. Wiria FE, Shyan JYM, Lim PN, Wen FGC, Yeo JF, Cao T. Printing of Titanium implant prototype. *Mater. Des.* 2010;31:S101-S105. doi:10.1016/j.matdes.2009.12.050.

75. Wiria FE, Chua CK, Leong KF, Quah ZY, Chandrasekaran M, Lee MW. Improved biocomposite development of poly(vinyl alcohol) and hydroxyapatite for tissue engineering scaffold fabrication using selective laser sintering. *J. Mater. Sci. Mater. Med.* 2008;19(3):989-96. doi:10.1007/s10856-007-3176-5.

76. Li X, Wang C, Zhang W, Li Y. Fabrication and characterization of porous Ti6Al4V parts for biomedical applications using electron beam melting process. *Mater. Lett.* 2009;63(3-4):403-405. doi:10.1016/j.matlet.2008.10.065.

77. Gibson LJ, Ashby MF. The Mechanics of Three-Dimensional Cellular Materials. *Proc. R. Soc. A Math. Phys. Eng. Sci.* 1982;382(1782):43-59. doi:10.1098/rspa.1982.0088.

78. Erk K a., Dunand DC, Shull KR. Titanium with controllable pore fractions by thermoreversible gelcasting of TiH2. *Acta Mater.* 2008;56(18):5147-5157. doi:10.1016/j.actamat.2008.06.035.

79. Wen CE, Yamada Y, Shimojima K, Chino Y, Asahina T, Mabuchi M. Processing and mechanical properties of autogenous titanium implant materials. *J. Mater. Sci. Mater. Med.* 2002;13(4):397-401. doi:10.1023/A:1014344819558.

80. Zou C, Zhang E, Li M, Zeng S. Preparation, microstructure and mechanical properties of porous titanium sintered by Ti fibres. *J. Mater. Sci. Mater. Med.* 2008;19(1):401-405. doi:10.1007/s10856-006-0103-0.

81. Gibson L, Ashby M. *Cellular Solids Structure and Properties*. 2nd Editio. Cambridge University Press Available at: http://www.cambridge.org/us/academic/subjects/engineering/materials-science/cellular-solids-structure-and-properties-2nd-edition. Accessed April 15, 2015.

82. DR Carter, WC Hayes. The compressive behavior of bone as a two-phase porous structure. *J. Bone Joint Surg. Am.* 1977;59(7):954-962. doi:10.1007/978-1-4471-5451-8_116.

83. Sumner DR, Turner TM, Igloria R, Urban RM, Galante JO. Functional adaptation and ingrowth of bone vary as a function of hip implant stiffness. *J. Biomech.* 1998;31(10):909-917. doi:10.1016/S0021-9290(98)00096-7.

84. Wan Z, Dorr LD, Woodsome T, Ranawat A, Song M. Effect of stem stiffness and bone stiffness on bone remodeling in cemented total hip replacement. *J. Arthroplasty* 1999;14(2):149-158. doi:10.1016/S0883-5403(99)90118-3.

85. Novitskaya E, Chen P-Y, Lee S, et al. Anisotropy in the compressive mechanical properties of bovine cortical bone and the mineral and protein constituents. *Acta Biomater.* 2011;7(8):3170-7. doi:10.1016/j.actbio.2011.04.025.

86. Pohler OE. Unalloyed titanium for implants in bone surgery. *Injury* 2000;31 Suppl 4:7-13. Available at: http://www.ncbi.nlm.nih.gov/pubmed/11270082.

87. Güden M, Celik E, Hizal A, Altindiş M, Cetiner S. Effects of compaction pressure and particle shape on the porosity and compression mechanical properties of sintered Ti6Al4V powder compacts for hard tissue implantation. *J. Biomed. Mater. Res. B. Appl. Biomater.* 2007;85(2):547-55. doi:10.1002/jbm.b.30978.

88. Farzadi A, Solati-Hashjin M, Asadi-Eydivand M, Abu Osman NA. Effect of Layer Thickness and Printing Orientation on Mechanical Properties and Dimensional Accuracy of 3D Printed Porous Samples for Bone Tissue Engineering. Claudepierre T, ed. *PLoS One* 2014;9(9):e108252. doi:10.1371/journal.pone.0108252.

89. Vaezi M, Chua CK. Effects of layer thickness and binder saturation level parameters on 3D printing process. *Int. J. Adv. Manuf. Technol.* 2010;53(1-4):275-284. doi:10.1007/s00170-010-2821-1.

90. ZOU C, LIU Y, YANG X, WANG H, WEI Z. Effect of sintering neck on compressive mechanical properties of porous titanium. *Trans. Nonferrous Met. Soc. China* 2012;22:s485-s490. doi:10.1016/S1003-6326(12)61750-6.

91. ASTM B 311-08. Standard Test Method for Density of Powder Metallurgy (PM) Materials Containing Less Than Two Percent Porosity 1. 2013:1-5. doi:10.1520/B0311-08.2.

92. Astm C373-88. Standard Test Method for Water Absorption, Bulk Density, Apparent Porosity, and Apparent Specific Gravity of Fired Whiteware Products. *Astm C373-88* 1999;88(Reapproved 2006):1-2. doi:10.1520/C0373-88R06.much.

93. ASTM Standard E9-09. Standard Test Methods of Compression Testing of Metallic Materials at Room Temperature. *Annu. B. ASTM Stand.* 2012;3.01:92-100. doi:10.1520/E0009-09.2.

94. Panigrahi BB, Godkhindi MM, Das K, Mukunda PG, Ramakrishnan P. Sintering kinetics of micrometric titanium powder. *Mater. Sci. Eng. A* 2005;396(1-2):255-262. doi:10.1016/j.msea.2005.01.016.

95. Harris JW, Stocker H. Handbook of mathematics and computational science. *Comput. Math. with Appl.* 1999;37:133. doi:10.1016/S0898-1221(99)90385-1.

96. Leng H, Dong XN, Wang X. Progressive post-yield behavior of human cortical bone in compression for middle-aged and elderly groups. *J. Biomech.* 2009;42(4):491-7. doi:10.1016/j.jbiomech.2008.11.016.

97. Reilly DT, Burstein AH. The Mechanical Properties of Cortical Bone Review Article The Mechanical Properties of Cortical Bone *. 1974;65-A(5):1001-1022.

98. Frosch K-H, Barvencik F, Viereck V, et al. Growth behavior, matrix production, and gene expression of human osteoblasts in defined cylindrical titanium channels. *J. Biomed. Mater. Res. A* 2004;68(2):325-34. doi:10.1002/jbm.a.20010.

99. Fukuda a, Takemoto M, Saito T, et al. Osteoinduction of porous Ti implants with a channel structure fabricated by selective laser melting. *Acta Biomater.* 2011;7(5):2327-36. doi:10.1016/j.actbio.2011.01.037.

100. Holm S. A Simple Sequentially Rejective Multiple Test Procedure. *Scand. J. Stat.* 1979;6(2):65-70. Available at: http://www.ime.usp.br/~abe/lista/pdf4R8xPVzCnX.pdf.

101. Öchsner A, Lamprecht K. On the uniaxial compression behavior of regular shaped cellular metals. *Mech. Res. Commun.* 2003;30(6):573-579. doi:10.1016/S0093-6413(03)00058-2.

102. Öhman C, Baleani M, Pani C, et al. Compressive behaviour of child and adult cortical bone. *Bone* 2011;49(4):769-76. doi:10.1016/j.bone.2011.06.035.

103. Gagg G, Ghassemieh E, Wiria FE. Effects of sintering temperature on morphology and mechanical characteristics of 3D printed porous titanium used as dental implant. *Mater. Sci. Eng. C. Mater. Biol. Appl.* 2013;33(7):3858-64. doi:10.1016/j.msec.2013.05.021.

104. Lakes R. Materials with structural hierarchy. *Nature* 1993;361(6412):511-515. Available at: http://dx.doi.org/10.1038/361511a0.

105. Currey JD. Bone strength: what are we trying to measure? *Calcif. Tissue Int.* 2001;68(4):205-10. doi:10.1007/s002230020040.

106. Gaston MS, Simpson a HRW. Inhibition of fracture healing. *J. Bone Joint Surg. Br.* 2007;89(12):1553-60. doi:10.1302/0301-620X.89B12.19671.

107. Claes L, Eckert-Hübner K, Augat P. The fracture gap size influences the local vascularization and tissue differentiation in callus healing. *Langenbecks. Arch. Surg.* 2003;388(5):316-22. doi:10.1007/s00423-003-0396-0.

108. Brydone a S, Meek D, Maclaine S. Bone grafting, orthopaedic biomaterials, and the clinical need for bone engineering. *Proc. Inst. Mech. Eng. Part H J. Eng. Med.* 2010;224(12):1329-1343. doi:10.1243/09544119JEIM770.

109. Qin L, Mak AT, Cheng CW, Hung LK, Chan KM. Histomorphological study on pattern of fluid movement in cortical bone in goats. *Anat. Rec.* 1999;255(4):380-7. doi:10.1002/(SICI)1097-0185(19990801)255:4<380::AID-AR3>3.0.CO;2-0.

110. Vlasea M., Basalah A., Azhari A., Kandel R. TE. Additive manufacturing for bone load bearing applications. In: Lijie Grace Zhang, John Fisher KL, ed. *3D Bioprinting and Nanotechnology in Tissue Engineering and Regenerative Medicine*. 1st Editio. Elsevier Inc.; 2015. Available at: http://store.elsevier.com/3D-Bioprinting-and-Nanotechnology-in-Tissue-Engineering-and-Regenerative-Medicine/Lijie-Grace-Zhang/isbn-9780128005477/. Accessed January 25, 2015.

111. Butscher A, Bohner M, Doebelin N, Hofmann S, Müller R. New depowdering-friendly designs for three-dimensional printing of calcium phosphate bone substitutes. *Acta Biomater.* 2013;9(11):9149-58. doi:10.1016/j.actbio.2013.07.019.

112. Vaezi M, Seitz H, Yang S. A review on 3D micro-additive manufacturing technologies. *Int. J. Adv. Manuf. Technol.* 2012;67(5-8):1721-1754. doi:10.1007/s00170-012-4605-2.

113. Bondioli IR, Bottino MA. Evaluation of shear bond strength at the interface of two porcelains and pure titanium injected into the casting mold at three different temperatures. *J. Prosthet. Dent.* 2004;91(6):541-547. doi:10.1016/j.prosdent.2004.03.033.

114. Salazar M, Pereira S. Shear bond strength between metal alloy and a ceramic system, submitted to different thermocycling immersion times. *Acta Odontol. ...* 2006;20(2):97-102. Available at: http://europepmc.org/abstract/MED/18590258. Accessed January 26, 2015.

115. Cocr BDE, Cerâmica EUMA. Evaluation of the shear bond strength of the union between two CoCr-alloys and a dental ceramic. *J. Appl. Oral Sci.* 2012;12(4):280-284.

116. Turner CH, Wang T, Burr DB. Shear Strength and Fatigue Properties of Human Cortical Bone Determined from Pure Shear Tests. *Calcif. Tissue Int.* 2001;69(6):373-378. doi:10.1007/s00223-001-1006-1.

117. German RM. *Sintering Theory and Practice*. illustrate. New York : Wiley, ©1996.; 1996. Available at: http://adsabs.harvard.edu/abs/1996stp..book.....G. Accessed January 9, 2015.

118. German R. Progress in Titanium Metal Powder Injection Molding. *Materials (Basel).* 2013;6(8):3641-3662. doi:10.3390/ma6083641.